# MECHANISTIC ANALYSIS OF THE ORGANOPHOSPHONATE-DEGRADING ENZYMES PHNY AND PHNZ

by

Jacqueline P. Séguin

A thesis submitted to the Department of Chemistry

In conformity with the requirements for

the degree of Master of Science

Queen's University

Kingston, Ontario, Canada

(August, 2015)

## Abstract

PhnY and PhnZ comprise a new microbial pathway for the degradation of the naturally occurring phosphonate 2-aminoethylphosphonic acid into glycine and inorganic phosphate. PhnY is an α-ketoglutarate / Fe(II)-dependent dioxygenase that hydroxylates the α-carbon of 2-aminoethylphosphonic acid. PhnZ is a di-iron-dependent oxygenase that cleaves the C-P bond of the PhnY product, 2-amino-1*R*-hydroxyethylphosphonic acid, using a mechanism unlike that used by other C-P bond cleaving enzymes. Kinetic parameters for PhnY were determined with 2-aminoethylphosphonic acid. A series of substrate analogues were also tested for reactivity, but PhnY was strictly specific for its native substrate. Attempts to crystallize PhnY to provide insight into its mechanism were unsuccessful in spite of the development of improved procedures to obtain concentrated samples of PhnY suitable for crystallography. PhnZ and active site variants were assayed with the native substrate 2-amino-1*R*-hydroxyethylphosphonic acid and a series of analogues. A primary deuterium kinetic isotope effect of 1.36 ± 0.06 was measured for the PhnZ reaction, indicating that cleavage of the αC-H bond of the substrate is only partly rate limiting. PhnZ was observed to convert 2*R*-amino-1*R*-hydroxypropylphosphonic acid, 3-amino-1*R*-hydroxypropylphosphonic acid, and *N*-methyl-2-amino-1-hydroxyethylphosphonic acid to inorganic phosphate. New X-ray crystal structures of PhnZ complexed with 2*R*-amino-1*R*-hydroxypropylphosphonic acid, 3-amino-1*R*-hydroxypropylphosphonic acid, and 1*R*-hydroxyethylphosphonic acid provided further insight into its substrate specificity revealing that it can accommodate some additional bulk in the active site, however the amino group and its location on the substrate are crucial for activity. The structures of PhnZ also provided new insights into the importance of the

flexible loop that closes the active site upon substrate binding, and the roles of two residues along this loop, Y24 and E27. Based on these results, a more complete mechanism for C-P bond cleavage by PhnZ is proposed.

## Co-Authorship

Work from this thesis was published in Proceedings of the National Academy of Science in 2014. (Proc. Natl. Acad. Sci. U.S.A. **2014**). This project was initiated by Fern McSorley, Laura van Staalduinen, David Zechel, and Zongchao Jia, all of whom were responsible for experimental design. Laura van Staalduinen, Fern McSorley, and Jacqueline Séguin performed research. Peter Wyatt, Katharina Schiessl, and Friedrich Hammerschmidt contributed compounds. The manuscript was prepared by Laura van Staalduinen, David Zechel, and Zongchao Jia with editorial input from all other contributing authors.

Nathalie Buttler performed the kinetic analysis of PhnY. Laura van Staalduinen assisted with crystallography of PhnY and PhnZ, X-ray data collection, and the structural determination of PhnZ crystal structures. Friedrich Hammerschmidt supplied all phosphonates unless otherwise noted with the exception of racemic 1-hydroxyethylphosphonic acid which was supplied by Peter Wyatt, and 1*R*-hydroxyethylphosphonic acid which was supplied by both groups.

## Acknowledgements

I would like to thank my supervisors David Zechel and R. Stan Brown, and my committee members Anne Petitjean and Gang Wu for their guidance and suggestions for further experiments. I would also like to thank Avena Ross for insightful discussions.

I would like to thank Fern McSorley for all of the work she did on this project before handing it off to me and for continuing to provide assistance when needed, Nathalie Butler for the work she did with PhnY, Shane Colbourne for all the assistance he provided during his summer as a lab volunteer, Yoseif Makonnen and Diane Beauchemin for ICP-MS analysis, and the labs of Friedrich Hammerschmidt and Peter Wyatt for synthesis of phosphonates. I also owe a great deal of gratitude to Zongchao Jia and Laura van Staalduinen for all of their assistance with crystallography and allowing me to be involved in the process every step of the way. I would also like to thank Natalie Roy for assistance with setting up crystal screens.

I would also like to thank Alyssa Brewer who was not only a great labmate but also a great friend. And thanks to anyone one else who has provided assistance along the way.

A special thanks goes to Paulo Cázares for encouraging me to come to Queen’s and for spending weekends and holidays showing me how to use equipment and perform the techniques I was unfamiliar with. Your support has meant everything to me.

# Statement of Originality

I hereby certify that all of the work described within this thesis is the original work of the author. Any published (or unpublished) ideas and/or techniques from the work of others are fully acknowledged in accordance with the standard referencing practices.

(Jacqueline P. Séguin)

(August, 2015)

# Table of Contents

# List of Figures

# List of Tables

# List of Abbreviations

| | |
|---|---|
| 1-HEP | 1-hydroxyethylphosphonate |
| 1-OH-2-AEP | 1-hydroxy-2-aminoethylphosphonate |
| 1-OH-2-APP | 1-hydroxy-2-aminopropylphosphonate |
| 1-OH-3-APP | 1-hydroxy-3-aminopropylphosphonate |
| 2-AEP | 2-aminoethylphosphonate |
| 2-HEP | 2-hydroxyethylphosphonate |
| α-KG | α-ketoglutarate |
| ABC | ATP-binding cassette |
| ADP | Adenosine-5’-diphosphate |
| AMPA | Aminomethylphosphonic acid |
| ATP | Adenosine-5’-triphosphate |
| C-terminal | Carboxy-terminal |
| CV | Column volume |
| C-P | Carbon-phosphorus |
| CHMP | (cyano(hydroxy)methyl)phosphonate |
| DLS | Dynamic light scattering |
| DNA | Deoxyribonucleic acid |
| *E. coli* | *Escherichia coli* |
| EDTA | Ethylenediaminetetraacetic acid |
| EPR | Electron paramagnetic resonance |
| FPLC | Fast protein liquid chromatography |

| | |
|---|---|
| FQ-EPR | Freeze quench-electron paramagnetic resonance |
| HABA | hydroxy-azophenyl-benzoic acid |
| HMP | hydroxymethylphosphonate |
| HPLC | High performance liquid chromatography |
| ICP-MS | Inductively coupled plasma-mass spectrometry |
| IPTG | Isopropyl-β-D-1-thiogalactoside |
| LB | Luria-Bertani |
| L-LDH | L-lactate dehydrogenase |
| MePn | Methylphosphonate |
| MES | 2-(*N*-morpholino)ethanesulfonic acid |
| MIOX | *Myo*-inositol oxygenase |
| MOPS | 3-(N-morpholino)propanesulfonic acid |
| $NAD^+$ | Nicotinamide adenine dinucleotide |
| N-terminal | Amino-terminal |
| NMR | Nuclear magnetic resonance spectroscopy |
| NTA | Nitrilotriacetic acid |
| $OD_{600}$ | Optical density at 600 nm |
| O-P | Oxygen-phosphorus |
| PAGE | Polyacrylamide gel electrophoresis |
| PCR | Polymerase chain reaction |
| PEP | phosphoenolpyruvate |
| $P_i$ | Inorganic phosphate |
| PITC | Phenylisothyocyanate |

| | |
|---|---|
| $PP_i$ | Pyrophosphate |
| PK | Pyruvate kinase |
| PnAA | Phosphonoacetaldehyde |
| PNP | Purine nucleoside phosphorylase |
| PnPy | Phosphonopyruvate |
| RPnTP | 5'-triphospho-α-D-ribosyl-1'-phosphonate |
| PRcP | 5-phospho-α-D-ribosyl 1,2-cyclic phosphate |
| PRPn | α-D-ribose-1-methylphosphonate-5-phosphate |
| RNA | Ribonucleic acid |
| Rpm | Rotations per minute |
| SAM | S-adenosyl methionine |
| SCS | Succinyl-CoA synthetase |
| SDS | Sodium dodecyl phosphate |
| TauD | Taurine dioxygenase |
| Tris | Tris(hydroxymethyl)aminomethane |
| WT | Wild type |

# Chapter 1

# Introduction

## 1.1 Organophosphonates as a source of metabolic phosphate

Inorganic phosphate ($P_i$) is an essential nutrient required by all forms of life. Amongst its many biochemical functions, one of the most important is the linking of nucleosides forming the phosphodiester backbones of DNA and RNA. It is also the main source of biochemical energy in the forms of adenosine triphosphate (ATP), creatine phosphate, and phosphoenolpyruvate (PEP). Furthermore, many coenzymes are phosphates, such as nicotinamide adenine dinucleotide phosphate ($NADP^+$) and pyridoxal phosphate.[1]

When $P_i$ is not immediately available in the environment, most organisms have the ability to hydrolyze phosphate esters to liberate $P_i$. Unlike higher organisms, some microorganisms also harbour metabolic pathways to enable them to obtain $P_i$ from other sources such as organophosphonates.[2] In contrast to phosphates, phosphonates have a more stable carbon-phosphorus (C-P) bond in place of one of the oxygen-phosphorus (O-P) bonds (**Figure 1-1**). The inert nature of the C-P bond imparts these compounds with greater resistance to chemical hydrolysis and thermal decomposition.[3]

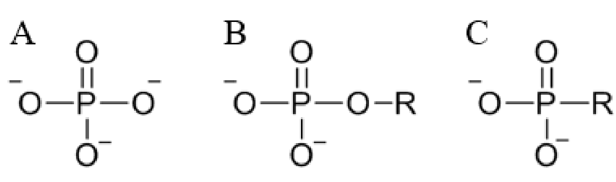


**Figure 1-1. General chemical structures of important sources of phosphate. A)** Inorganic phosphate, **B)** phosphate ester, and **C)** phosphonate.

## 1.2 Origins of organophosphonates on Earth

The origin of life-sustaining organophosphates on primitive Earth is unknown, particularly since the reducing atmosphere on primitive Earth does not favour the synthesis of these molecules. In 1969, a meteorite hit Earth in Murchison, Australia. The contents of this meteorite were studied extensively and alkylphosphonates were found to make up 29% of the soluble phosphates. It has been therefore suggested that phosphonates could have been delivered to primitive Earth by meteorites and comets.[4,5,6] It is also possible that phosphonates preceded phosphates and as Earth's atmosphere became more oxygenated, phosphates would have become the more abundant species and C-P catabolic enzymes would have evolved to either cleave O-P bonds, or would have been naturally selected against in favour of ones that do.[16] It can therefore be hypothesized that microorganisms evolved pathways and enzymes for C-P catabolism very early in the geological history of Earth.

## 1.3 Discovery and biosynthesis of naturally occurring organophosphonates

In 1959, the first naturally occurring organophosphonate was discovered in protozoa from sheep rumen.[7] Extracts from the rumen were acid hydrolyzed and the isolated compound was identified as 2-aminoethylphosphonate (2-AEP). 2-AEP has since been found in bacteria, fungi, and some higher organisms. Most commonly, 2-AEP is incorporated into the macromolecules of some of these organisms including lipids[8], polysaccharides, and proteins.[9] Other naturally occurring organophosphonates are seen in **Figure 1-2**.

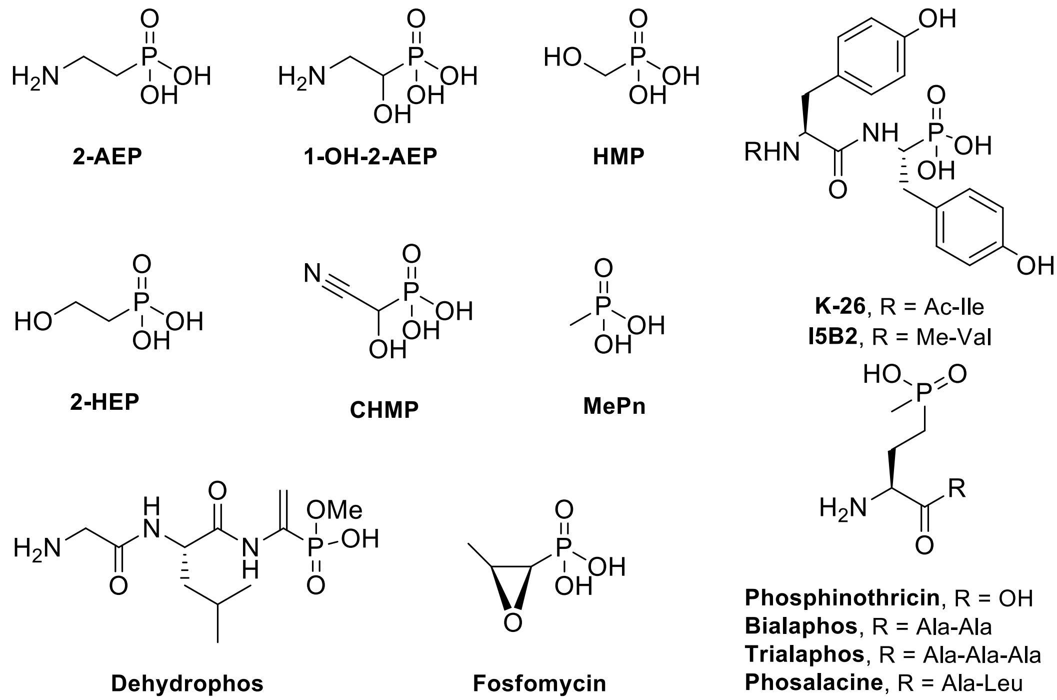


**Figure 1-2. Naturally occurring phosphonates.** 2-AEP: 2-aminoethylphosphonate, 1-OH-2-AEP: 2-amino-1-hydroxyethylphosphonate, HMP: hydroxymethylphosphonate, 2-HEP: 2-hydroxyethylphosphonate, CHMP: (cyano(hydroxy)methyl)phosphonate, MePn: methylphosphonate.

### 1.3.1 Mechanism of C-P bond formation in naturally occurring organophosphonates

The biological precursor for 2-AEP remained unknown until 1968 when *in vivo* $^{14}$C-labelling experiments in the protozoa *Tetrahymena pyriformis* revealed that the precursor was the glycolytic intermediate PEP. It was proposed that a PEP mutase may catalyze the intramolecular rearrangement of PEP to phosphonopyruvate (PnPy) (**Figure 1-3**).[10]

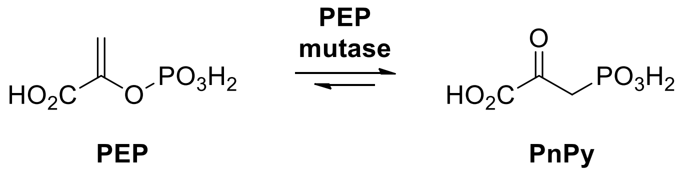

**Figure 1-3. Enzymatic synthesis of C-P bonds.** Intramolecular rearrangement of PEP to PnPy catalyzed by PEP mutase.

It was anticipated that since PEP is a high energy molecule that the equilibrium of the enzyme-catalyzed reaction would favour the conversion of PEP to PnPy, however the ratio of PEP to PnPy at equilibrium was found to be ≥500. This is likely in part due to the higher energy of the C-P bond in PnPy compared to the O-P bond in PEP.[11] Early experiments following the forward reaction of PEP to PnPy were unable to detect PEP mutase[12,13] and it was not until 1988 by monitoring the conversion of PnPy to PEP that it was isolated and characterized.[14] Initial studies showed that PEP mutase catalyzes the intramolecular rearrangement of PEP to PnPy with retention of stereochemistry at the phosphorus centre.[15] For this to occur, it was proposed that a nucleophilic enzyme residue would attack the phosphorus centre causing an inversion of stereochemistry, followed by attack of the pyruvate enolate to phosphorus causing a second inversion in stereochemistry resulting in an overall retention of stereochemistry (**Figure 1-4, A**). However, a phospho-enzyme intermediate was never isolated. X-ray crystallographic analysis of PEP mutase in complex with Mg(II) and an oxalate inhibitor revealed an active site with Mg(II) coordinated by active site residues.[16] Site-directed mutagenesis and modelling studies suggested that the reaction most likely proceeded through a double displacement mechanism, however another crystal structure in complex with a sulfopyruvate inhibitor contradicted this data and strongly supported a dissociative mechanism.[17] The crystallographic data suggested that the phosphoryl group is held in place by active site residues as metaphosphosphate is liberated and the pyruvate enolate rotates around the C1-C2 bond. C3 of the pyruvate enolate then attacks the metaphosphate on the same face from which it departed creating the phosphonyl group of PnPy with overall retention of stereochemistry (**Figure 1-4, B**).

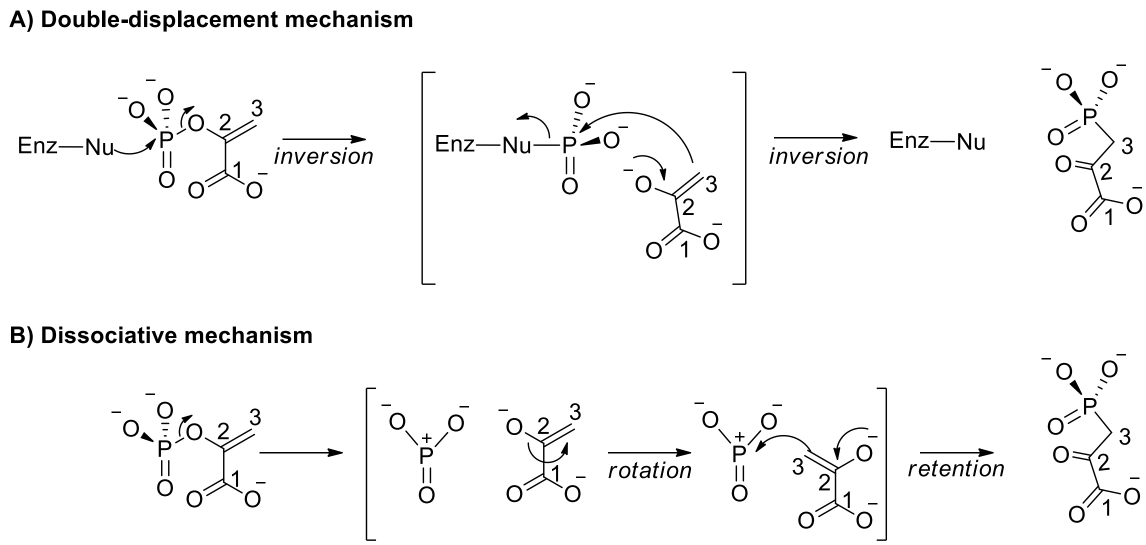


**Figure 1-4. Proposed mechanisms of C-P bond formation catalyzed by PEP mutase.** Both mechanisms result in overall retention of stereochemistry at the phosphorus centre. **A)** Early mechanism proposing double-displacement and **B)** currently accepted mechanism following a dissociative mechanism. Figure adapted from reference 17.

Currently, the biosynthesis of the C-P bond in all organophosphonates for which the gene cluster is known is well conserved and is catalyzed by PEP mutase, with the exception of C-P bond formation in the tripeptide phosphonic acids K-26 and I5B2 (**Figure 1-2**).[18] These phosphonates contain a non-proteinogenic derivative of tyrosine which is incorporated using a non-ribosomal peptide synthetase (NRPS). The mechanism of C-P bond formation is unknown, however it not believed to be catalyzed by PEP mutase, suggesting that there is another enzyme capable of forming C-P bonds in organophosphonates.[19,20,21]

In comparison to phosphonates, phosphinates contain an additional R-P bond. Natural phosphinates containing a C-P-C bond include the phosphinothricin-containing peptides (**Figure 1-2**). In their biosynthesis, the first C-P bond is formed by PEP mutase, however the second involves the transfer of a methyl group onto phosphorus by PhpK, a radical SAM and cobalamin-dependent methyltransferase. The mechanism for this reaction is still unknown, however the reaction has been reconstituted *in vitro*.[22]

### 1.3.2 Biosynthesis of 2-AEP

A consequence of the equilibrium of the intramolecular rearrangement of PEP to PnPy favouring PEP is that the biosynthesis of organophosphonates relies on a subsequent highly exergonic step to drive the reaction forward. In the case of the synthesis of 2-AEP, this step is the decarboxylation of PnPy by PnPy decarboxylase to phosphonoacetaldehyde (PnAA).[10,12,15] PnAA is subsequently converted to 2-AEP by 2-AEP-pyruvate aminotransferase (**Figure 1-5**).[9] 2-AEP can then be incorporated into other C-P macromolecules.

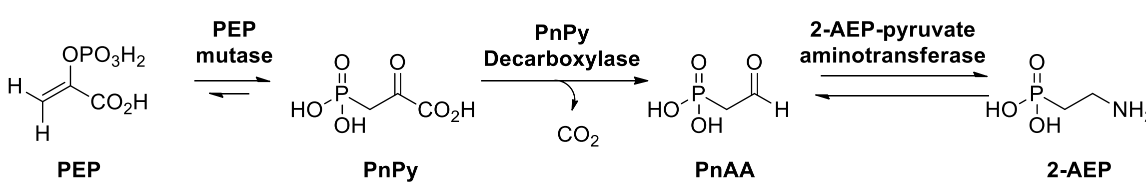


**Figure 1-5. The 2-AEP biosynthetic pathway.**

### 1.4 Commercial applications of organophosphonates

Natural and man-made organophosphonates have been exploited for a number of commercial applications. Since organophosphonates are very similar to phosphate esters, they often have high affinity for the target enzymes. For this reason, they are primarily used to inhibit enzymes for a wide variety of applications such as chemical warfare agents, antibiotics, and herbicides. One of the most successful commercially available organophosphonates is glyphosate, the active ingredient in the broad-spectrum herbicide Roundup®. It was initially believed that glyphosate would not be harmful to humans and animals because its target enzyme is part of the Shikimate pathway[23], which is used by plants and some microorganisms for the synthesis of aromatic amino acids. This hypothesis was also supported by early studies suggesting that glyphosate was rapidly degraded in the soil and was relatively non-toxic.[24-26] However, although glyphosate is metabolized by some microbes[27], recent evidence suggests that this does not occur in certain regions[28] and glyphosate as well as its immediate breakdown product, aminomethylphosphonic acid (AMPA) (**Figure 1-6**) have detrimental effects on other bacteria, fungi[29], human health, and the environment.[30-32] It is therefore of growing interest to exploit a C-P catabolic pathway for bioremediation of this growing concern.

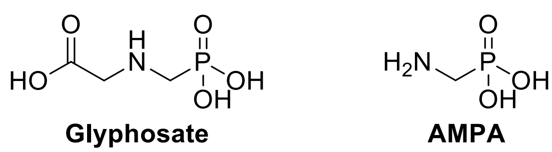


**Figure 1-6. Chemical structures of glyphosate and its immediate breakdown product AMPA.**

### 1.5 Regulation of phosphonate catabolism

Phosphate uptake in *E. coli* is under the control of the phosphate (Pho) regulon which comprises seven proteins participating in a signalling pathway.[33] These seven proteins include the integral membrane sensor histidine kinase PhoR, the transcription factor PhoB, the four-component ATP-binding cassette (ABC) transporter complex

PstSCAB, and the PhoR/PhoB inhibitory protein PhoU. Under conditions of limiting $P_i$, PstS decouples from PstCAB causing PhoR to phosphorylate PhoB, which then binds to the Pho box and activates expression of genes that allow utilization of $P_i$ and other sources of phosphorus. An example is the expression of the C-P lyase complex which allows the utilization of a variety of organophosphonates (discussed in greater detail in **section 1.6.2**). Under surplus $P_i$ conditions, PhoR dephosphorylates PhoB and represses gene expression.

Several pathways for organophosphonate metabolism that are not under regulation of the Pho operon also exist (**Figure 1-7**)[4,34-36,44] and include hydrolytic pathways (**section 1.6.1**) as well as the recently discovered oxidative pathway (**section 1.6.3**). These will be discussed in greater detail in their respective sections.

## 1.6 Mechanisms of enzymatic C-P bond cleavage

There are currently 5 known phosphonate catabolic pathways. These include the: (1) 2- phosphonoacetaldehyde hydrolase (phosphonatase) pathway, (2) phosphonopyruvate hydrolase pathway, (3) phosphonoacetate hydrolase pathway, (4) C-P lyase pathway, and (5) PhnY / PhnZ pathway (**Figure 1-7**). The enzymes that cleave the C-P bond in these pathways can be classified into one of three categories based on the mechanism by which they cleave the C-P bond: (1) Hydrolytic cleavage, (2) radical cleavage, and (3) oxidative cleavage. These mechanisms will be discussed in this section, with particular focus on the oxidative mechanism of the PhnY / PhnZ pathway, which is the pathway under investigation in this thesis.

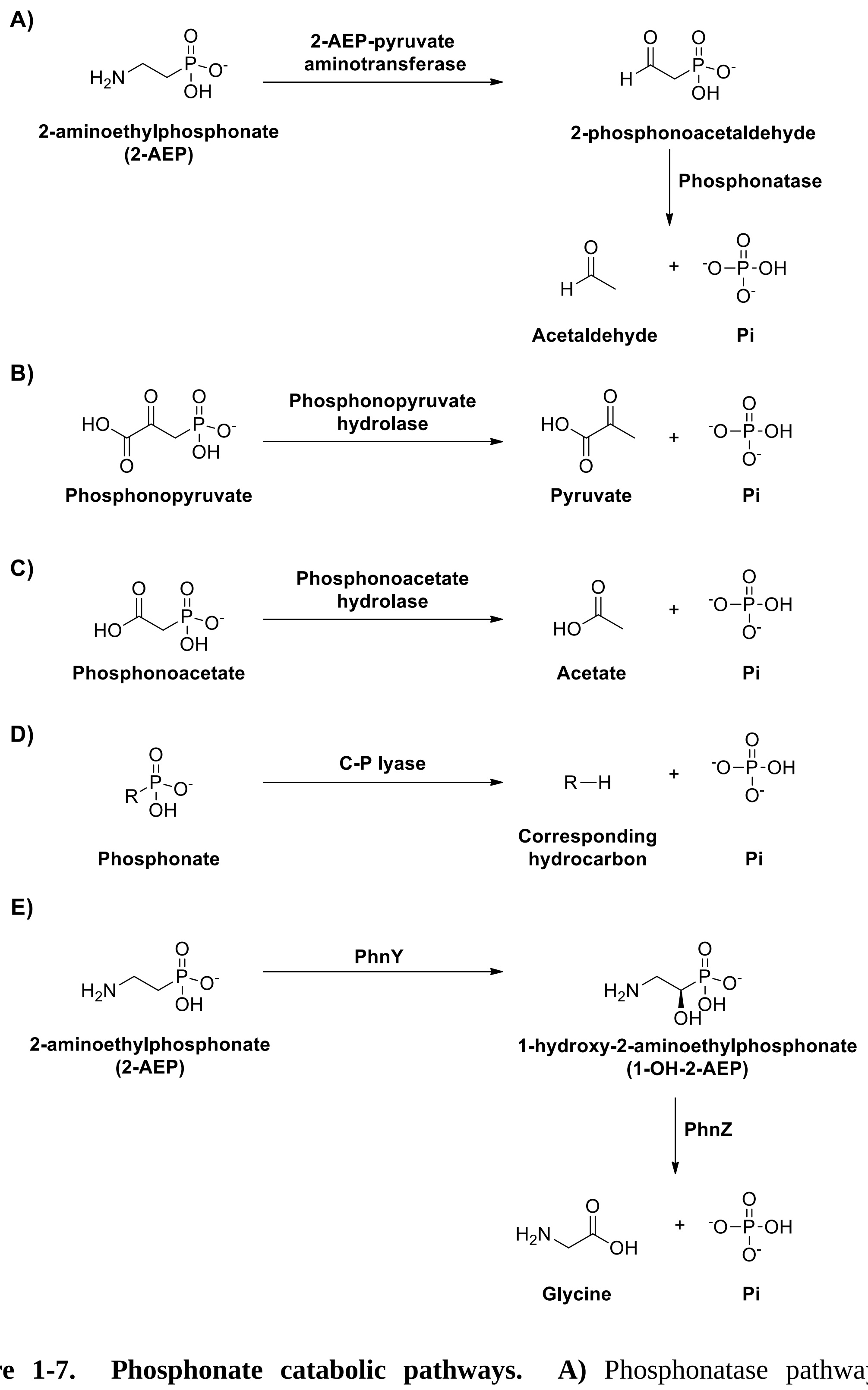


**Figure 1-7. Phosphonate catabolic pathways.** **A)** Phosphonatase pathway, **B)** phosphonopyruvate hydrolase pathway, **C)** phosphonoacetate hydrolase pathway, **D)** C-P lyase pathway, and **E)** PhnY / PhnZ pathway. Figure adapted from reference 35.

### 1.6.1 Hydrolytic C-P bond cleavage

The most common mechanism employed by C-P catabolic enzymes is the hydrolytic mechanism. The enzymes which use this mechanism are phosphonatase, phosphonopyruvate hydrolase, and phosphonoacetate hydrolase. In general, these enzymes employ a very similar mechanism in which they introduce a carbonyl group β to the phosphorus atom, following which a nucleophilic enzyme residue attacks the phosphorus centre and the β-carbonyl group acts as an electron sink during C-P bond cleavage. $P_i$ can then be liberated from the enzyme active site through hydrolysis (**Figure 1-8).** The details of the mechanisms of each of these enzymes will be discussed below.

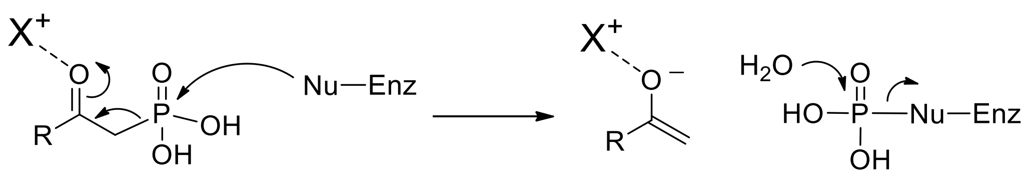


**Figure 1-8. General mechanism of hydrolytic C-P bond cleavage.** Hydrolytic C-P cleavage is employed by phosphonatase, phosphonopyruvate hydrolase, and phosphonoacetate hydrolase. Nu-Enz represents a nucleophilic enzyme residue.

#### 1.6.1.1 Phosphonoacetaldehyde hydrolase (phosphonatase)

Phosphonatase is a member of the haloacid dehalogenase superfamily, which primarily consists of phosphotransferases. It is one of the two enzymes involved in the two-step degradation of 2-AEP to acetaldehyde and $P_i$ (**Figure 1-7, a.**). The first step in 2-AEP catabolism through this pathway is the reverse of the last step in its biosynthesis which involves the transamination of 2-AEP by 2-AEP-pyruvate aminotransferase using pyruvate as the amino acceptor to form PnAA and alanine (a nitrogen source). This reaction introduces the β-carbonyl, which makes hydrolysis by phosphonatase possible.

The details of the mechanism of phosphonatase were discovered largely through X-ray crystallographic analysis.[37-40] The active site of phosphonatase is located at the interface of a core and capping domain and contains a Mg(II) ion which coordinates the substrate oxygens, some active site residues, and a water molecule. A lysine residue located at the N-terminus of an α-helix from the capping domain is rendered nucleophilic due to p$K_a$ depression. Several electrostatic effects are believed to be responsible for this p$K_a$ depression, including the electropositive field of the helix dipole where it is located at the N-terminus and its location within a hydrophobic microenvironment.

The phosphonatase mechanism proceeds through Schiff-base formation whereby the lysine residue is deprotonated and the phosphonoacetaldehyde carbonyl is protonated. Proton transfer is believed to occur through a hydrogen bond network between the lysine, a water molecule, an active site histidine, and the carbonyl of phosphonoacetaldehyde. Following formation of the Schiff-base intermediate, an active site aspartate residue attacks the phosphorus and cleaves the C-P bond, displacing lysine *N*-ethyleneamine. $P_i$ and acetaldehyde are then liberated through hydrolysis (**Figure 1-9**).

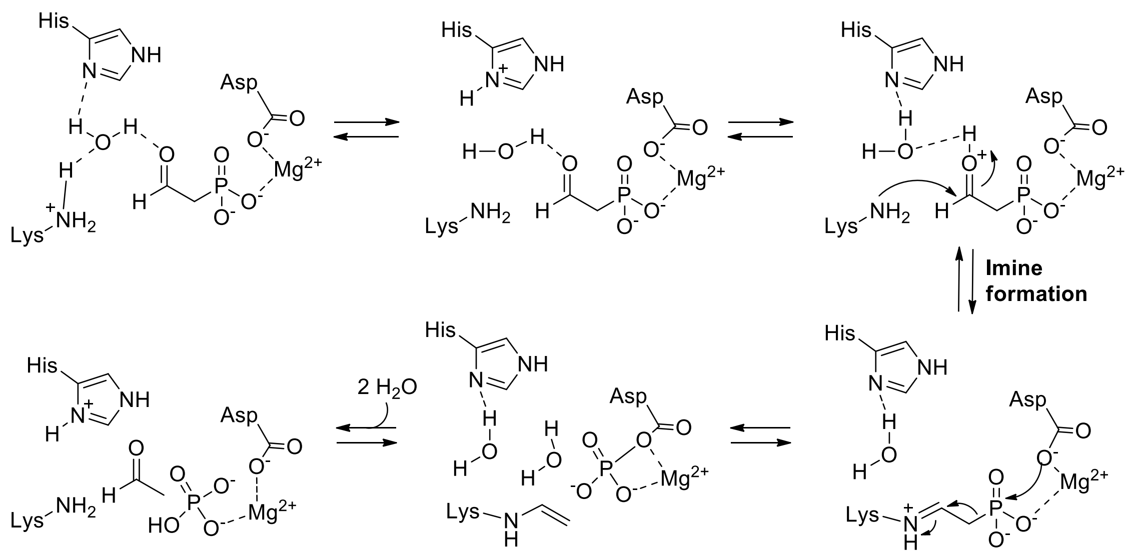


**Figure 1-9. Mechanism of C-P bond cleavage by phosphonatase.** Phosphonatase hydrolyzes phosphonoacetaldehyde yielding acetaldehyde and $P_i$. Figure adapted from reference 40.

### 1.6.1.2 Phosphonopyruvate hydrolase

Phosphonopyruvate hydrolase is the enzyme responsible for the cleavage of the C-P bond in PnPy yielding pyruvate and $P_i$ (**Figure 1-7, b.**). X-crystallography revealed the structure and key active site residues important for catalysis.[41] Within the active site of the enzyme is a Mg(II) ion that coordinates 3 aspartate residues, a glutamate residue, and the C1 and C2 oxygens of phosphonopyruvate. The mechanism is believed to proceed through a metaphosphate-pyruvate intermediate in a manner similar to that of PEP mutase. Both enzymes have conserved active site residues which appear to stabilize the metaphosphate-pyruvate enolate. However, the key difference between the two is that phosphonopyruvate hydrolase has a threonine residue in place of an asparagine. In PEP mutase, the asparagine is believed to create a barrier between the phosphoryl group and the solvent. Therefore it has been proposed that the threonine residue of phosphonopyruvate hydrolase may form a hydrogen bond with a water molecule, which in turn polarizes it and facilitates hydrolysis.

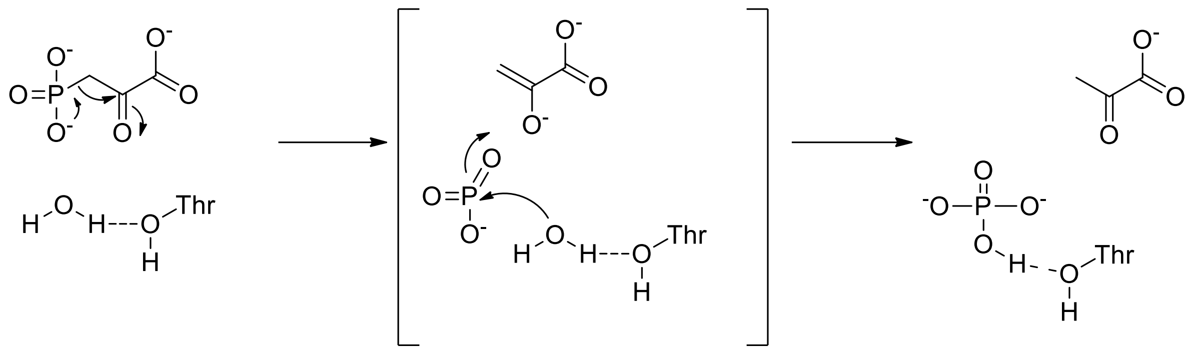

**Figure 1-10. Mechanism of C-P bond cleavage by phosphonopyruvate hydrolase.** Phosphonopyruvate hydrolase hydrolyzes phosphonoacetate yielding pyruvate and $P_i$. Figure adapted from reference 41.

### 1.6.1.3 Phosphonoacetate hydrolase

Phosphonoacetate hydrolase is a member of the alkaline phosphatase superfamily and catalyzes the cleavage of the C-P bond in phosphonoacetate producing acetate and $P_i$ (**Figure 1-7, c.**). X-ray crystallographic analysis revealed that phosphonoacetate hydrolase consists of two distinct domains: a core domain, which is highly homologous amongst members of the alkaline phosphatase superfamily, and a capping domain.[42] The active site of the enzyme, much like other members of the alkaline phosphatase superfamily, contains two metal ions, both of which are zinc ions. The first ion is believed to activate a water molecule for nucleophilic displacement at phosphorus during hydrolysis of the phosphorylated enzyme intermediate. The second ion is believed to activate the catalytic threonine residue for nucleophilic attack at phosphorus. The zinc ions also contribute to electrostatic stabilization of oxyanions during P-O bond cleavage. In other members of the alkaline phosphatase family, a third metal ion is present, however in phosphonoacetate hydrolase, this ion appears to be replaced by active site cysteine, aspartate, asparagine, tyrosine and threonine residues which form a hydrogen bonding network. It is currently not well understood how this may affect the mechanism of the reaction in comparison to other enzymes of the alkaline phosphatase superfamily.

Much like the other phosphonohydrolases, phosphonoacetate hydrolase employs charge delocalization onto a β-carbonyl, which in this case is the carboxylate of phosphonoacetate. An active site threonine residue is activated by a Zn(II) ion allowing it to act as a nucleophile and attack at phosphorus cleaving the C-P bond. This releases acetate as an aci-carboxylate with the charges being stabilized by coordination to a second Zn(II) ion and a water molecule. The phosphoryl group can then be released from the enzyme active site as $P_i$ by another water molecule that is coordinated through the first Zn(II) ion, thus polarizing it and rendering it capable of hydrolyzing the P-O bond between phosphorus and the oxygen of the threonine side chain (**Figure 1-11**).

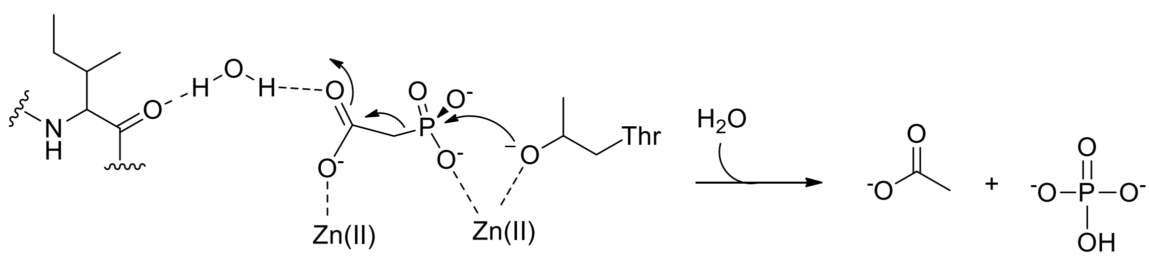


**Figure 1-11. Mechanism of C-P bond cleavage by phosphonoacetate hydrolase.** Phosphonoacetate hydrolase hydrolyzes phosphonoacetate yielding acetate and $P_i$. Figure adapted from reference 42.

### 1.6.2 Radical C-P bond cleavage by CP-lyase

The C-P lyase pathway is the most widespread pathway for phosphonate degradation and it is able to convert the largest variety of substrates.[43] This pathway is believed to have evolved early and to have undergone numerous horizontal gene transfers suggesting that there is strong selective pressure for maintenance and acquisition of the pathway.[44] It is used by a number of different bacteria for the degradation of organophosphonates such as alkylphosphonates, 2-AEP, phenylphosphonate, phosphonomethylglycine, and methylphosphonate to the corresponding hydrocarbons and $P_i$ (**Figure 1-7, d.**).[45]

The C-P lyase pathway has primarily been investigated in *Escherichia coli* where it is under control of Pho regulon which is induced under limiting $P_i$ conditions. The multi-enzyme complex is encoded by the 14 genes of the *phn*CDEFGHIJKLMNOP operon. It is currently proposed that PhnC, PhnD, and PhnE form a phosphonic acid transporter[46], PhnF is a *phn* operon repressor[47], PhnG-PhnM form the minimal region for catalysis of C-P bond cleavage, PhnN[48,50,49] is a bisphosphokinase, PhnO is an *N*-acetyltransferase involved in the detoxification of 1-aminoalkylphosphonic acids[50], and PhnP is a phosphodiesterase.[51]

### 1.6.2.1 Proposed mechanism of C-P bond cleavage by the C-P lyase

The mechanism of C-P bond cleavage by the C-P lyase was first proposed in 1987 to use a radical mechanism yielding the corresponding hydrocarbon and $P_i$.[52] The first step in the proposed mechanism involved oxidation or reduction of an alkylphosphonate to form an alkylphosphonyl or an alkylphosphoryl radical. The radical intermediate was then proposed to undergo cleavage of the C-P bond releasing an alkyl radical, and either meta-phosphoric acid or phosphite. The radical species would then abstract a hydrogen from an unknown donor forming an alkane (**Figure 1-12**).

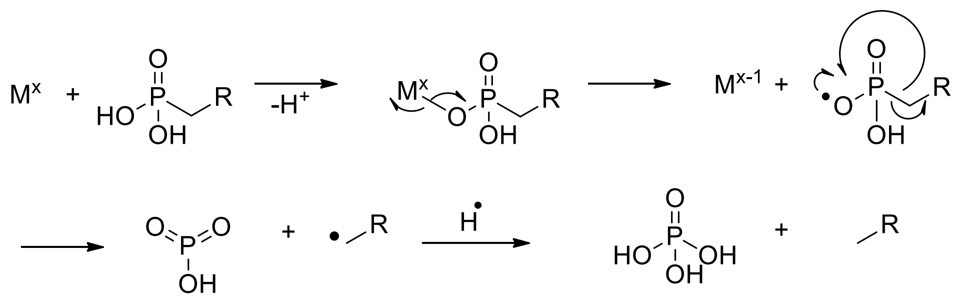

**Figure 1-12. First proposed mechanism of radical C-P bond cleavage by C-P lyase.** Figure adapted from reference 52.

A major hurdle in elucidating the mechanism of C-P bond cleavage by C-P lyase was the inability to observe the reaction *in vitro*. The first *in vitro* reconstitution of the C-P lyase reaction was in 2011 and a new mechanism for the reaction was proposed.[48] Briefly, it was found that PhnI is responsible for the first step in the reaction which involves the displacement of adenine in ATP by the phosphonate (in this case, methyl phosphonate was used as the substrate) forming a phosphate ester with inverted configuration at the anomeric carbon, 5'-triphospho-α-D-ribosyl-1'-phosphonate (RPnTP). PhnG, PhnH and PhnL were all required in order to carry out this transformation. It had been suggested by previous studies that the next step in the pathway is hydrolysis of the β- and γ- phosphoryl groups. PhnM is a member of the amidohydrolase superfamily, which consists of enzymes capable of carrying out hydrolysis at carbon and phosphorus centres. This made PhnM the prime candidate for catalyzing the hydrolysis of RPnTP generating α-D-ribose-1-methylphosphonate-5-phosphate (PRPn) and pyrophosphate ($PP_i$). Accumulation of this intermediate in growth media when *phnJ* is deleted suggested that this was the substrate that ultimately undergoes C-P bond cleavage.[51] The sequence of PhnJ contains four conserved cysteine residues which may form a portion of an Fe-S cluster, suggesting that it may belong to the radical SAM superfamily which contain conserved cysteine residues for the assembly of a [4Fe-4S] cluster.[53] Therefore, based on the previously proposed radical mechanism, PhnJ was the most likely candidate for C-P bond cleavage. PhnJ was incubated with each of RPnTP and PRPn, and a $[4Fe\text{-}4S]^{2+}$ cluster and SAM. Incubation with RPnTP yielded no reaction products, however incubation with PRPn produced 5-phospho-α-D-ribosyl 1,2-cyclic phosphate (PRcP) (a previously discovered intermediate in the pathway[51]) and methane (**Figure 1-13**).

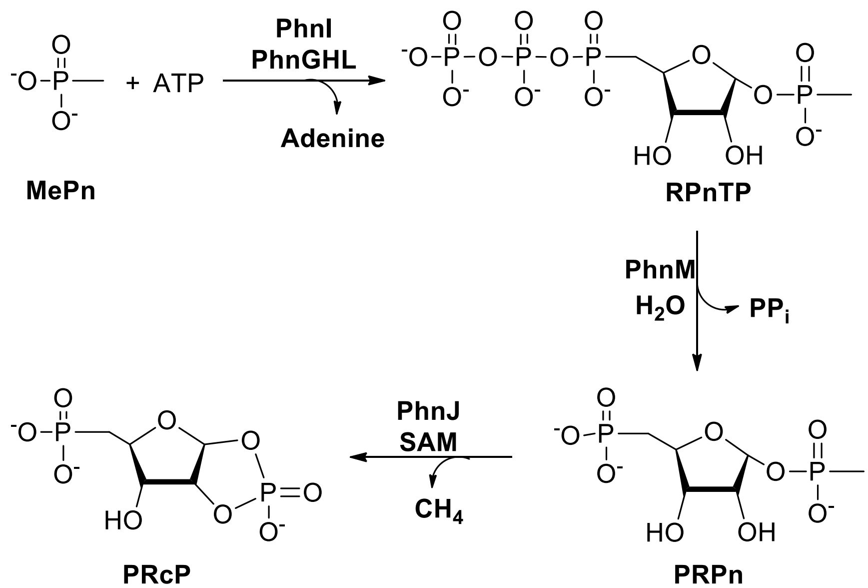


**Figure 1-13. Proposed intermediates of phosphonate degradation by the C-P lyase pathway.** Figure adapted from reference 48.

The mechanism of methylphosphonate degradation by PhnJ was reported in 2013.[54] The mechanism by which PhnJ cleaves the C-P bond is proposed to be initiated by transfer of an electron from the Fe-S cluster to SAM, cleaving SAM to produce L-Met and the 5'-deoxyadenosyl radical.[48] This radical abstracts a hydrogen from G32 in PhnJ, which subsequently abstracts a hydrogen from the C262 side chain, producing a thyil radical, which in turn attacks the phosphonate at phosphorus cleaving the C-P bond and displacing a methyl radical that then abstracts a hydrogen from G32 producing methane and regenerating the glycyl radical. Intramolecular attack at phosphorus by the ribose 2-hydroxyl then displaces the substrate from the enzyme forming the cyclic phosphate structure (**Figure 1-14)**.

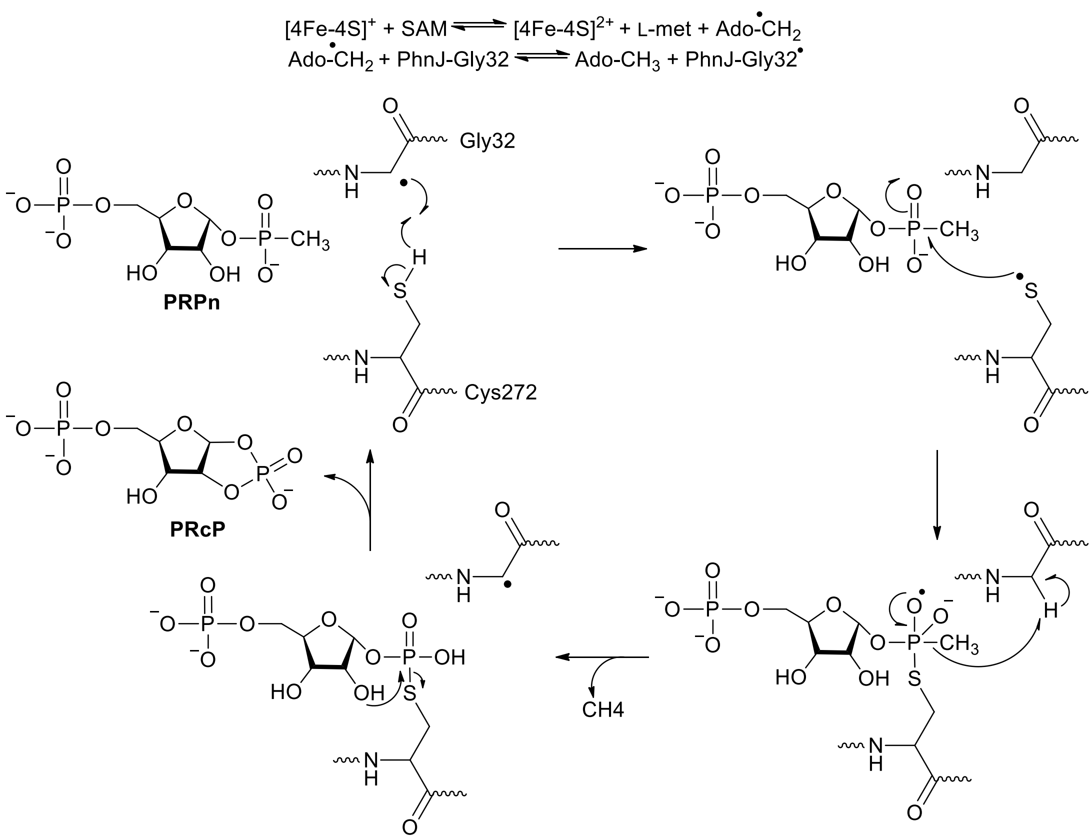


**Figure 1-14. Proposed mechanism of C-P bond cleavage by PhnJ.** Figure adapted from references 48 and 54.

### 1.6.2.2 Structure of the C-P lyase core complex

In addition to the mechanism, researchers have long sought to solve the structure of the C-P lyase. In 2011 the labs of Zechel, Hove-Jensen, and Jochimsen isolated a stable and soluble complex of five of the gene products from the *phn* operon, *phnGHIJK*, which make up the C-P lyase core complex.[55] More recently, the PhnGHIJ core complex was isolated and the crystal structure solved.[56] Up until that point PhnH was the only protein of this complex that had been structurally characterized, revealing that this protein formed a symmetrical dimer in solution and in crystal form.[57] The C-P lyase core complex crystallizes as the two-fold symmetric hetero-octamer $(PhnGHIJ)_2$. The overall architecture reveals remarkable symmetries contributing to its assembly. At the core of the structure is a PhnI homodimer upon which the rest of the complex is assembled. PhnJ binds PhnI through extensive interactions and also, surprisingly, forms a heterodimer with PhnH, with which it shares remarkable homology of core folds despite having dissimilar sequences. The PhnHJ heterodimer also bears remarkable similarity to the structure of the PhnH homodimer. The second instance of symmetry is the PhnG and PhnI heterodimer, with PhnG attaching to PhnI through insertion of a beta-hairpin into a groove in PhnI.

The $(PhnGHIJ)_2$ crystal structure also reveals the binding sites for the iron cluster and SAM in PhnJ. Although C272 is located within proximity to the cluster, G32 is more than 30 Å away and would not be able to carry out its role in the current proposed mechanism. But this does not discount the possibility that there may be a structural rearrangement that places G32 within proximity. There also appears to be a second potential active site at the interface between PhnI and PhnJ, where histidine residues coordinate a zinc ion. The role of this second active site is currently unknown.

### 1.6.3 Oxidative C-P bond cleavage by PhnZ

The most recently discovered mechanism of C-P bond cleavage is that of the di-iron oxygenase PhnZ. This enzyme catalyzes the second step in the two-step degradation of 2-AEP to glycine and $P_i$ by the enzymes PhnY and PhnZ (**Figure 1-7, e.**). The mechanisms of these enzymes are the subject of investigation for this thesis.

#### 1.6.3.1 The discovery of the PhnY / PhnZ pathway

A screen of metagenomic DNA recovered from seawater off the coast of Hawaii by the DeLong research group sought to discover new pathways for phosphonate utilization.[58] They hypothesized that since phosphonates are a major source of dissolved organic phosphorus in the ocean that they could be a source of phosphorus for marine microorganisms in $P_i$-limiting regions. The metagenomic library was screened for genes that allowed *E. coli* lacking a functional C-P lyase system to grow on minimal media containing 2-AEP as the sole source of phosphate. This study led to the discovery of two novel genes involved in 2-AEP degradation: *phnY* and *phnZ.*

The nature of 2-AEP catabolism by PhnY and PhnZ was discovered through *in vitro* re-constitution of the pathway.[59] Sequence homology suggested that PhnY belonged to the non-heme Fe(II)/α-ketoglutarate-dependent dioxygenase family, whereas PhnZ was a member of a phosphohydrolase superfamily that is characterized by a His-Asp (HD) active site motif. The reaction of PhnY using 2-AEP as the substrate in the absence of co-factors was first analyzed using $^{31}$P-NMR spectroscopy and resulted in a signal at $\delta$ 17.3 ppm (relative to $H_3PO_4$, $\delta = 0$ ppm). When Fe(II), α-ketoglutarate, ascorbate, 2-AEP, and PhnY are combined a new signal appears at $\delta$ 14.3 ppm. It was hypothesized that analogous to TauD[65] and DhpA[60] of the non-heme Fe(II)/α-ketoglutarate-dependent dioxygenase family, PhnY would catalyze the α-hydroxylation of 2-AEP. The product of this reaction would be the known organophosphonate 1-OH-2-AEP. When a reaction mixture of Fe(II), α-ketoglutarate, ascorbate, and PhnY is spiked with a racemic synthetic standard of the expected product, an increase is the signal at $\delta$ 14.3 ppm is observed and confirms the identity of the PhnY product.

The addition of PhnZ to a PhnY reaction resulted in complete conversion to $P_i$, which has a characteristic signal of approximately δ 3 ppm in $^{31}$P-NMR. However, a PhnZ reaction with (±)-1-OH-2-AEP resulted in only 50% conversion to $P_i$ suggesting that PhnZ is specific for one enantiomer of its substrate. Investigation into the metal ion dependence of PhnZ suggested that only Fe(II) can afford full activity to PhnZ, permitting full conversion to $P_i$. This dependence suggested that PhnZ may in fact be an oxygenase and the most likely products of its reaction would therefore be glycine and $P_i$. The production of glycine by PhnZ was demonstrated by using HPLC to analyze reaction products derivatized with phenylisothyocyanate (PITC), and confirming the production of glycine by co-injecting with a PITC-derivitized glycine standard. The production of glycine has also been confirmed by a study by Wörsdörfer and coworkers[61] who used mass spectrometry to detect glycine. This study also confirmed the product of the PhnY reaction.

### 1.6.3.2 Stereospecificty of PhnY and PhnZ

PhnY hydroxylates 2-AEP at the carbon α to phosphorus generating a new stereocentre. The configuration of this stereocentre was determined by examining the PhnZ reaction. When PhnZ is directly added to a PhnY reaction mixture, it can fully convert the PhnY product to $P_i$, however it can only convert 50% of a synthetic racemic mixture of this product. A reaction of PhnZ with a synthetic (*S*)-enantiomer of its substrate does not result in the conversion to $P_i$, however a reaction of PhnZ with the (*R*)-enantiomer results in full conversion to $P_i$. This confirms that PhnY produces (*R*)-1-OH-2-AEP and that this is the only enantiomer that PhnZ accepts. This observation was also confirmed by Wörsdörfer and coworkers who used polarimetry to determine the configuration of the product of the PhnY reaction.[61]

### 1.6.3.3 Metal ion dependence of PhnZ

It was known that PhnZ required a metal ion cofactor for activity through the observation that all activity was lost with the addition of EDTA. When PhnZ is stripped of metal ions and replaced with a variety of other metal ions only Fe(II) affords full activity. In fact, ICP-MS analysis corroborates this observation since PhnZ purified from *E.coli* co-purifies with approximately 1.25 ± 0.14 mol $^{54}$Fe and 1.18 ± 0.12 mol $^{57}$Fe per mol of PhnZ. Furthermore, activity assays conducted in the presence of Fe(II) or Fe(III) suggest that the required oxidation state to afford activity is Fe(II). Wörsdörfer and coworkers confirmed the Fe(II) dependence of PhnZ using Mössbauer and electron paramagnetic (EPR) spectroscopies.[61]

The top structural homologue of PhnZ is *myo*-inositol oxygenase (MIOX). This enzyme catalyzes the oxidative cleavage of a carbon-carbon bond in *myo*-inositol using a pair of Fe metal ions that exist in a mixed oxidation, or valence, state corresponding to Fe(II)/Fe(III).[62,63] Recent work by Wörsdörfer and coworkers has confirmed that much like MIOX, PhnZ also uses a mixed-valence active site for oxidative cleavage of the C-P bond in (*R*)-1-OH-2-AEP.[61] To specifically reconstruct the Fe(II)/Fe(III) oxidation state, they treated aerobically isolated PhnZ with ascorbate to reduce the diiron cluster to approximately ~40% Fe(II)/Fe(III) which was confirmed using EPR spectroscopy. Within 30 minutes, complete conversion of the substrate (*R*)-1-OH-2-AEP to $P_i$ was observed by $^{31}$P-NMR spectroscopy. To test if the Fe(III)/Fe(III) diiron cluster of PhnZ would be catalytically active, they oxidized the remaining Fe(II) iron with ferricyanide. The mixed Fe(II)/Fe(III) state of PhnZ was virtually undetectable by EPR after oxidation, and virtually no conversion of the substrate was observed with this form of the enzyme. To demonstrate that the inactive Fe(III)/Fe(III) state can be converted to the active Fe(II)/Fe(III) state, the protein sample was treated with 5 equivalents of ascorbate to reduce Fe(III)/Fe(III) to Fe(II)/Fe(III). By EPR, 40% Fe(II)/Fe(III) was observed and within 30 minutes, complete conversion of substrate to $P_i$ was observed. Freeze quench (FQ)-EPR studies also suggests a rapid cyclization of the decay and reformation of the PhnZ-Fe(II)/Fe(III) - (R)-1-OH-2-AEP complex, similar to what has been observed with MIOX.[63]

**1.6.3.4 The structure of PhnZ**

To date, four crystal structures of PhnZ have been solved. Two structures were solved by the Zechel and Jia labs that correspond to PhnZ bound to the buffer additive L-tartrate and (*R)*-1-OH-2-AEP at resolutions of 1.70 Å (PDB ID: 4MLM) and 1.85 Å (PDB ID: 4N6W), respectively.[62,64] In parallel, two structures of lower resolution were solved by Wörsdörfer corresponding to PhnZ bound to its substrate (*R)*-1-OH-2-AEP and citrate at resolutions of 2.10 Å (PDB ID: 4MLN) and 2.98 Å (PDB ID: 4N71), respectively.[61]

Two virtually identical molecules of the L-tartrate / PhnZ complex were observed in the asymmetric unit of the crystal (**Figure 1-15, a**). The two Fe ions, Fe1 and Fe2, are found bridged by one half of the HD motif, D59, and a water molecule. Fe1 is coordinated in a distorted octahedral geometry by the other half of the HD motif, H58, as well as Y24, H34, D59, D161, and the bridging water molecule. Fe2 is also coordinated in an octahedral geometry by D59, H80, H104, the bridging water molecule, and the α-hydroxyl oxygens of L-tartrate that bind to Fe2 in a bidentate mode (**Figure 1-15, a; Figure 1-16**).

Two molecules, A and B, of the (*R)*-1-OH-2-AEP / PhnZ complex were found in the asymmetric unit. Much like the L-tartrate complex, (*R)*-1-OH-2-AEP binds to Fe2 in a bidentate mode through the C1 hydroxyl and a phosphonyl oxygen (**Figure 1-16, b**). In this orientation, the C1 hydrogen projects toward Fe1 where $O_2$ is proposed to bind. Two radically different conformations were observed in molecules A and B that displayed large movements of two loops around the active site. The active site of molecule A from the substrate complex is nearly closed to solvent and the 2-amino group of substrate, which is likely protonated, forms an electrostatic interaction with E27. The phenolic oxygen of Y24 that is coordinated to Fe1 in the L-tartrate complex is replaced by a water molecule in molecule A of the substrate complex. However, molecule B resembles more closely the structure of the L-tartrate complex and lacks the key interaction seen between the 2-amino group of the substrate and E27. The Y24 residue in molecule B still occupies the $O_2$ binding at the apical position of Fe1. This suggest that molecule A of the substrate complex represents the active Michaelis complex following recognition of the substrate by E27 and triggering expulsion of Y24 from the active site making space for $O_2$ to bind at Fe1. This action causes the loop comprised of D21-N30 to cover the active site creating the closed conformation. This change is accompanied by movement of another loop comprised of H62-H80. Molecule B therefore represents an inactive complex before substrate recognition, likely the result of Fe1 being oxidized to the ferric state during the aerobic crystallization conditions. Both PhnZ structures (citrate complex and substrate complex) solved by Wörsdörfer and coworkers displayed the open conformations and they did not observe the closed conformation as seen by Zechel and coworkers.

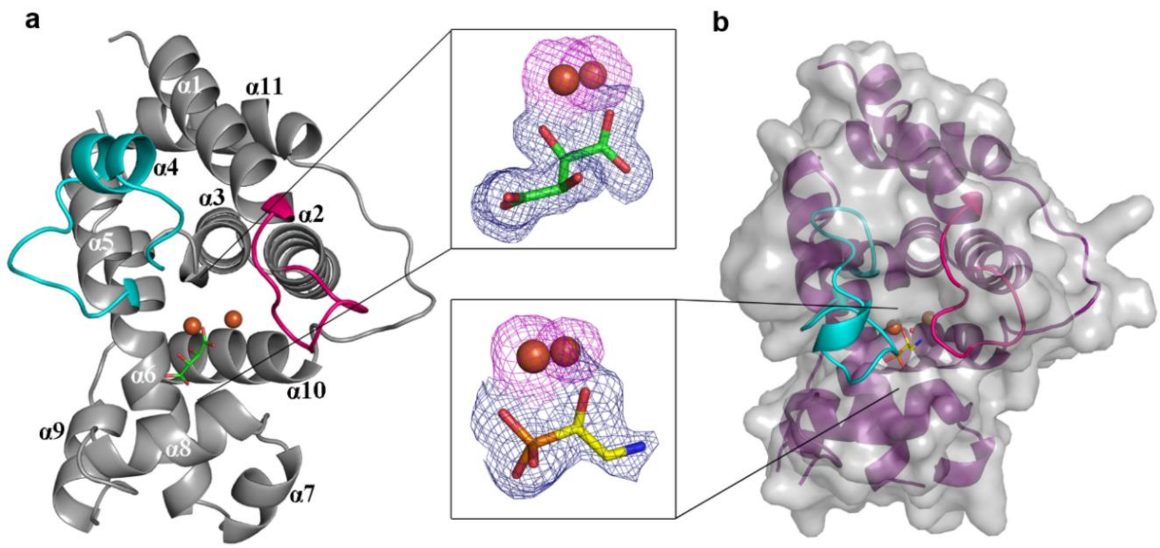


**Figure 1-15. Crystal structures of PhnZ. A)** Structure of PhnZ molecule A bound to L-tartrate, **B)** structure of PhnZ molecule A bound to (*R*)-1-OH-2-AEP overlaid with the surface representation of the L-tartrate complex. Large movements of two loops (teal and magenta) can be observed. Fe ions are modeled as orange spheres, L-tartrate is modeled as greens sticks, and (*R*)-1-OH-2-AEP is modeled as yellow and orange sticks. Figure adapted from reference 64.

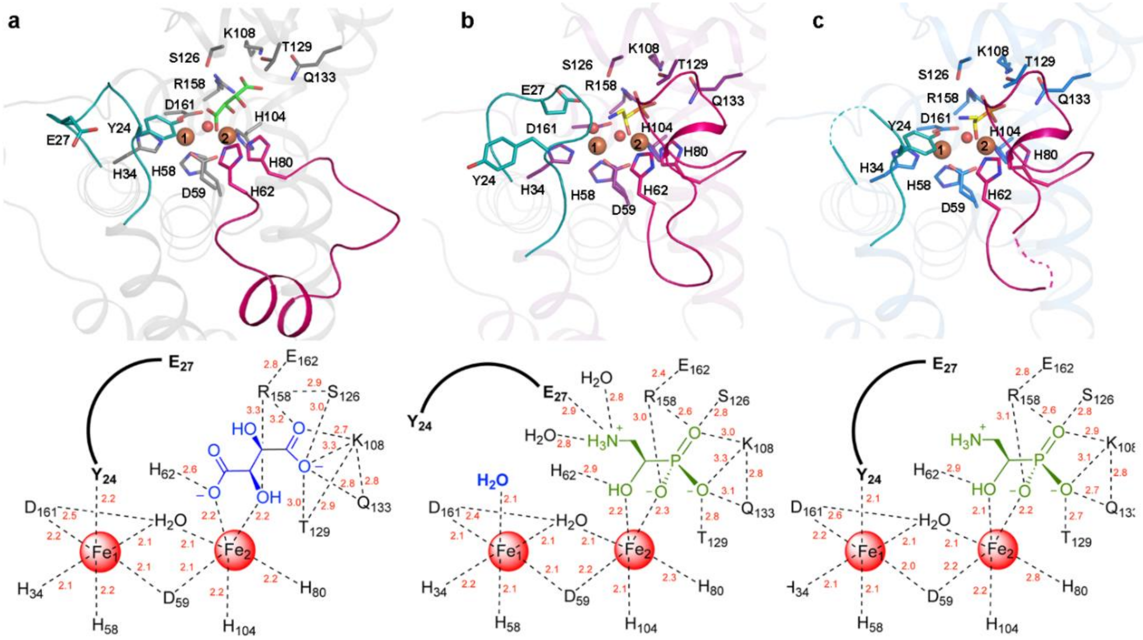

**Figure 1-16. Structures PhnZ active sites. A)** PhnZ-L-tartrate complex, molecule A, **B)** PhnZ-substrate complex, molecule A, and **C)** PhnZ-substrate complex, molecule B. Lower: Active site schemes corresponding to the structure in the upper panel. Figure adapted from reference 64.

### 1.6.3.5 Proposed mechanism of α-hydroxylation by PhnY

A mechanism for hydroxylation by PhnY can be proposed based on the known mechanism of the enzyme taurine dioxygenase (TauD), also a member of the non-heme Fe(II)/α-ketoglutarate-dependent dioxygenase family, that carries out the hydroxylation of the carbon α to sulfur in taurine (**Figure 1-17**).[65]

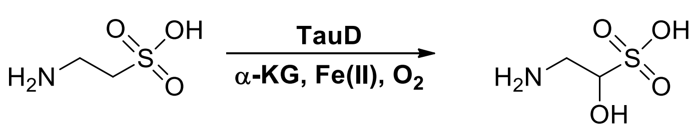

**Figure 1-17. Reaction catalyzed by TauD.** TauD catalyzes the α-hydroxylation of taurine.

The mechanism begins with the generation of a powerful ferryl oxygen species (Fe(IV)=O) that is capable of hydrogen abstraction. This species is generated through the oxidation of α-ketoglutarate, which enters the active site followed by $O_2$, and undergoes decarboxylation releasing succinate. The Fe(IV)=O species that is generated can subsequently abstract a hydrogen from the carbon α to phosphorus to produce a carbon-centered radical and an Fe(III)-OH intermediate. Rebound of the hydroxyl back to the substrate produces (*R*)-1-OH-2-AEP and regenerates Fe(II) for another catalytic cycle (**Figure 1-18**).[66] There is currently no crystal structure of PhnY to identify the active site environment that would catalyze this process.

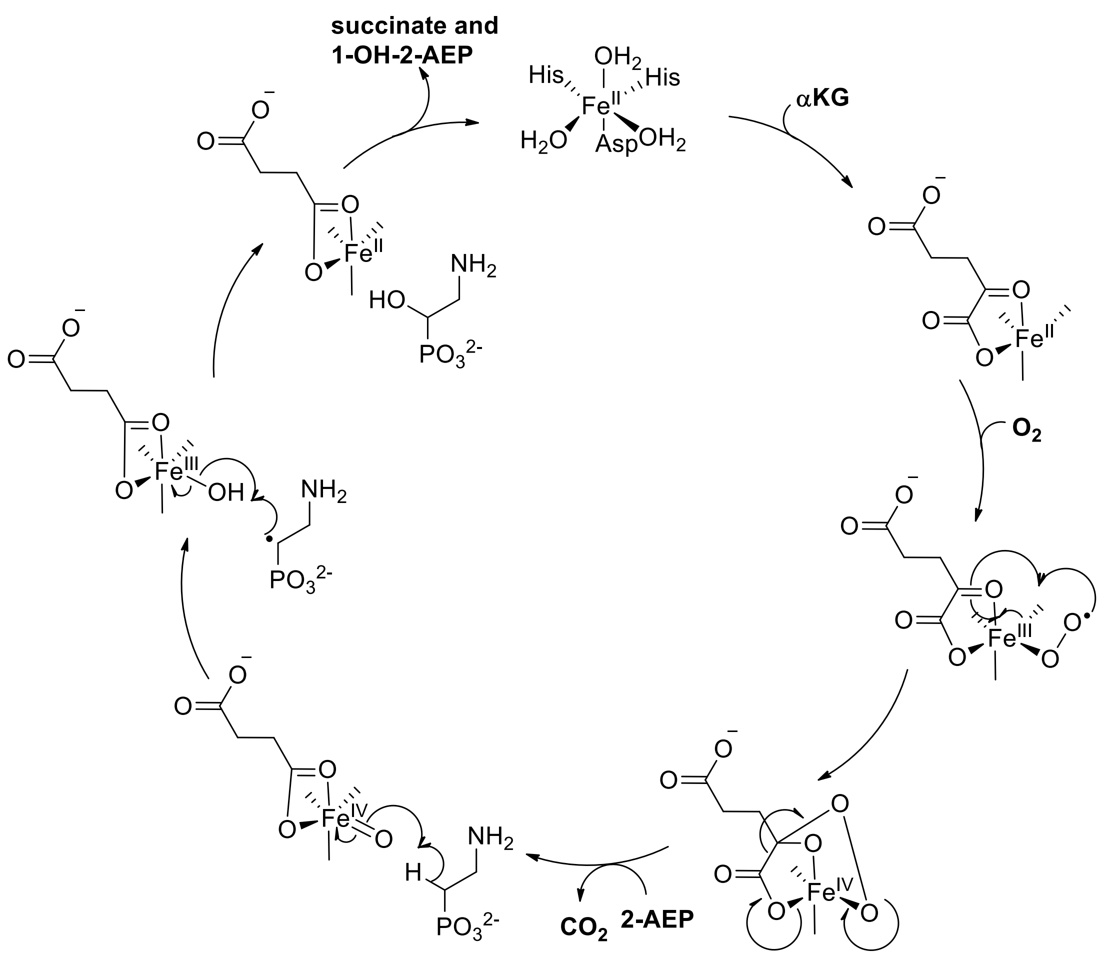


**Figure 1-18. Proposed mechanism of α-hydroxylation by PhnY.** Figure adapted from reference 66.

### 1.6.3.6 Proposed mechanism of C-P bond cleavage by PhnZ

The mechanism of PhnZ has been proposed based on computational modelling of the mechanism of MIOX.[59,67] MIOX is also a member of the HD superfamily and catalyzes the cleavage of a carbon-carbon (C-C) bond in *myo*-inositol (**Figure 1-19**).

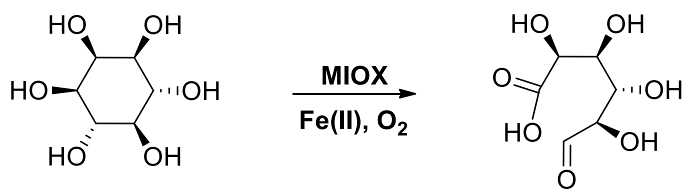


**Figure 1-19. Reaction catalyzed by MIOX.** MIOX catalyzes the C-C bond cleavage of *myo*-inositol.

PhnZ likely uses Fe1 in the ferrous state to reduce molecular oxygen to form superoxo-Fe(III) species and Fe2 would likely be in the ferric Fe(III) state to bind the substrate in a bidentate mode. The superoxo-Fe(III) species at Fe1 would abstract the α-hydrogen of the substrate to form an acylphosphonate intermediate and concomitant reduction of Fe2 to the ferrous state. The metal ion bridging hydroxide is then believed to act as a base to facilitate nucleophilic attack of the Fe(III)-hydroperoxide on the alpha carbonyl of the acylphosphonate intermediate. Calculations for MIOX favour homolytic cleavage of the bridged peroxide leading to the formation of the Fe(IV)=O species and the *gem*-diolate phosphonate intermediate. C-P bond cleavage would be initiated by abstraction of the hydroxyl hydrogen by the Fe(IV)=O oxygen leading to glycine and metaphosphate. Metaphosphate may be attacked by water to form $P_i$ directly, or alternatively be captured by the glycine alpha carboxylate to form glycyl phosphate. The glycyl phosphate would then be hydrolysed to glycine and $P_i$ (**Figure 1-20**).

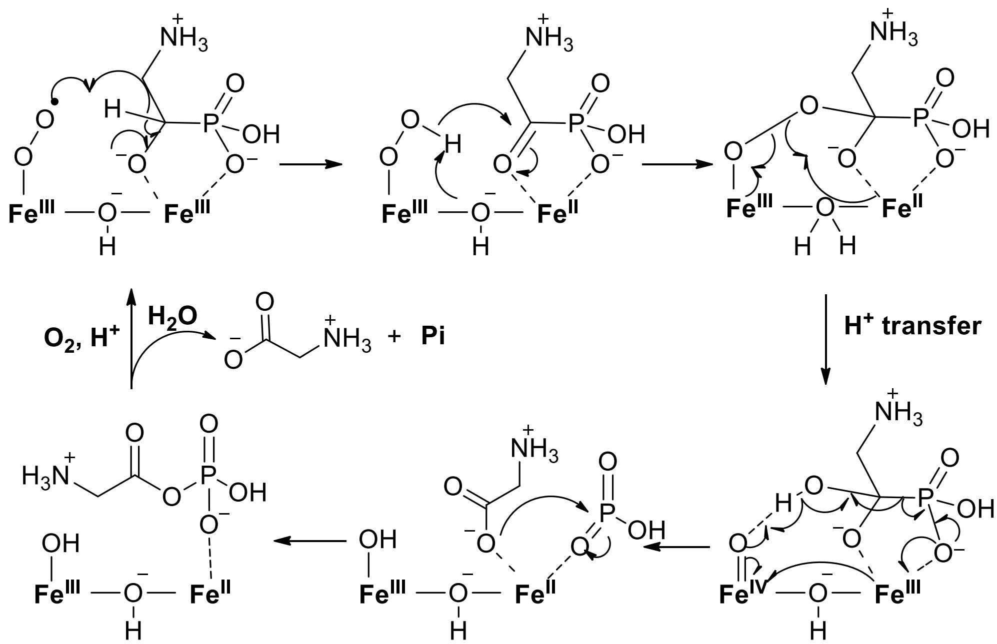


**Figure 1-20. Proposed mechanism of C-P bond cleavage by PhnZ.** Figure reproduced from reference 59.

### 1.6.4 Unknown phosphonate catabolic pathways

Other uncharacterized pathways for C-P catabolism are also believed to exist. For instance, the pathogenic bacteria *Campylobacter jejuni*[68] and *Helicobacter pylori*[69] are capable of degrading numerous phosphonates with a substrate scope similar to that of the C-P lyase. However, investigations of their genomes suggest that they do not contain any of the homologous genes that are conserved within bacteria that harbor the C-P lyase pathway, suggesting that they utilize novel organophosphonate degradation pathways.

## 1.7 Thesis objectives

The ultimate objectives of this thesis are to further the understanding of the mechanisms of PhnY and PhnZ and to establish a basis for the rational engineering of their substrate specificities. With regards to PhnY, the objectives are (1) to obtain a crystal structure to determine active site residues important for catalysis and substrate specificity,

(2) test substrate analogues with PhnY to explore its substrate specificity, and (3) conduct kinetic analysis to determine kinetic parameters. With regards to PhnZ, the objectives are (1) to explore its substrate specificity using substrate analogues, (2) to conduct kinetic analysis of PhnZ with substrate analogues and determine kinetic parameters, (3) to conduct kinetic isotope effect studies on hydrogen-abstraction to determine if this is the rate-limiting step in the proposed mechanism, (4) to use X-ray crystallography to investigate the nature of binding of substrate analogues in the PhnZ active site to further explore substrate specificity, and (5) to use all acquired data to propose a more complete mechanism for PhnZ.

# Chapter 2

# Experimental

## 2.1 Materials

Luria-Bertani (LB), agar, ampicillin, kanamycin, and IPTG were purchased from Bio-Shop (Burlington, Ontario, Canada). *E. coli* XL1-Blue cells were purchased from Stratagene (La Jolla, California, USA). *E. coli* BL21 (DE3) cells were purchased from Novagen. All restriction endonucleases and T4 DNA ligase were purchased from New England Biolabs, except *Dpn*I which was purchased from Stratagene. The expression plasmid pET21a was obtained from Novagen. Nickel-nitrilotriacetic acid (NTA) agarose and Superflow resin and the QIAquick gel extraction kit were obtained from Qiagen, Streptactin Superflow resin was obtained from IBA Life Sciences GmbH (Göttingen, Germany). Nucleospin plasmid DNA extraction kit was obtained from Macherey-Nagel. EnzChek Phosphate assay kit was obtained from Invitrogen. Succinic acid assay kit was obtained from Megazyme®. Racemic 2-amino-1-hydroxyethylphosphonate was obtained from Peter Wyatt (Queen Mary, University of London) as well as the *R*-enantiomer, which was also obtained from Friedrich Hammerschmidt (Institute of Organic Chemistry, University of Vienna) along with all other phosphonates (**Figure 2-1**). Deionized or Milli-Q water was used for all media or buffer preparations respectively. All reagents were used as received without further modification or purification unless stated otherwise.

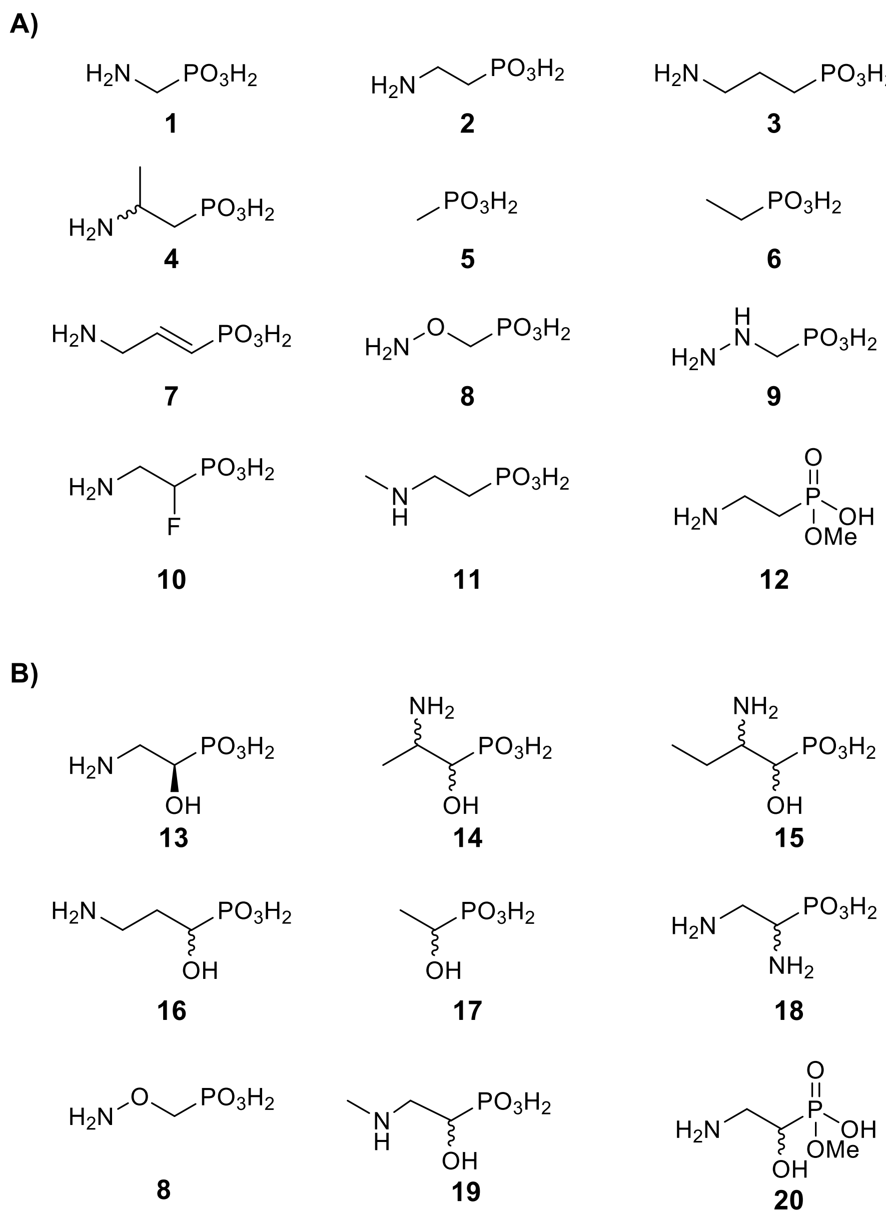


**Figure 2-1. Phosphonates tested as substrates with A) PhnY and B) PhnZ.** All phosphonates were synthesized by the Hammerschmidt group, with the exception of **17** which was also obtained from the Wyatt group.

**Table 2-1. Buffers used for purification and storage of PhnY and PhnZ.**

| Buffer | Composition |
|---|---|
| ***Lysis buffers*** | |
| PhnY lysis buffer | 20 mM Tris-HCl, 300 mM NaCl, 10 mM imidazole, pH 7.5 |
| PhnZ lysis buffer | 20 mM Tris-HCl, 300 mM NaCl, 20 mM imidazole, pH 7.5 |
| ***Ni-NTA column purification buffers*** | |
| Buffer A | 20 mM Tris-HCl, 300 mM NaCl, pH 7.5 |
| Buffer B | 20 mM Tris-HCl, 300 mM NaCl, 500 mM imidazole, pH 7.5 |
| ***Strep-Tactin column purification buffers*** | |
| Buffer W | 100 mM Tris-HCl, 150 mM NaCl, pH 8.0 |
| Buffer E | 100 mM Tris-HCl, 150 mM NaCl, 2.5 mM desthiobiotin, pH 8.0 |
| Buffer R | 100 mM Tris-HCl, 150 mM NaCl, 1 mM HABA (hydroxy-azophenyl-benzoic acid), pH 8.0 |
| ***Storage buffers*** | |
| Buffer Y | 50 mM Tris-HCl, 300 mM NaCl, 10% (wt/vol) glycerol, pH7.5 |
| Buffer T | 25 mM Tris-HCl, 150 mM NaCl, 10% (wt/vol) glycerol, pH 7.5 |
| Buffer M | 25 mM MOPS, 150 mM NaCal, 10% (wt/vol) glycerol, pH 7.0 |

## 2.2 Equipment

### 2.2.1 NMR spectroscopy

Spectra were acquired using a Bruker Avance 400 MHz spectrometer at Queen's University. $^{31}$P-NMR spectra were acquired at 400 MHz and referenced to 85% phosphoric acid at δ0.0 ppm (contained separately within a capillary). Spectra were analyzed using the Bruker TopSpin 2.0 and MestReNova software platforms.

### 2.2.2 Inductively coupled plasma-mass spectrometry (ICP-MS)

ICP-MS analysis was performed by Yoseif Makonnen (Diane Beauchemin lab, Department of Chemistry, Queen's University) on a Varian 820MS (Mulgrave, Victoria, Australia) quadrupole-based ICP-MS instrument featuring the Turner interlaced load coil configuration, which minimizes secondary discharge, allowing representative spatial profiling of the plasma. Sample introduction consisted of a MicroMist concentric nebulizer (Glass Expansion, Pocasset, USA) fitted into a Scott double-pass spray chamber and maintained at 0 °C via a computer controlled Peltier cooling system.

## 2.3 Methods

### 2.3.1 Studies on the α-ketoglutarate / Fe(II) dependent dioxygenase PhnY

#### 2.3.1.1 Heterologous expression and purification of PhnY

A synthetic *phnY* gene codon-optimized for expression in *E. coli* was expressed as previously described.[66] A plasmid encoding recombinant PhnY bearing a C-terminal hexahistidine sequence was used to transform *E. coli* BL21 (DE3) cells grown on LB-agar plates supplemented with ampicillin (final concentration of 100 µg/mL) at 37°C. A single colony was used to inoculate a 5 mL pre-culture of LB supplemented with ampicillin (final concentration of 100 µg/mL) and was grown in an air shaker for 16 hours at 37°C, 240 rpm. A 500 mL LB culture supplemented with ampicillin (final concentration of 100 µg/mL) was inoculated with the pre-culture and grown in an air shaker at 37°C and 240 rpm until the culture reached an $OD_{600}$ of 0.5-0.7. The culture was then chilled on ice for 30 minutes followed by induction with IPTG to a final concentration of 40 µM. PhnY was then expressed at 15°C for 20 hours before the cells were harvested at 4150 rpm and 4°C for 15 minutes. Immediately after the cells were harvested, they were resuspended in 4 mL of PhnY lysis buffer per g of cell pellet and lysed by three passages through a high-pressure homogenizer (Emulsiflex, model C5, Avestin, Ottawa, ON) at 15 000 psi. The lysate was subsequently clarified by centrifugation at 30 000 g, 4°C for 30 minutes. The crude extract was then filtered through a 0.45 µm filter and loaded onto a 5 mL Ni-NTA agarose column that was pre-equilibrated in 2% buffer B using an ÄKTA FPLC system. The column was washed with 10 column volumes (CV) of 2% buffer B, followed by elution of PhnY with an imidazole gradient of 2% to 100% buffer B over 5-10 CV using a flow rate of 2 mL/min while monitoring the eluent at 280 nm. The collected fractions were analyzed by SDS-PAGE and those containing PhnY were pooled and buffer was exchanged with Buffer Y at 4°C using an Amicon Ultrafiltration device. The concentration of PhnY was determined by measuring the absorbance at 280 nm using the extinction coefficient 48 485 $M^{-1}$ $cm^{-1}$ that was calculated from the amino acid sequence of PhnYHis using the ProtParam tool on the ExPASY website (http://web.expasy.org/protparam/). The purified yield of PhnY was typically 150-180 mg per litre of *E. coli* culture.

#### 2.3.1.2 Crystallography of PhnY

DLS was performed using a Protein Solutions Dynapro light scatterer and was used to ensure monodispersity of PhnY in solution and to determine its oligomeric state. Several crystallization screens were set up using the following commercially available screens (Qiagen): Classics suites I and II, PEGs suites I and II, and JCSG core suites I-IV. Crystal trays were set up by Natalie Roy using a Phoenix robot (Art Robbins Intruments). Screens were set up in 96-well plates using the sitting drop diffusion method with a 0.4 µL droplet size and 0.07 mL reservoir volume. Plates were incubated at either room temperature, 285

K, or 277 K. PhnY was used at concentrations of 8 mg/mL or 10 mg/mL and incubated with **2** or (+/-)-**10** and/or Fe(II).

### 2.3.1.3 $^{31}$P-NMR spectroscopic analysis of PhnY reactions

PhnY reactions were analyzed using $^{31}$P-NMR spectroscopy as previously described.[59] In all cases, reactions were set up in a total reaction volume of 500 µL and were incubated in an air shaker at 30°C, 240 rpm for 16 hours. PhnY reactions consisted of 1 mM substrate (**Figure 2-1, A**), freshly prepared 0.1 mM $Fe(SO_4)_2(NH_4)_2$, 2 mM α-ketoglutarate, 0.2 mM ascorbate, and 10 µM PhnY in 25 mM Tris-HCl, pH 7.0. All reactions were terminated with the addition of 10 mM sodium dithionite and 50 mM EDTA, pH 8.0, followed by 20% (vol/vol) $D_2O$ as a lock for NMR analysis. Reaction mixtures were centrifuged to remove any precipitated enzyme and the supernatant was analyzed by $^{31}$P-NMR spectroscopy (400 MHz) acquiring 500-600 scans using a delay time (D1) of 2 seconds. Chemical shifts were referenced to 85% phosphoric acid (external standard in a capillary) at 0.0 ppm.

### 2.3.1.4 Kinetic analysis of PhnY

Kinetic analysis of PhnY was performed by Nathalie Butler (honours thesis student, Zechel lab, Department of Chemistry, Queen's University) using PhnY that was expressed and purified by the author. PhnY requires α-ketoglutarate to generate the ferryl oxygen species that is responsible for α-hydroxylation of **2**. Following entry of α-ketoglutarate into the PhnY active site, it is oxidized to succinate which can be detected using the Succinic Acid Assay Kit (Megazyme, Bray, Ireland) based on the method described by Beutler[70]. In principle, the amount of succinate that is generated is stoichiometric to the amount of **2** that is converted to (*R*)-**13**. To detect the production of succinate and relate the rate of succinate production to the rate of α-hydroxylation of **2**, the assay uses a multi-step reaction pathway to monitor the consumption of NADH, which can be measured spectrophotometrically at 340 nm. The first step is the conversion of succinate to succinyl-CoA by the ATP-dependent enzyme succinyl Co-A synthetase (SCS) generating ADP and $P_i$. Pyruvate kinase (PK) then dephosphorylates PEP and transfers the phosphate to ADP producing pyruvate and ATP. L-lactate dehydrogenase (L-LDH) then reduces pyruvate to L-lactate consuming NADH and producing $NAD^+$ and L-lactate (**Figure 2-2**).

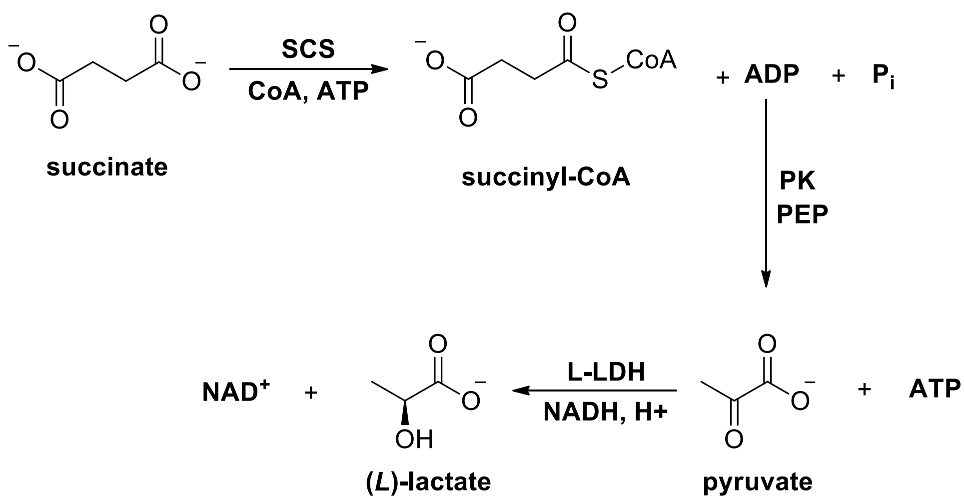


**Figure 2-2. Sequence of coupled reactions in the succinic acid assay.**

All solutions were prepared and stored according to the manufacturer's directions, and combined in the recommended proportions along with reagents required for the PhnY reaction in a total reaction volume of 200 µL. The volumes of the reagents supplied by the kit were 20 µL each of buffer, of an NADH solution, and of a solution containing ATP, PEP, and CoA, as well as 2 µL each of a solution containing PK and L-LDH, and a solution of SCS. The concentrations of the reagents required for the PhnY reaction that were used are 0.1 mM $Fe(SO_4)_2(NH_4)_2$, 2 mM α-ketoglutarate, 0.2 mM ascorbate, and varying concentrations of **2**. The reaction was then initiated with the addition of PhnY to a final concentration of 4.4 μM and the absorbance was monitored at 340 nm over 30 minutes. The slope of the linear portion of the curve was used to determine the rate of NADH consumption, which was then related to the rate of succinate production (and therefore the rate of α-hydroxylation) using the extinction coefficient for NADH at 340 nm of 6300 $M^{-1}$ $cm^{-1}$. Initial reaction rates were plotted against the concentration of **2** and the data was fitted to the Michaelis-Menten equation using GraphPad Prism 6.0 (GraphPad Software, San Diego, USA) to determine kinetic parameters.

### 2.3.2 Studies on PhnZ

#### 2.3.2.1 Heterologous expression and purification of PhnZ from pJExpress401_*phnZ*

A synthetic *phnZ* gene codon-optimized for expression in *E. coli* was expressed using methods that were previously described.[64] A plasmid encoding PhnZ bearing a C-terminal hexahistidine tag was used to transform *E. coli* BL21 (DE3) cells and grown on LB-agar plates supplemented with kanamycin (final concentration of 50 μg/mL) at 37°C. A single colony was used to inoculate a 5 mL pre-culture of LB supplemented with kanamycin (final concentration of 50 μg/mL) and was grown in an air shaker for 16 hours at 37°C, 240 rpm. A 500 mL LB culture supplemented with kanamycin (final concentration of 50 μg/mL) was inoculated with the pre-culture and grown in an air shaker at 37°C and 240 rpm until the culture reached an $OD_{600}$ of 0.5-0.7. The culture was then chilled on ice for 30 min followed by induction with IPTG to a final concentration of 200 μM. PhnZ was then expressed at 30°C and 240 rpm for 4 hours before the cells were harvested at 4150 rpm and 4°C for 15 minutes. The cell pellet was then either flash frozen using liquid nitrogen and stored at -20°C or was resuspended in PhnZ lysis buffer and the cells were lysed by three passages through a high-pressure homogenizer (Emulsiflex, model C5, Avestin, Ottawa, ON) at 15 000 psi. The lysate was subsequently clarified by centrifugation at 30 000 g, 4°C for 30 minutes. The crude extract was then filtered through a 0.45 µm filter and loaded onto a 5 mL Ni-NTA Superflow column that was pre-equilibrated in 4% buffer B using an ÄKTA FPLC system. The column was washed with 10 CV of 4% buffer B, followed by elution of PhnZ with an imidazole gradient of 4% to 100% buffer B over 10-15 CV using a flow rate of 2 mL/min while monitoring the eluent at 280 nm. The collected fractions were analyzed by SDS-PAGE and those containing PhnZ were pooled and buffer was exchanged with either buffer T (for use in crystallography) or buffer M (for kinetic analysis) using an Amicon Ultrafiltration device. If the sample was to be used for kinetic analysis, it was concentrated to ~ 200 µM, flash frozen with liquid nitrogen, and stored at -80°C until further use. If the sample was to be used for crystallographic analysis, it was subsequently concentrated to 1 mL following the removal of imidazole and loaded onto a 130 mL S-200 size exclusion column and washed through the column using buffer A while monitoring the eluent at 280 nm. Fractions containing PhnZ were pooled, buffer exchanged with buffer T,and concentrated to ~15 mg/mL. The sample was then flash frozen with liquid nitrogen and stored at -80°C until further use. The concentration of PhnZ was determined by measuring the absorbance at 280 nm using the extinction coefficient 24 660 $M^{-1}$ $cm^{-1}$ calculated from the amino acid sequence using the web-based tool ProtParam (http://web.expasy.org/protparam/). The yield of purified PhnZHis was typically 6-12 mg per litre of *E. coli* culture.

#### 2.3.2.1.1 Construction of pET21a_*phnZHis*

The *phnZ* gene with a sequence encoding a C-terminal hexahistidine tag was excised from the pJexpress401 expression plasmid using the restriction endonucleases *Nde*I and *Hind*III and subcloned into a pET21a vector digested with the same restriction endonucleases yielding pet21a_*phnZHis*. Prior to ligation, the fragments were separated by agarose gel electrophoresis (1%) and excised from the gel and purified using the QIAquick gel extraction kit according to the manufacturer's directions. The purity and concentration of both fragments was determined using agarose gel electrophoresis. Ligations were set up using 2 µL of digested pET21a, 12 µL digested *phnZ,* 1.5 µL T4 ligase, and 1X T4 ligase buffer in a total reaction volume of 20 µL. The ligation product was transformed into *E. coli* XL1-Blue and grown overnight at 37°C on LB-agar supplemented with ampicillin (final concentration of 100 µg/mL). A single colony was used to inoculate a 4 mL LB supplemented with ampicillin (final concentration of 100 µg/mL). Plasmid DNA was isolated using the Nucleospin plasmid DNA extraction kit according to the manufacturer's directions, digested with *Nde*I and *Hind*III, and analyzed by agarose gel electrophoresis to confirm ligation of *phnZHis* into the pET21a vector.

#### 2.3.2.1.2 Construction of pET21a_*StrepphnZHis*

In order to improve the purity of PhnZ, a construct was produced encoding an N-terminal Strep tag and a C-terminal hexahistidine tag yielding pET21a_*StrepphnZHis*. This construct was produced using PCR with the primers listed in **Table 2-2**. The primer For*StepPhnZHis* encodes an *Nde*I site (which includes a start codon) followed by the sequence encoding a Strep tag. The primer Rev*HisPhnZ* encodes a *Hind*III site followed by a stop codon and a portion of the N-terminal hexahistidine tag.

**Table 2-2. Primers used to amplify *StrepphnZHis*.** Restriction endonuclease sequences are underlined, sequences encoding purification tags are bolded, and the *phnZ* gene is italicized.

| Primer | Sequence (5'-3') |
|---|---|
| **For*StrepphnZHis*** | gctc<u>catatg</u>**tggtctcatccgcagttcgaaaa***gatgagcctgagcaatagcag* |
| **Rev*HisphnZ*** | gctc<u>aagctt</u>tta**gtggtgatggtg** |

PCR was performed using the following reagents: 1X Pfu Ultra buffer, 250 µM of each dNTP, approximately 1-30 ng of DNA template (1 µL of pJexpress401_*phnz* plasmid DNA isolated from *E. coli*), 0.25 µM of each primer, and 1 µL of Pfu Ultra polymerase (Stratagene) in a 50 µL reaction volume. A "hot-start" initiation was used and the PCR was performed using an Eppendorf Mastercycler® ep Gradient thermal cycler following the program described in **Table 2-3.**

**Table 2-3. Thermal cycler program used to amplify Strep*phnZHis*.**

| ***Step*** | ***Program*** |
|---|---|
| **1** | 5 min at 95°C |
| **2** | 0.5 min at 95°C |
| **3** | 0.5 min at 62°C |
| **4** | 1 min at 72°C |
| **5** | Go to step 2, 30 times |
| **6** | 5 min at 72°C |

Agarose gel electrophoresis was used to confirm the amplification *StrepphnZHis*. Both *StrepphnZHis* and pET21a were digested with *Nde*I and *Hind*III then gel purified using the QIAquick gel extraction kit. The purity and concentration of both fragments was determined using agarose gel electrophoresis. Ligations were set up using 5 µL of digested pET21a, 2 µL digested *StrepphnZHis*, 1.5 µL T4 ligase, and 1X T4 ligase buffer in a total reaction volume of 20 µL. The ligation product was transformed into chemically competent *E. coli* XL1-Blue and grown overnight at 37°C on LB-agar supplemented with ampicillin (final concentration of 100 µg/mL). A single colony was used to inoculate a 4 mL LB supplemented with ampicillin (final concentration of 100 µg/mL). Plasmid DNA was isolated using the Nucleospin plasmid DNA extraction kit according to the manufacturer's directions, digested with *Nde*I and *Hind*III, and analyzed by agarose gel electrophoresis to confirm ligation of *StrepphnZHis* into the pET21a vector.

**2.3.2.1.3 Optimization of PhnZ production**

Expression of PhnZ as described above in **section 2.3.2.1** was not always ideal (discussed in the **Results**) and new plasmids were constructed (described below) in the interest of improving expression conditions. In both cases, optimal expression conditions were established by transforming the new plasmid construct into *E. coli* BL21 (DE3) and incubating overnight at 37°C on LB-agar supplemented with ampicillin (final concentration of 100 µg/mL). A single colony was then used to inoculate 1 mL LB pre-cultures supplemented with ampicillin (final concentration of 100 µg/mL) and were subsequently grown overnight in an air shaker at 37°C, 240 rpm. Several 100 mL LB cultures supplemented with ampicillin (final concentration of 100 µg/mL) were inoculated with the pre-cultures and grown in an air shaker at 37°C and 240 rpm until they reached an

$OD_{600}$ of 0.5-0.7. The cultures were then chilled on ice for 30 min followed by induction while varying concentrations of IPTG, expression temperatures, and expression duration to determine optimal expression conditions. Uninduced and induced samples were analyzed by SDS-PAGE to determine protein production levels.

#### 2.3.2.1.4 Purification of PhnZHis and StrepPhnZHis from pET21a

PhnZHis and StrepPhnZHis were expressed and purified from pET21a using the method described for purification of PhnZHis from pJExpress401_*phnZ*, however the expression conditions were optimized to expression at 37°C for 4 hours following induction with 0.5 mM IPTG. StrepPhnZHis was purified using a 5 mL Ni-NTA Superflow column as described above, and subsequently purified using a 2 mL Strep-Tactin Superflow gravity column. Elution fractions from the Ni-NTA Superflow column that were found to contain protein (monitored at 280 nm) were pooled and concentrated to approximately 1 mL using an Amicon ultrafiltration device. The concentrate was then loaded onto a 2 mL Strep-Tactin Superflow column pre-equlibrated with buffer W. The column was subsequently washed with 4 column volumes of buffer W, and eluted from the column using 6 sequential half column volumes of buffer E. The column was regenerated with three sequential washes of 5 column volumes of buffer R. All steps were performed by gravity at 4°C. All fractions were analyzed by SDS-PAGE and StrepPhnZHis-containing fractions were pooled and buffer exchanged with buffer T using an Amicon filtration device. The concentration of StrepPhnZHis was determined by measuring the absorbance at 280 nm using the extinction coefficient 29 910 $M^{-1}$ $cm^{-1}$. StrepPhnZHis was typically concentrated to 200 µM, aliquoted to 100 µL, and flash frozen using liquid nitrogen and stored at -80°C for several weeks without significant loss of activity. The yield of purified StrepPhnZHis was typically 8-14 mg per litre of *E. coli* culture.

**2.3.2.2 Creation of the PhnZ variant Y24/E27**

A variant of PhnZ with two mutations in the active site was generated to study the structure-function relationship between two important active site residues (Y24 and E27). The QuikChange site-directed mutagenesis protocol (Stratagene, Cedar Creek, Texas, USA) was followed to introduce these mutations using PCR. Mutagenic primers were designed to introduce the E27A mutation into the plasmid encoding the PhnZ variant Y24F and these are listed in **Table 2-4.**

**Table 2-4. PhnZ QuikChange mutagenic primers.** Mutated codons are shown in uppercase letters; Y24F is bolded and E27A is underlined.

| **Substitution** | **Mutagenic primer (5'-3')** |
|---|---|
| **Y24F/E27A** | For: ctcgcgacttggac**TTC**atcggtGCGgcg<br>Rev: cgcCGCaccgat**GAA**gtccaagtcgcgag |

PCR reactions contained final concentrations of the following reagents: 1X Pfu Ultra buffer, 200 µM of each dNTP, approximately 1-30 ng of DNA template (3 µL of 100-fold diluted pJexpress401_*phnz* plasmid DNA isolated from *E. coli*), 0.25 µM of each primer, and 1 µL of Pfu Ultra polymerase (Stratagene) in a 50 µL reaction volume. A "hot-start" initiation was used and the PCR was performed using an Eppendorf Mastercycler® ep Gradient thermal cycler following the program described in **Table 2-5.**

**Table 2-5. PCR program to generate *phnZY24F/E27A*.**

| Step | Program |
|---|---|
| **1** | 5 min at 96°C |
| **2** | 0.5 min at 96°C |
| **3** | 1 min at 55°C |
| **4** | 4.5 min at 68°C |
| **5** | Go to step 2, 18 times |
| **6** | 10 min at 68°C |

Immediately following PCR, the restriction enzyme *Dpn*I was then added to the reaction mixture and incubated for 1 hour at 37°C to digest parental plasmid DNA. PCR products were analyzed using agarose gel electrophoresis to confirm amplification of the plasmid. PCR products with amplified plasmids were transformed into chemically competent *E. coli* XL1-Blue cells and grown on LB-agar supplemented with kanamycin (final concentration of 50 µg/mL) at 37°C overnight. A single colony was used to inoculate 4 mL of LB supplemented with kanamycin (final concentration of 50 µg/mL) and grown overnight in an air shaker at 37°C and 240 rpm. Plasmid DNA was isolated using the Nucleospin plasmid DNA extraction kit according to the manufacturer's directions, digested with *Nde*I and *Hind*III, and analyzed by agarose gel electrophoresis to confirm the presence of the *phnZ* gene and the mutation was confirmed through sequencing using the primers pJexpress_Seqfor2 5'-cgagcttcatgcacagtgaaatc-3' and pJexpress_Seqrev2 5'-cgaaaggctcagtcagtcgaaagactgg-3'. For ease of purification, *phnZY24F/E27A* was subsequently subcloned into pET21a using the method described above to subclone *StrepphnZHis* into pET21a to generate pET21a_*StrepphnZY24F/E27AHis*.

#### 2.3.2.3 Absorbance spectra of PhnZ and variants

Absorbance spectra for all samples were measured from 260 – 700 nm (1 nm steps) on a plate reader using a 96-well quartz plate. Samples of PhnZ, PhnZ Y24F, and PhnZ D161A consisted of 200 µM protein in 20 mM Tris, pH 7.5, 300 mM NaCl. For PhnZ bound to (*R*)-**13**, 200 µM PhnZ was mixed with 4 mM substrate and incubated at 4°C for 30 min before the spectrum was measured.

#### 2.3.2.4 ICP-MS analysis of metal ion content in PhnZ variants

ICP-MS was used to analyze the metal ion content of PhnZ variants. Dialysis buffer was treated with Chelex-100 to chelate residual metal ions. The dialysis buffer, 25 mM Tris-HCl, 35 mM NaCl, pH 7.5, was treated with Chelex for 4 hours followed by filtration through a 0.20 µm filter to remove the Chelex resin. Purified PhnZ was dialyzed against the Chelex-treated buffer using Slide-A-Lyzer dialysis cassettes (Thermo Scientific, Rockford, IL, USA) and concentrated using an Amicon ultrafiltration device. Analysis was performed by Yoseif Makonnen (Diane Beauchemin lab, Department of Chemistry, Queen's University). The optimal plasma operating conditions and measurement parameters were the following: Argon plasma flow, 18.0 L/min; argon auxiliary flow rate, 1.8 L/min; argon nebulizer flow rate, 1.0 L/min; argon sheath flow rate, 0.02 L/min; RF power, 1.5 kW; sample uptake rate, 300 µL/min; sampling depth, 5.0 mm. A calibration curve was prepared using standard solutions of iron and sulfur in Chelex-treated dialysis buffer over a 0.1-1000 µg/L range. A 5 µg/L solution of Sc was used as an internal standard. Three replicates of five PhnZ variants (H58A, E27A, D161A, Y24F, H80A) at various enzyme concentrations were analyzed for $^{57}Fe$.

### 2.3.2.5 $^{31}$P-NMR spectroscopic analysis of PhnZ reactions

PhnZ reactions were analyzed using $^{31}$P-NMR spectroscopy as previously described.[59] In all cases, reactions were set up in a total reaction volume of 500 µL and were incubated in an air shaker at 30°C, 240 rpm for 16 hours. PhnZ reactions consisted of 1 mM substrate (**Figure 2-1, B**), freshly prepared 0.1 mM $Fe(SO_4)_2(NH_4)_2$, and 5 µM PhnZ in 25 mM Tris-HCl, pH 7.0. All reactions were terminated with the addition of 10 mM sodium dithionite and 50 mM EDTA, pH 8.0. 20% (vol/vol) $D_2O$ was added as a lock for NMR analysis. Reaction mixtures were centrifuged to remove any precipitated enzyme and the supernatant was analyzed by $^{31}$P-NMR. Chemical shifts were referenced to 85% phosphoric acid (external standard in a capillary) at 0.0 ppm.

### 2.3.2.6 pH profile of PhnZ

The activity of PhnZ was assayed over a range of pH 5 – 8.5 to produce a pH profile. The activity of PhnZ was assayed using the malachite green assay using the method described by Pegan and coworkers.[71] The assay uses an acidic malachite green development solution to detect free $P_i$. This solution was prepared by adding 15 mL of 36 N $H_2SO_4$ to 75 mL of $H_2O$ and allowing this solution to cool to room temperature before adding 110 mg of malachite green producing a clear, orange solution. Prior to use, 1 mL of this solution was mixed with 250 µL of 7.5% (wt/vol) ammonium molybdate and 20 µL of 11% (vol/vol) Tween 20. PhnZ reactions were carried out in the following buffers (50 mM): sodium acetate, pH 5.0 and 5.5; MES, pH 6.0 and 6.5; MOPS, pH 7.0; and Tris-HCl, pH 7.5, 8.0, and 8.5. All reactions consisted of 50 mM buffer, 1 mM (*R*)-**13**, 200 µM $Fe(SO_4)_2(NH_4)_2$, and 2 µM PhnZ. Reaction components were combined in a 96-well plate to a final reaction volume of 100 µL and allowed to mix at 50 rpm for 5 minutes before being quenched with the malachite green development solution in a 1:4 ratio (25 µL to a 100 µL reaction). Following quenching, the dye was allowed to develop for 10 min at room temperature with shaking at 50 rpm before the absorbance was measured at 623 nm using a SpectraMax microplate reader. The absorbance was related to the amount of $P_i$ that was generated using $P_i$ standard curves that were produced for each buffer. All reactions for the $P_i$ standard curves consisted of 50 mM buffer, 1 mM (*R*)-**13**, 200 µM $Fe(SO_4)_2(NH_4)_2$, and various concentrations of $P_i$ (from a stock solution of $K_2HPO_4$) to a final reaction volume of 100 µL. Reactions were quenched and analyzed as described for the PhnZ reactions. Standard curves were created in GraphPad Prism 6.0 (GraphPad Software, San Diego, USA).

### 2.3.2.7 Kinetic analysis of PhnZ

The activity of PhnZ was measured using the EnzChek Phosphate Assay Kit based on the method described by Webb.[72] As $P_i$ is generated by PhnZ, purine nucleoside phosphorylase (PNP) converts $P_i$ and the substrate 2-amino-6-mercapto-7-methylpurine riboside (MESG) to α-D-ribosyl-1-phosphate and 2-amino-6-mercapto-7-methylpurine, the latter of which can be monitored at 360 nm (**Figure 2-3**).

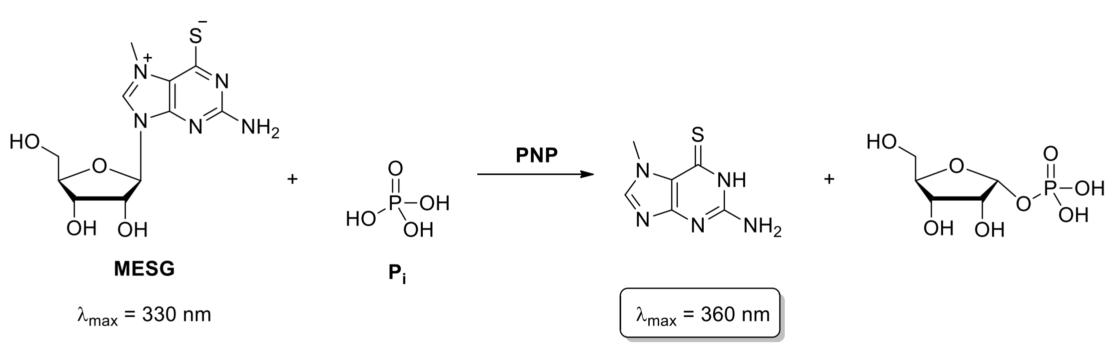


**Figure 2-3. Reaction scheme for the EnzChek Phosphate assay.**

All experiments were performed following the EnzChek manual, however the reaction buffer provided with the kit was replaced with 25 mM MOPS pH 7.0 to account for the pH optimum of PhnZ. The final concentrations of the reaction components were the following: 200 µM MESG, freshly prepared 200 µM $Fe(SO_4)_2(NH_4)_2$, 1U PNP, and 10 µM PhnZ in a total reaction volume of 500 µL. All reaction components were combined in a cuvette and incubated for 10 minutes at 25°C to deplete the reaction mixture of free $P_i$. The reaction was then initiated with the addition of substrate. The reaction was monitored every 0.1 seconds at 360 nm and 25°C using a Cary UV-Vis Bio 300 spectrophotometer (Varian). The molar extinction coefficient for the reaction product 2-amino-6-mercapto-7-methylpurine at pH 7.0 was determined by measuring the difference in absorbance at 360 nm between a blank and reactions of PNP with four concentrations of $P_i$ (5, 10, 15, 20 µM). The slope of this plot was used to determine an extinction coefficient of 7021 $M^{-1}$ $cm^{-1}$ at pH 7.0, which was used to determine initial reaction rates. Initial reaction rates were plotted against substrate concentration and the data was fitted to the Michaelis-Menten equation using GraphPad Prism 6.0 (GraphPad Software, San Diego, USA) to determine kinetic parameters.

#### 2.3.2.8 Kinetic isotope effect on hydrogen abstraction by PhnZ

Michaelis-Menten plots were generated for the reaction of PhnZ of (*R*)-**13** and 1-D-(*R*)-**13** using the EnzChek phosphate assay and following the method described in **section 2.3.2.7**. Initial rates were determined at 0.05, 0.1, 0.15, 0.5 1.0 and 1.5 mM of each substrate and all data points were performed in triplicate, except those at 0.1 and 1.5 mM substrate which were performed in a single trial.

#### 2.3.2.9 Crystallization and X-ray data collection of PhnZ with substrate analogues

PhnZ was concentrated to 15 mg/mL for crystallization in 25 mM Tris-HCl, 150 mM NaCl, 10% (wt/vol) glycerol, pH 7.5. Crystals were grown under aerobic conditions using the hanging drop vapour diffusion method and typically grew after 4-7 days at room temperature. For co-crystallization of PhnZ with substrate analogues, PhnZ (10 mg/mL) was pre-equilibrated on ice for 1 hour with substrate in a 1:10 molar ratio. The final condition for PhnZ co-crystallized with 1-HEP contained 0.1 M tris pH 7.5, 0.2 M sodium acetate, 30% PEG 4000. The reservoir was mixed in a 1:1 ratio (2 µL + 2 µL) with PhnZ-substrate complex. The final condition for PhnZ co-crystallized with 1-OH-2-APP contained 0.1 M bis-tris pH 6.5, 22% PEG 5000 MME in the well solution. The reservoir was mixed in a 1:1 ratio (2 µL + 2 µL) with PhnZ-substrate complex. The final condition for PhnZ co-crystallized with 1-OH-3-APP contained 0.1 M bis-tris pH 6.5, 24% PEG 5000 MME in the well solution. The reservoir was mixed in a 1:1 ratio (5 µL + 5 µL) with PhnZ-substrate complex and 1 µL of 0.1 M spermidine was added to the drop.

All diffraction data were collected at 100 K using the well solution plus 20% glycerol as a cryoprotectant. Diffraction data were collected at the 23 ID-B beamline at the Advanced Photon Source (Argonne National Laboratory, Chicago, IL, USA) equipped with a MARMOSAIC 300 CCD detector. Data were indexed and scaled using XDS.[73] All crystals belonged to the primitive orthrombic space group $P2_12_12_1$ with the following cell dimensions: PhnZ co-crystallized with 1-HEP, $a$ = 68.0, $b$= 75.2, and $c$= 83.2 Å; PhnZ co-crystallized with 1-OH-2-APP, $a$ = 68.5, $b$= 75.4, and $c$= 83.7 Å; and PhnZ co-crystallized with 1-OH-3-APP $a$ = 68.5, $b$= 75.5, and $c$= 82.2 Å. All structures had two molecules in the asymmetric unit with Mathews[74] coefficients of 2.37$Å^3Da^{-1}$ (48.2 % solvent), 2.41

Å$^3$Da$^{-1}$ (49.0% solvent), and 2.37 Å$^3$Da$^{-1}$ (48.2% solvent) for PhnZ co-crystallized with 1-HEP, 1-OH-2-APP, and 1-OH-3-APP, respectively.

#### 2.3.2.9.1 Structure solution and refinement of PhnZ co-crystallized with substrate analogues

The structures of PhnZ co-crystallized with substrate analogues diffracted to the following resolutions: 1-HEP, 1.7 Å; 1-OH-2-APP, 1.9 Å; and 1-OH-3-APP, 1.9 Å. All structures were solved by molecular replacement using Phaser[75] using molecule A from the structure of PhnZ co-crystallized with 1-OH-2-AEP (PDB ID: 4MLN) with the bound substrate and iron cofactors removed as a search model and the structure was refined using PHENIX[76]. Missing residues were manually built in Coot[77] and all substrate analogues were subsequently added to the unambiguous difference density in the active site. Coordinates for all substrates were generated in Chem3D Pro 12.0.

# Chapter 3

# Results

## 3.1 Studies on the α-ketoglutarate / Fe(II) dependent dioxygenase PhnY

### 3.1.1 Expression and purification of PhnY

#### 3.1.1.1 Optimization of PhnY purification conditions

Initially, previously established procedures were used for the heterologous expression and purification of PhnY from *E. coli*.[66] Optimized expression conditions had been established for both PhnY bearing a C-terminal Strep tag (PhnYStrep) and PhnY bearing a C-terminal hexahistidine (PhnYHis), and in both cases expression was induced with 40 μM IPTG at $OD_{600}$ = 0.5-0.7 and expression at 15°C and 240 rpm for 20 hours. Up to 16 mg and 64 mg of PhnYStrep and PhnYHis, respectively, could be isolated from a 1 L *E. coli* culture using these conditions. Although PhnYStrep is produced in lower yields, it has been found to be more stable and therefore was typically used. In this thesis, the author expressed and purified PhnYHis. Although it is possible to isolate up to 64 mg of PhnYHis from a 1 L *E. coli* culture, it is less stable and ensuring the production of soluble protein was often problematic. Analysis of a typical purification of PhnYHis by 12% SDS-PAGE shows that only small quantities of the enzyme, which appears as a band at approximately 31.1 kDa, can be isolated (**Figure 3-1, lanes 5-10)**. Additionally, analysis of the clarified lysate shows that a large portion of PhnYHis is visible in the insoluble fraction (**Figure 3-1, lane 2**) and a very small amount is visible in the soluble lysate fraction (**Figure 3-1, lane 3**).

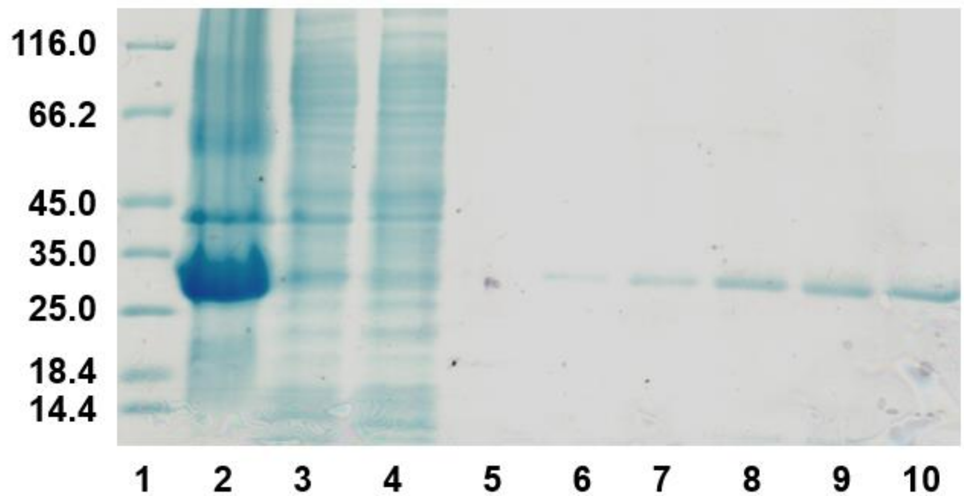


**Figure 3-1. SDS-PAGE (12%) analysis of PhnY purification. (1)** Protein molecular weight ladder 26610 (Thermo Scientific), molecular weights indicated to the left of the bands in kDa, **(2)** insoluble cell lysate, **(3)** cleared lysate, **(4)** flow-through upon washing the column with lysis buffer, and **(5) – (10)** elution fractions.

The large amount of insoluble PhnY that is produced in comparison to soluble PhnY suggested that either the expression conditions were not ideal for PhnY stability or that PhnY began to precipitate out of solution at some point after expression and before purification. Typically, the *E. coli* cell pellet was flash-frozen and stored at -20°C after expression and purified at a later time. Analysis by SDS-PAGE indicated that when the cell pellet is not frozen and PhnY is purified immediately after expression, a greater portion of PhnY is found in the soluble fraction rather than the insoluble fraction of the cell lysate (**Figure 3-2,** lanes **2** and **3**). Although SDS-PAGE analysis suggested that a larger quantity of purified PhnY could be isolated (**Figure 3-2,** lanes **5-10**), analysis of the flow-through after the column is washed with lysis buffer suggested that PhnY does not bind well to the column and was being washed off using low concentrations of imidazole (20 mM) (**Figure 3-2**, lane **4**).

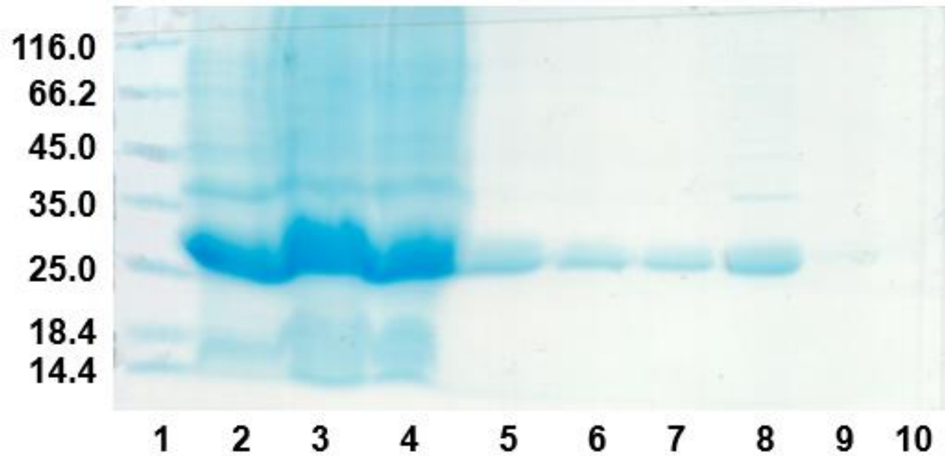


**Figure 3-2. SDS-PAGE (12%) analysis of PhnY purification immediately after protein expression. (1)** Protein molecular weight ladder 26610 (Thermo Scientific) with molecular weights indicated to the left of each band in kDa, **(2)** insoluble cell lysate, **(3)** cleared lysate, **(4)** flow-through upon washing the column with lysis buffer, and **(5) – (10)** elution fractions.

To circumvent the low binding affinity of PhnY for the Ni-NTA resin, the concentration of imidazole in the lysis buffer was decreased from 20 mM to 10 mM, which ensured that PhnY remained bound to the column but unspecific proteins were still washed off the column. After the cleared lysate was loaded onto the column, the column was washed with this buffer until the absorbance at 280 nm remained steady, suggesting that unspecific proteins had been washed off the column.

Purifying PhnY immediately after expression and decreasing the concentration of imidazole in the lysis and wash buffers greatly improved the yield of PhnY that could be achieved. Analysis by SDS-PAGE of a purification that included these alterations to the purification procedure resulted in the isolation of large quantities of purified PhnY (**Figure**

**3-3,** lanes **5-19**). These results were highly reproducible and yields of 150-180 mg per litre of *E. coli* culture were typically achieved.

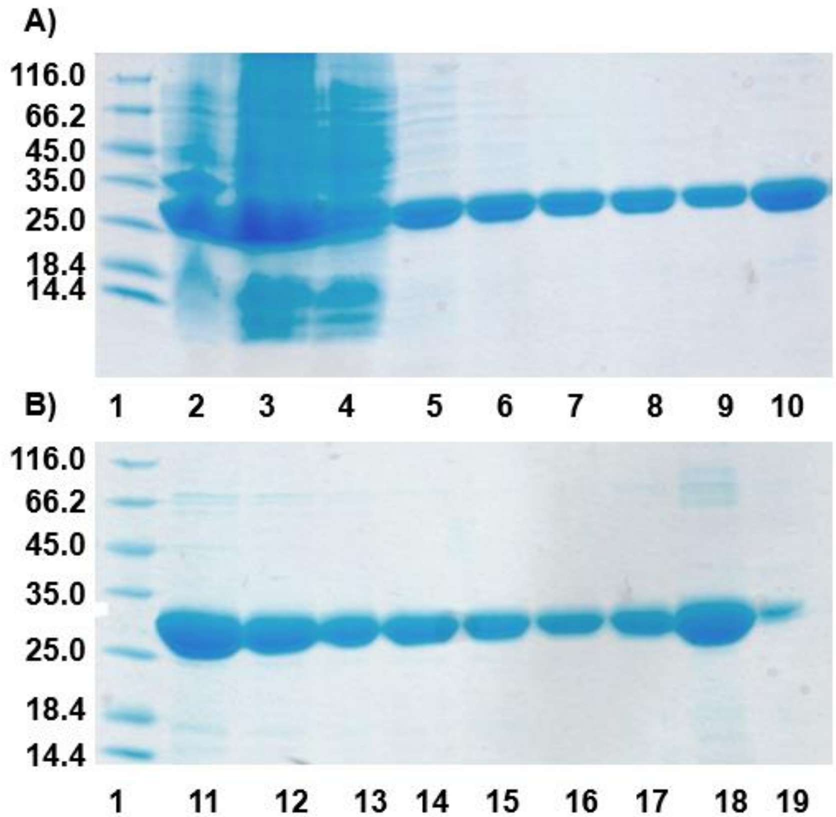


**Figure 3-3. SDS-PAGE (12%) analysis of PhnY protein production after optimization of purification procedure.** **(1)** Protein molecular weight ladder 26610 (Thermo Scientific), molecular weights indicated to the left of the bands in kDa, **(2)** insoluble cell lysate, **(3)** cleared lysate, **(4)** flow-through upon washing the column with lysis buffer, and **(5) – (19)** elution fractions.

### 3.1.1.2 Optimization of PhnY stability

Immediately following purification, PhnY was concentrated and buffer exchanged with a buffer containing 50 mM Tris-HCl, 10% (wt/vol) glycerol, pH 7.5. However, PhnY was very unstable in this buffer and would rapidly precipitate out of solution above concentrations of approximately 50 µM. In the interest of developing a buffer system in which PhnY could remain stable, the content of imidazole and NaCl was varied in the buffer described above. Immediately following purification, PhnY is in a buffer containing 300 mM NaCl and approximately 300 mM imidazole and it was believed that either NaCl or imidazole were responsible for the precipitation of PhnY. When PhnY was buffer exchanged with a buffer containing no NaCl, precipitation still occurred. However, when PhnY was buffer exchanged with a buffer containing 300 mM NaCl and no imidazole, a concentration of up to 2 mM (66.2 mg/mL) could be achieved. Studies of PhnY using dynamic light scattering (DLS) suggested that a concentrated sample of PhnY that was diluted in buffer B underwent large amounts of aggregation. However a concentrated sample of PhnY diluted in buffer Y (50 mM Tris-HCl, 300 mM NaCl, 10% (wt/vol) glycerol, pH 7.5) was a monomer in solution with a monodispersity of 99.3%, suggesting that this was a buffer in which PhnY was stable and aggregation was not occurring.

### 3.1.2 Towards obtaining a crystal structure of PhnY

Three important factors to consider when producing a protein sample for use in crystallography are purity, homogeneity, and monodispersity. Additionally, protein concentrations of 10-15 mg/mL are generally required for crystallization of small proteins that are 30 kDa or less.[78] The optimized conditions for the expression, purification, and stability of PhnY as described above permitted the production of a protein sample that was in excess of 95% purity and 99.3% monodispersity, with achievable concentrations of up to 2 mM (62.2 mg/mL) (**Figure 3-4**). These results suggested that PhnY would likely be a good candidate for crystallography.

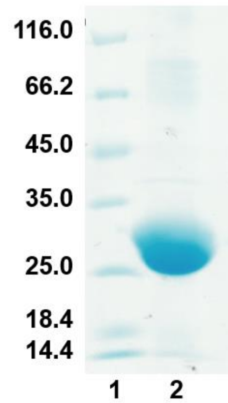


**Figure 3-4. SDS-PAGE analysis (12%) of concentrated PhnY. (1)** Protein molecular weight ladder 26610 (Thermo Scientific), molecular weights indicated to the left of the bands in kDa, **(2)** concentrated sample of purified PhnY.

Several attempts were made to crystallize PhnY, however none of these were successful. Several commercially available screens were set up at room temperature, but rapid precipitation of PhnY was observed in all cases. The screens were repeated at 285K and 277K to slow down the rate of precipitation, however precipitation also occurred in these cases. All screens were set up with apoenzyme, or PhnY pre-incubated with **2** or (±)-**10** and/or Fe(II). Attempts to incubate PhnY with an excess of α-ketoglutarate resulted in rapid precipitation that also occurred when **2** and/or Fe(II) were present (regardless of the order of addition), and it was therefore omitted from all crystallization screens. Further attempts to crystallize PhnY were abandoned.

### 3.1.3 Analysis of the substrate specificity of PhnY by $^{31}$P-NMR spectroscopy

PhnY was reacted with **2** in the presence of Fe(II), α-ketoglutarate and ascorbate for 16-20 hours whereupon the reaction mixture was analyzed using $^{31}$P-NMR spectroscopy. The PhnY substrate, **2**, exhibits a chemical shift at approximately δ 18.1

ppm (**Figure 3-5**, **A**) and when it is converted to (*R*)-**13**, there is a shift upfield to approximately δ 14.8 ppm (**Figure 3-5**, **B**).

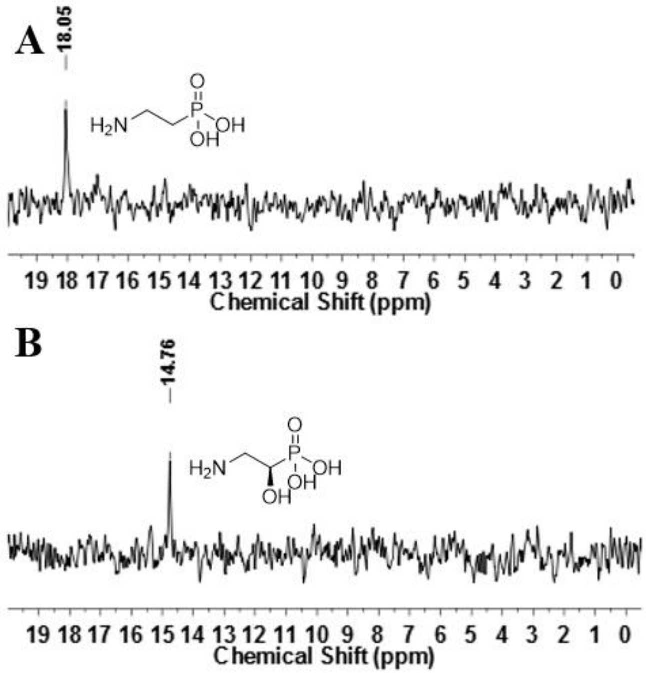


**Figure 3-5. $^{31}$P-NMR spectroscopic analysis of the PhnY reaction. A)** Enzyme-free control, **2** at δ18.1 ppm and **B)** PhnY reaction, (*R*)-**13** at 14.8 ppm. Reactions were carried out with 1 mM substrate and 10 µM PhnY at pH 7.0. Signals are not referenced to 85% $H_3PO_4$.

Several substrate analogues (**Figure 2.2, A**) were synthesized by members of the Hammerschmidt group (University of Vienna) to investigate the substrate specificity of PhnY. These substrates were synthesized to investigate the effect of the amino group (**5**, **6**), chain length (**1**, **3**, **4**), rigidity (**7**), fluorination at C1 (**10**) and methylation (**11**, **12**). Two other analogues (**8**, **9**) were also tested. Reactions with **5** and **6** were carried out previously, and neither were found to be substrates for PhnY.[66] Reactions with all other substrate analogues were set up and terminated in the same way as the reactions with **2** and were analyzed by $^{31}$P-NMR spectroscopy. In all cases an enzyme-free control as well as a reaction with PhnY was set up. In all cases, no change in intensity of the NMR signals and there was no appearance of a new signal to indicate a reaction with PhnY (**Table 3-1**). All spectra are presented in **Appendix A**.

**Table 3-1. $^{31}$P-NMR chemical shifts of EF-controls and PhnY reactions with substrate analogues.** All signals referenced to 85% $H_3PO_4$ at 0.0 ppm.

| Structure | Chemical shift (ppm) EF-control | Chemical shift (ppm) PhnY reaction | Reaction |
|---|---|---|---|
| 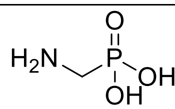 **1** | 10.16 | 10.17 | No |
| 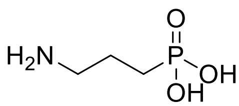 **3** | 22.8 | 22.5 | No |
| 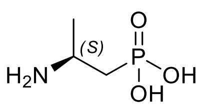 (*S*)-**4** | 16.86 | 16.85 | No |
| 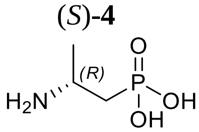 (*R*)-**4** | 16.84 | 16.86 | No |
| 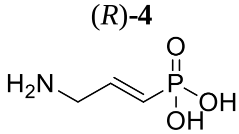 **7** | 8.45 | 8.43 | No |
| 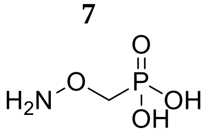 **8** | 12.54 | 12.47 | No |
| 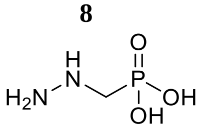 **9** | 13.31 | 13.27 | No |
| 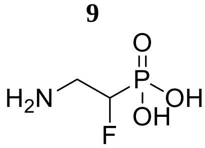 **10** | 8.32 (d, *J* = 57.8 Hz) | 8.31 (d, *J* = 57.1 Hz) | No |

| | | | |
|---|---|---|---|
| 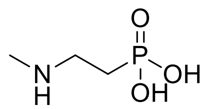 **11** | 17.94 | 17.39 | No |
| 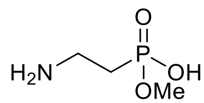 **12** | 22.53 | 22.60 | No |

### 3.1.4 Kinetic analysis of PhnY

Kinetic analysis of PhnY was carried out by Nathalie Butler (honours thesis student, Queen's University) using PhnY produced by the author as described above. The initial rate of α-hydroxylation by PhnY at various concentrations of **2** was monitored using the succinic acid assay kit and the consumption of NADH was monitored at 340 nm for 30 minutes. To ensure efficient coupling by the multiple coupling enzymes involved in the assay, the concentration of PhnY was doubled to determine the effect this would have on the initial rate. The rate doubled when the concentration of PhnY doubled, and the coupling enzymes were therefore found not to be rate-limiting.

Kinetic analysis was then performed using **2** as the substrate. Initial rates were plotted against the concentration of **2** and the data was fitted with the Michaelis-Menten equation (**Figure 3-6**). The resulting kinetic parameters are listed in **Table 3-2.**

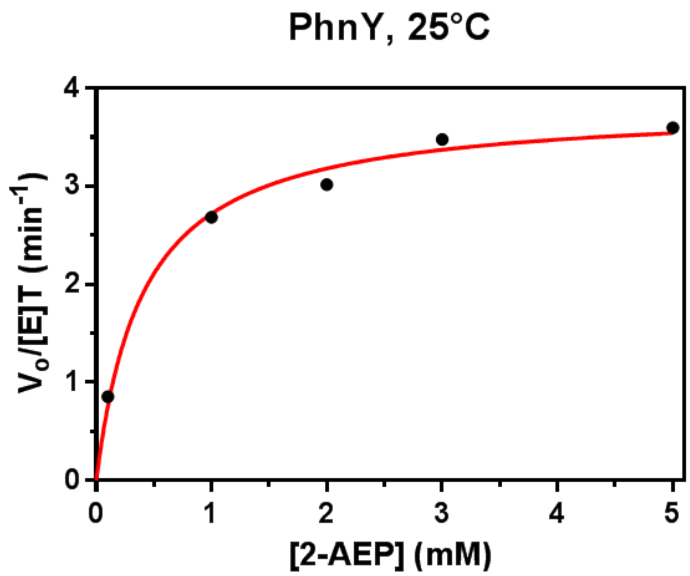


**Figure 3-6. Michaelis-Menten plot for PhnY with 2 (2-AEP).** All data points represent a single trial.

**Table 3-2. Kinetic parameters for the reaction of PhnY with 2.**

| **Kinetic parameter** | **Value** |
|---|---|
| $k_{cat}$ (min$^{-1}$) | 3.8 ± 0.1 |
| $K_M$ (mM) | 0.41 ± 0.08 |
| $k_{cat}/K_M$ (min$^{-1}$ mM$^{-1}$) | 9.3 ± 1.8 |

### 3.2 Studies on PhnZ

#### 3.2.1 Expression and purification of PhnZ

The *phnZ* gene bearing a C-terminal hexahistidine tag (PhnZHis) was expressed in *E. coli* BL21 (DE3) cells following induction with IPTG as previously described using affinity chromatography.[66] Analysis of the insoluble and soluble fractions of the cleared lysate were analyzed by SDS-PAGE (**Figure 3-7**, lanes **2** and **3**) as well as the flow-through (**Figure 3-7**, lane **4**) and elution fractions (**Figure 3-7**, lanes **5-10**). PhnZ appears as a band on the gel at approximately 22.4 kDa. Very reasonable yields of 6-12 mg per litre of culture could be obtained using this procedure, however a new construct was produced to improve expression conditions (**section 3.2.1.1**) and another to enable orthogonal affinity purification to obtain improved purity (**section 3.2.1.2**).

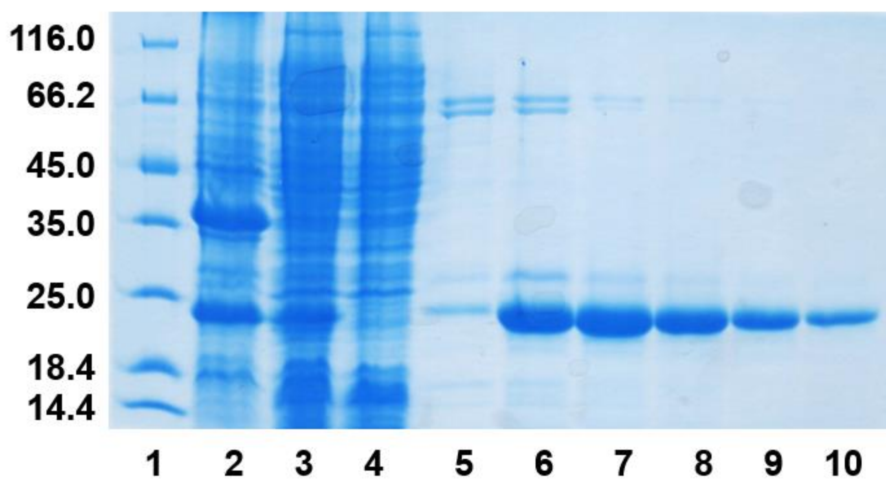


**Figure 3-7. SDS-PAGE (12%) analysis of PhnZHis purification. (1)** Protein molecular weight ladder 26610 (Thermo Scientific), molecular weights indicated to the left of the bands in kDa, **(2)** insoluble cell lysate, **(3)** cleared lysate, **(4)** flow-through upon washing the Ni-NTA column with lysis buffer, and **(5) – (10)** imidazole elution fractions. PhnZ appears as a band at 22.4 kDa.

#### 3.2.1.1 Construction of pET21a_*phnZHis*

The expression of PhnZHis from the pJExpress401 vector was inconsistent and no expression was observed on several occasions.  For this reason, the *phnZ* gene was sub-cloned into the expression vector pET21a that contains the stronger T7 promoter compared to the T5 promoter of the pJExpress401 vector.  The pJExpress401_*phnZ* plasmid and the pET21a vector were digested with the restriction endonucleases *Nde*I and *Hind*III (**Figure 3-8**, **A**) and subsequently agarose gel-purified to obtain the desired fragments (**Figure 3-8**, **B**).  Bands of 5378 bp and 593 bp were visualized using agarose gel electrophoresis corresponding to digested pET21a and *phnZHis*, respectively.

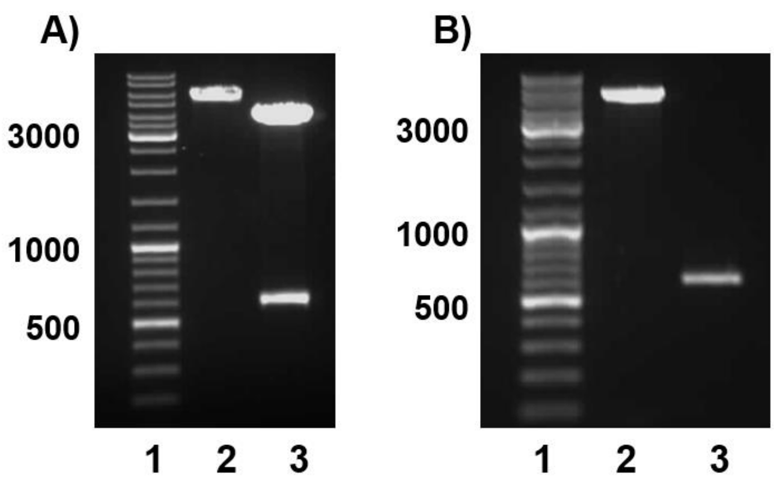


**Figure 3-8.  1% agarose gel of fragments used for the ligation of pET21a and *phnZHis*.** Lane 1 in both **A)** and **B)** is the DNA ladder SM0333 (Fermentas) with the length (bp) of the brighter bands indicated to their left; the other fragments are: 10000, 8000, 6000, 5000, 4000, 3500, 2500, 2000, 1500, 1200, 900, 800, 700, 600, 400, 300, 200, and 100 bp. **A)** Agarose gel electrophoresis of pET21a (**2**) and pJexpress401_*phnZ* (**3**) digested with *Nde*I and *Hind*III; **C)** agarose gel electrophoresis of digested and gel-purified pET21a (**2**) and pJexpress401_*phnZ* (**3**).

The two fragments were ligated together using standard procedures and the concentrations of the fragments estimated from the gel in **Figure 3-8, B.** Ligation products were transformed into XL1-Blue *E. coli* cells and grown overnight. Approximately 30 colonies were obtained and six were selected to grow in liquid culture to produce plasmid DNA. The plasmid DNA was isolated and digested with NdeI and HindIII to confirm the ligation of *phnZHis* into pET21a and all six clones were found to be positive (**Figure 3-9**).

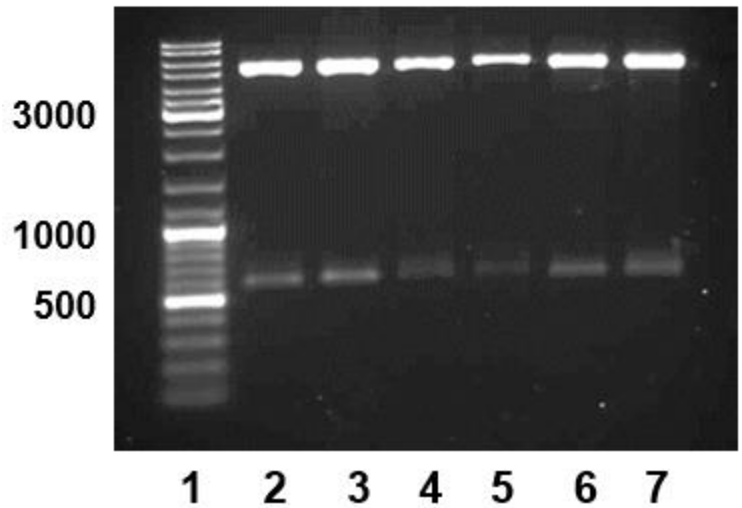


**Figure 3-9. 1% agarose gel of pET21a_*phnZHis* clones.** Lane **1** is the DNA ladder SM0333 (Fermentas) with the size of the brighter bands indicated to their left; the other fragments are: 10000, 8000, 6000, 5000, 4000, 3500, 2500, 2000, 1500, 1200, 900, 800, 700, 600, 400, 300, 200, and 100 bp. Lanes **2 -7** are clones digested with Nde*I* and Hind*III* to confirm the ligation of *phnZHis* (593 bp) into pET21a (5378 bp).

### 3.2.1.2 Construction of pET21a_*StrepphnZHis*

The purity of PhnZ following a single step of affinity chromatography was not always in excess of 95% and occasionally required two passages through a Ni-NTA column. For this reason, a Strep tag was added to the N-terminus of *phnZHis* to create a more rapid two-step purification system. *StrepphnZHis* was amplified from the pJExpress401_*phnZ* plasmid using the For*StrepphnZ* and Rev*HisphnZ* primers and gradient PCR to determine the ideal annealing temperature (**Figure 3-10**). Six different annealing temperatures were tested and all resulted in approximately equal degrees of amplification.

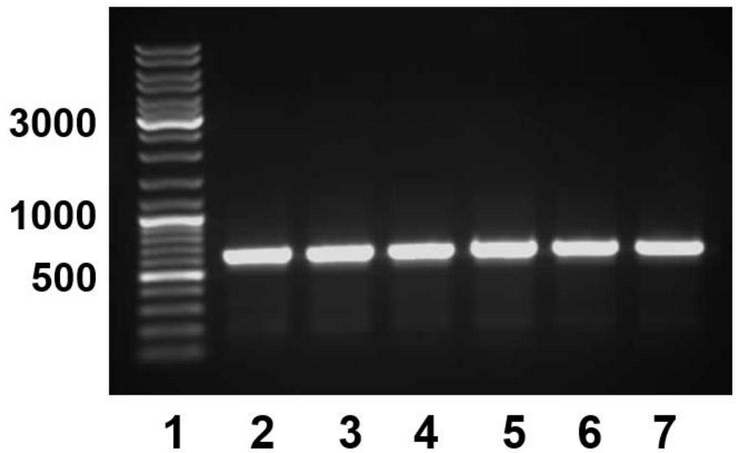


**Figure 3-10. 1% agarose gel of *StrepphnZHis* PCR products.** Lane **1** is the DNA ladder SM0333 (Fermentas) with the size of the brighter bands indicated to their left; the other fragments are: 10000, 8000, 6000, 5000, 4000, 3500, 2500, 2000, 1500, 1200, 900, 800, 700, 600, 400, 300, 200, and 100 bp. Lanes **2** – **7** are PCR products amplified using different annealing temperatures: (**2**) 52.0, (**3**) 53.7, (**4**) 56.1, (**5**)58.7, (**6**) 60.8, and (**7**) 61.9 °C. The expected size of *StrepphnZHis* is 638 bp.

The gel purified *StrepphnZHis* PCR product and pET21a were digested using *Nde*I and *Hind*III. Agarose gel electrophoresis of the digests confirmed the expected fragment lengths of 5378 bp and 638 bp, respectively (**Figure 3-11**, **A**). This gel was used to estimate DNA concentrations and the two fragments were ligated together using standard procedures. Ligation products were transformed into XL1-Blue *E. coli* cells and grown overnight. Three single colonies were obtained and all three were grown overnight in liquid culture to produce pDNA. Plasmid DNA was isolated and digested using *Nde*I and *Hind*III to confirm the ligation of *StrepphnZHis* into pET21a. Two clones were positive and one was negative (**Figure 3-11**, **B**).

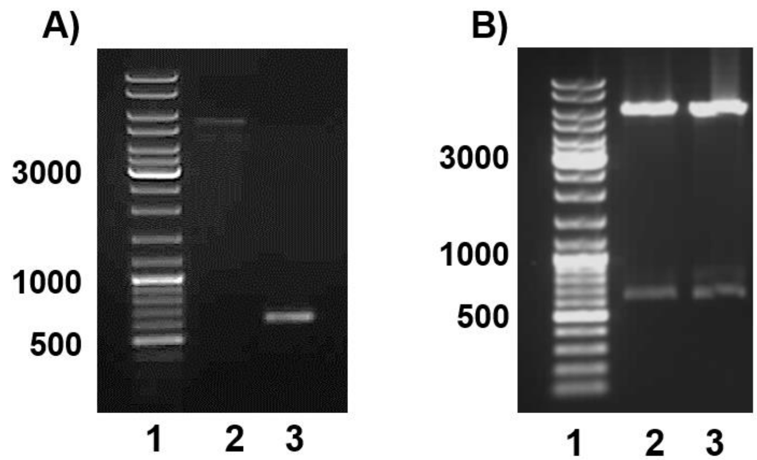


**Figure 3-11. 1% agarose gels of fragments used for ligation of pET21a and *StrepphnZHis* and analysis of restriction digested clones.** Lane **1** is the DNA ladder SM0333 (Fermentas) with the size of the brighter bands indicated to their left; the other fragments are: 10000, 8000, 6000, 5000, 4000, 3500, 2500, 2000, 1500, 1200, 900, 800, 700, 600, 400, 300, 200, and 100 bp. **A)** agarose gel of digested and gel-purified pET21a (**2**) and *StrepphnZHis* (**3**); **B)** positive clones digested with *Nde*I and *Hind*III to confirm the ligation of *StrepphnZHis* (638 bp) into pET21a (5378 bp).

### 3.2.1.3 Expression and purification of PhnZHis and StrepPhnZHis from pET21a

Production of PhnZ from pJExpress401_*phnZ*, pET21a_*phnZHis*, and pET21a_*StrepPhnZHis* was analyzed by SDS-PAGE to determine optimal expression conditions. All three constructs were expressed at both 30 and 37°C, 0.5 and 1 mM IPTG, and 240 rpm for 4 hours in an air shaker. The optimal conditions for each respective construct were the following: pJExpress401_*phnZ*, 30°C, 0.5 mM IPTG, 240 rpm, 4 hours; pET21a_*phnZHis*, 37°C, 0.5 mM IPTG, 240 rpm, 4 hours; pET21a_*StrepphnZHis*, 37°C, 0.5 mM IPTG, 240 rpm, 4 hours.  PhnZ production for each construct using the optimal expression conditions is shown in **Figure 3-12.**

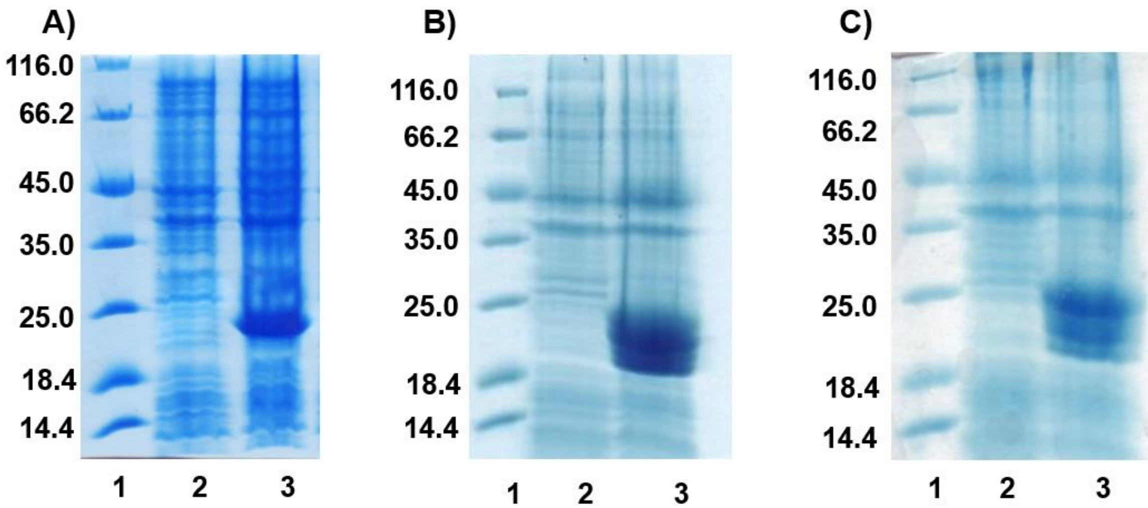


**Figure 3-12.  SDS-PAGE (12%) analysis of PhnZ production from different clones.** Lane **1** in all gels is the protein molecular weight ladder 26610 (Thermo Scientific), molecular weights indicated to the left of the bands in kDa, **A)** PhnZ production from pJExpress410_*phnZ*; **(2)** uninduced and (**3**) induced BL21 (DE3) / pJExpress410_*phnZ*. **B)** PhnZ production from pET21a_*phnZHis*; **(2)** uninduced and (**3**) induced BL21 (DE3) / pET21a_*phnZHis*.  **C)** PhnZ production from pET21a_*StrepphnZHis*; **(2)** uninduced and (**3**) induced BL21 (DE3) / pET21a_*StrepphnZHis*.    PhnZ appears as a band at 22.4 kDa in **A)** and **B)** and at 23.4 kDa in **C)**.

As mentioned previously, yields of 6-12 mg per litre of culture could be achieved using pJExpress401_*phnZ* and typical production levels from a half litre culture can be seen in **Figure 3-12, A**.  Production levels from the pET21a vector of both PhnZHis and StrepPhnZ were similar to production levels from the pJExpress401 vector (**Figure 3-12, B** and **C**), however the results were more consistent.  It should be noted that although the production levels of PhnZ from the pET21a vector appear to be greater in as seen in **Figure 3-12,** production levels are not in fact greater, rather PhnZ appears as multiple bands on the gel when insufficiently reduced prior to SDS-PAGE analysis and gives the illusion of greater protein production. Mass spectrometry has confirmed that a sample of PhnZ that appears as multiple bands is in fact intact protein. Purification of the cultures **A**, **B**, and **C** in **Figure 3-12** yielded 6 mg, 6 mg, and 9 mg per litre of culture, respectively.

PhnZHis expressed from pET21a_*phnZHis* was purified using a Ni-NTA gravity column and protein purity was determined using SDS-PAGE. Analysis of the wash fractions indicates that PhnZ co-elutes with higher molecular weight proteins (**Figure 3-13 A**, lanes **7-8**) that have a similar affinity for the Ni-NTA resin and do not wash off the column at lower concentrations of imidazole (**Figure 3-13 A**, lanes **5-6**). The multiple bands for PhnZ that are observed using SDS-PAGE analysis are the result of a lack of fresh DTT in the sample.

StrepPhnZHis expressed from pET21a_*StrepphnZHis* was purified using a Ni-NTA gravity column and the protein-containing fractions were pooled and concentrated to 1 mL prior to loading onto the Strep column for a second step of purification. SDS-PAGE analysis was used to determine protein purity. Analysis of the wash fraction after loading onto the Strep column shows several unspecific proteins that co-eluted with PhnZ from the Ni-NTA columns (**Figure 3-13 B**, lane **4**). Elution fractions of PhnZ indicate that PhnZ was isolated in greater purity than with a single purification step using a Ni-NTA column (**Figure 3-13 B**, lanes **5-8**).

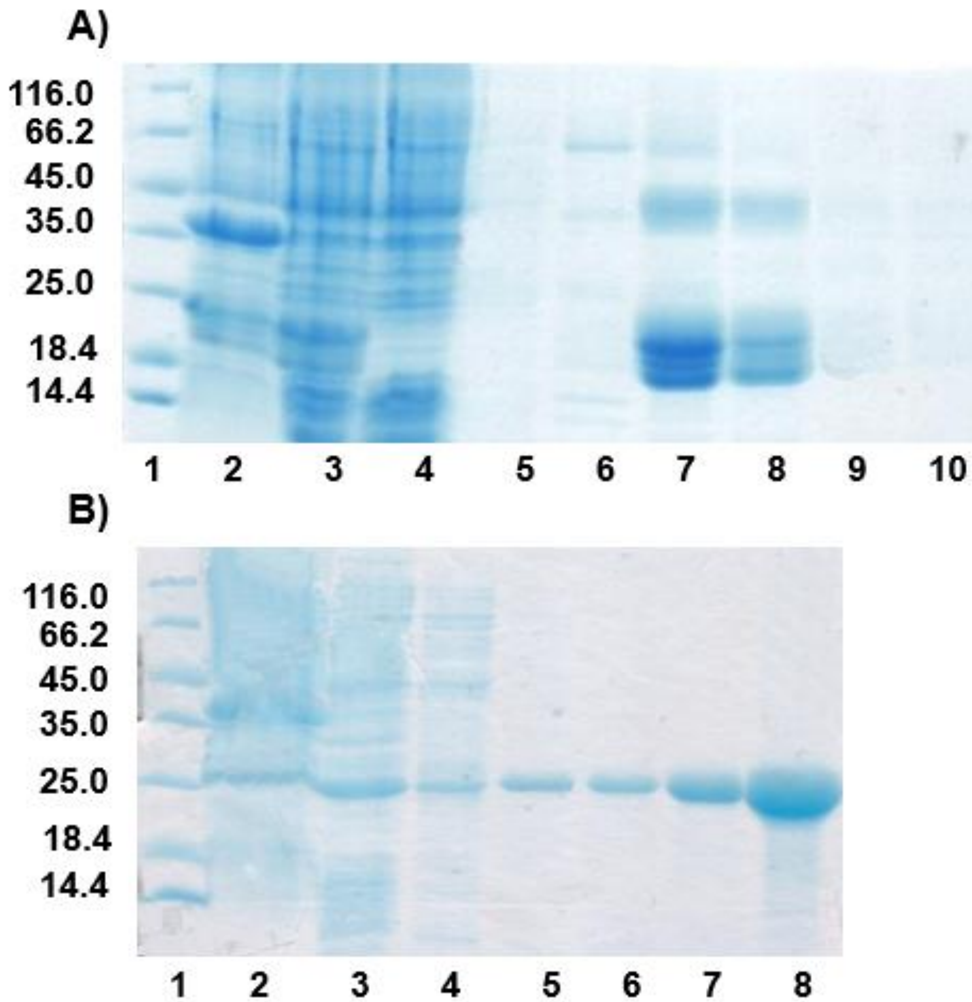


**Figure 3-13. SDS-PAGE (12%) analysis of PhnZ purification from pET21a_*phnZHis* and pET21a_*StrepphnZHis*.** Lane **1** in both gels is the protein molecular weight ladder 26610 (Thermo Scientific), molecular weights are indicated to the left of the bands in kDa. **A)** PhnZ purification from pET21a_*phnZHis*; **(2)** insoluble cell lysate, **(3)** cleared lysate, **(4)** flow-through upon washing the column with wash buffer, and **(5) – (10)** elution fractions. PhnZ appears as a band at 22.4 kDa. **B)** PhnZ purification from pET21a_*StrepphnZHis*; **(2)** insoluble cell lysate, **(3)** cleared lysate, **(4)** flow-through upon washing the Strep column with wash buffer, and **(5) – (8)** elution fractions. PhnZ appears as a band at 23.4 kDa.

### 3.2.1 Probing the role of the coupled interaction between Y24 and E27

To investigate the importance of the apparent coupled interaction between the active site residues Y24 and E27 during substrate recognition and binding, a double variant of PhnZ was generated to introduce the substitutions Y24F and E27A. The QuikChange protocol (Stratagene) was used to introduce these substitutions using PCR with mutagenic primers. PCR was performed using pJExpress401_*phnZY24F* (generated by Laura van Staalduinen using the same protocol[62]) as a template and using optimized procedures that were previously established.[66] Following PCR, the amplicon was treated with *Dpn*I to digest the parent DNA and the mutated PCR product was transformed into *E. coli* XL1-Blue. Six single colonies were selected and grown in liquid culture overnight for isolation of pDNA. The pDNA was digested using *Nde*I and *Hind*II (**Figure 3-14**) and of the six clones, only one had appeared to contain a DNA fragment that was the expected size of *SrepphnZY24F/E27A* (638 bp) (**Figure 3-14**, lane **2**). The plasmid DNA of this clone was sequenced to confirm the desired mutations.

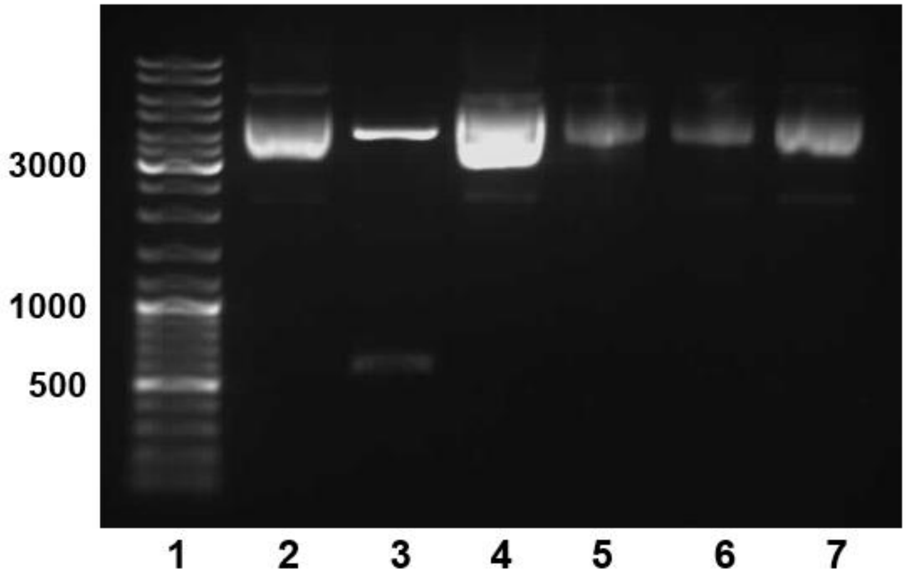


**Figure 3-14. 1% agarose gel of restriction-digested pDNA encoding PhnZ Y24F/E27A.** Lane **1** is the DNA ladder SM0333 (Fermentas) with the size of the brighter bands indicated to their left; the other fragments are: 10000, 8000, 6000, 5000, 4000, 3500, 2500, 2000, 1500, 1200, 900, 800, 700, 600, 400, 300, 200, and 100 bp. Lane **3** is the *Nde*I- and *Hind*III-digested pDNA from a clone that contained the desired *phnZY24F/E27A* gene. Lanes **2** and **4-7** are the *Nde*I- and *Hind*III-digests of pDNA from clones that did not contain the desired *phnZY24F/E27A* gene. Expected sizes of pET21a and StrepphnZY24F/E27AHis are 5378 bp and 638 bp, respectively.

### 3.2.1.1 Subcloning *phnZY24F/E27A* into pET21a

For ease of purification, *phnZY24F/E27A* was PCR amplified from pJExpress401_*phnZY24F/E27A* using the method described above for the construction of pET21a_*StrepphnZHis*. The *StrepphnZY24F/E27AHis* amplicon that was excised from the gel and the pET21a vector into which it would be ligated were digested using *Nde*I and *Hind*III. Agarose gel electrophoresis was used to analyze the digested fragments and bands corresponding to digested pET21a and *StrepphnZY24F/E27AHis* were visualized at the expected sizes of 5378 bp and 638 bp, respectively (**Figure 3-15**, **A**). This gel was used to estimate DNA concentrations and the two fragments were ligated together using standard procedures. Ligation products were transformed into XL1-Blue and grown overnight. Nine single colonies were obtained and all nine were grown overnight in liquid culture to produce pDNA. Plasmid DNA was isolated and digested using *Nde*I and *Hind*III to confirm the ligation of *StrepphnZY24F/E27AHis* into pET21a. Four of the nine clones were positive (**Figure 3-15**, **B**).

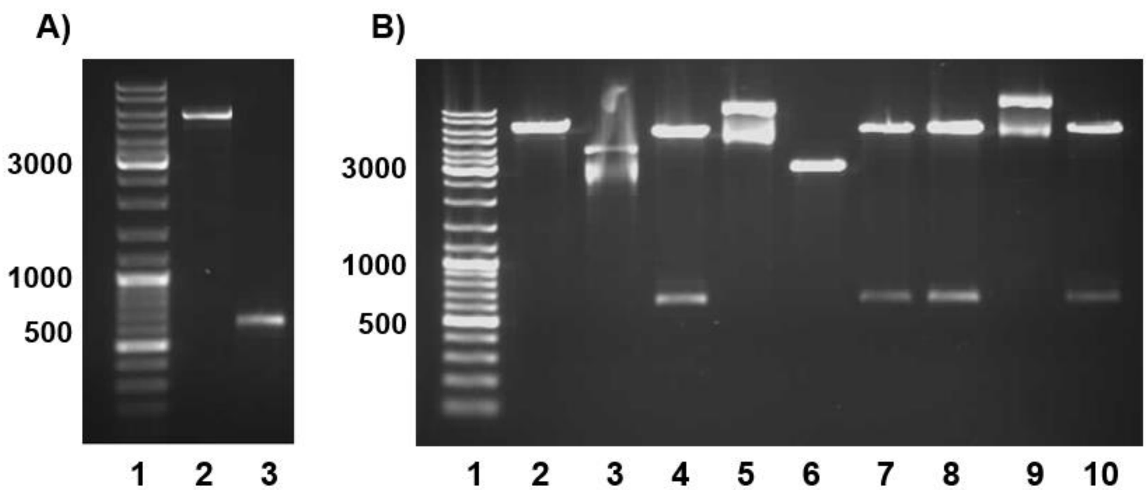


**Figure 3-15. 1% agarose gels of fragments used for ligation of pET21a and *StrepphnZHis* and analysis of digested clones.** Lane **1** is the DNA ladder SM0333 (Fermentas) with the size of the brighter bands indicated to their left; the other fragments are: 10000, 8000, 6000, 5000, 4000, 3500, 2500, 2000, 1500, 1200, 900, 800, 700, 600, 400, 300, 200, and 100 bp. **A)** agarose gel of digested and gel-purified pET21a (**2**) and *StrepphnZY24F/E27AHis* (**3**); **B)** positive clones (**4, 7, 8, 10**) digested with *Nde*I and *Hind*III to confirm the ligation of *StrepphnZY24F/E27AHis* (638 bp) into pET21a (5378 bp).

### 3.2.1.2 Analysis of PhnZ Y24F/E27A activity by $^{31}$P-NMR spectroscopy

To analyze the activity of PhnZ Y24F/E27A, this mutant was first expressed and purified using the same method as for StrepPhnZHis. PhnZ Y24F/E27A was then reacted with (*R*)-**13** in the presence of Fe(II) and analyzed using $^{31}$P-NMR spectroscopy. No change in intensity in the NMR signal (δ13.7 ppm for (*R*)-**13**) was observed between the enzyme-free control and the PhnZ reaction, and there was no appearance of a new signal at approximately δ 3 ppm which would indicate the generation of $P_i$ (**Appendix C, Figure A 45**).

It was suspected that the specificity of this mutant could have been altered by removing the dependence of the 2-amino group for activity. However, when PhnZ Y24F/E27A is reacted with (*R*)-**17** (δ19.3 ppm) in the presence of Fe(II), analysis by $^{31}$P-NMR spectroscopy does not indicate any conversion to $P_i$ (**Appendix C, Figures A 46 and 47**).

### 3.2.2 Absorbance spectra of PhnZ and active site variants

When concentrated in excess of 200 µM, solutions of WT PhnZ have a distinct purple colour (**Figure 3-17**, **A**) and the addition of substrate results in a colour change to yellow (**Figure 3-16**, **B**).

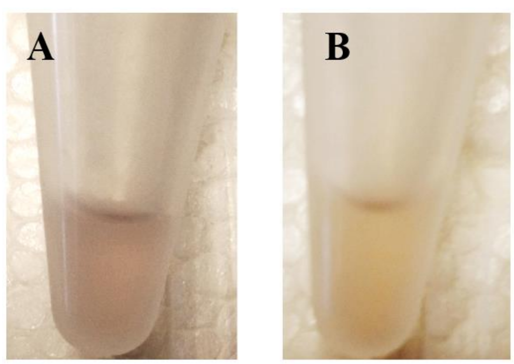


**Figure 3-16. Colour of concentrated WT PhnZ solutions. A)** A WT PhnZ solution without substrate bound is distinctly purple and **B)** a WT PhnZ solution with substrate bound is distinctly yellow.

This colour change occurs where there is a disruption in the charge transfer complex between Y24 and Fe1, and can also be observed using UV-Vis spectroscopy. Absorbance spectra of concentrated WT PhnZ solutions display a prominent shoulder at approximately 350 nm (**Figure 3-16, A**) and an absorbance maximum at approximately 510 nm. However, the addition of (*R*)-**13** results in a decrease in the absorbance at 510 nm. Likewise, absorbance spectra of PhnZ variants that would cause a disruption in the charge transfer complex also show decreased absorbance at 510 nm (**Figure 3-16, B**).

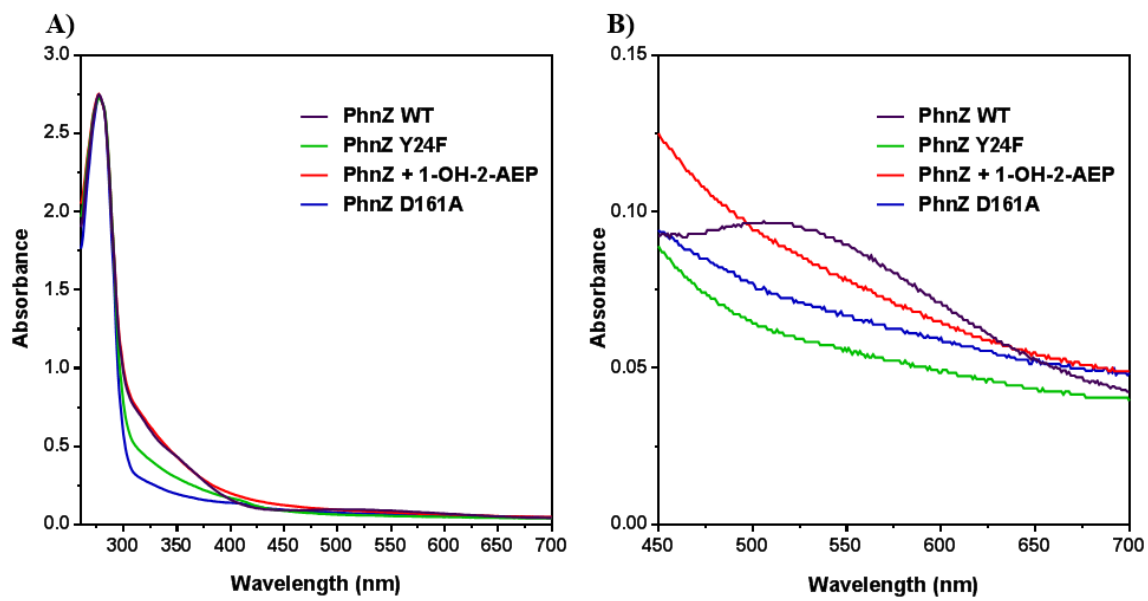


**Figure 3-17. PhnZ absorbance spectra. A)** Absorbance spectra of PhnZ WT (purple), PhnZ Y24F (green), PhnZ in the presence of 4 mM (*R*)-**13** (red), and PhnZ D161A (blue). **B)** Expansion of the PhnZ absorbance spectra in the region of 450-700 nm.

### 3.2.3 ICP-MS analysis of PhnZ and active site variants

ICP-MS was used to determine the amount of Fe that PhnZ and active site variants contain in the active site without the addition of excess Fe. The WT contained the largest amount of Fe, whereas E27A contained the least with 1.2 and 0.20 mol of Fe per mol PhnZ, respectively.  These values and those for other active site variants are presented in **Table 3-3**.

**Table 3-3. Fe content of PhnZ and active site variants.** Fe content represented as molar ratios as determined by ICP-MS. Values are derived from triplicate measurements.

| Variant | [Fe]/[PhnZ] |
|---|---|
| WT | 1.2 ± 0.1 |
| Y24F | 0.355 ± 0.006 |
| E27A | 0.204 ± 0.006 |
| H80A | 0.46 ± 0.01 |
| H58A | 1.12 ± 0.04 |
| D161A | 0.301 ± 0.007 |

### 3.2.4 Analysis of the substrate specificity of PhnZ by $^{31}$P-NMR spectroscopy

PhnZ was reacted with (*R*)**-13** in the presence of Fe(II) for several hours whereupon the reaction mixture was analyzed using $^{31}$P-NMR spectroscopy. The PhnZ substrate, (*R*)-**13**, exhibits a chemical shift at approximately δ 13.7 ppm (**Figure 3-18**, **A**) and when it is converted to $P_i$, there is a shift upfield to approximately δ 2.0 ppm (**Figure 3-18**, **B**).

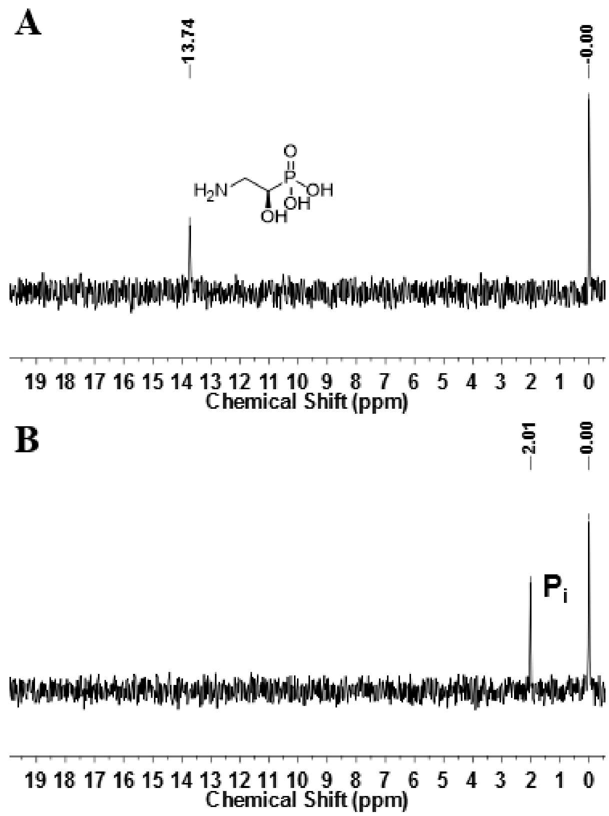


**Figure 3-18. $^{31}$P-NMR spectroscopic analysis of the PhnZ reaction. A)** Enzyme-free control, (*R*)-**13** at 13.7 ppm and **B)** PhnZ reaction, $P_i$ at 2.0 ppm. Reactions were carried out with 1 mM substrate and 5 µM PhnZ at pH 7.0. All signals are referenced to 85% $H_3PO_4$ at 0.0 ppm.

Several substrate analogues (**Figure 2.2, B**) were synthesized by members of the Hammerschmidt group (University of Vienna) to investigate the substrate specificity of PhnZ. These substrates were synthesized to investigate the effect of chain length (**14**, **15**, **16**) and methylation (**19**, **20**). Two other analogues (**8**, **18**) were also tested to probe the effect of heteroatom substituents on the alpha carbon. All reactions were set up and terminated in the same way as the reactions with (*R*)-**13** and were analyzed by $^{31}$P-NMR spectroscopy. In all cases an enzyme-free control as well as a reaction with PhnZ was conducted. PhnZ was able to completely convert (1*R*, 2*R*)-**14** and (*R*)-**16** to $P_i$, and 50% of (+/-)-**19** (**Table 3-4**). All spectra are presented in **Appendix B**.

**Table 3-4. [31]P-NMR chemical shifts of EF-controls and PhnZ reactions with substrate analogues.** All signals referenced to 85% $H_3PO_4$ at 0.0 ppm.

| Structure | Stereochemistry | Chemical shift (ppm) EF-control | Chemical shift (ppm) PhnZ reaction | Reaction |
|---|---|---|---|---|
| 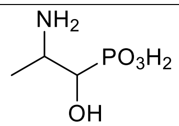 | (1R,2R) | 14.59 | 1.95 | yes |
| | (1*R*,2*R*):(1*S*,2*S*) | 14.59 | 14.59; 2.07 | 50% |
| **14** | (1*R*,2*S*):(1*S*,2*R*) | 13.81 | 13.88; 2.00 | 50% |
| 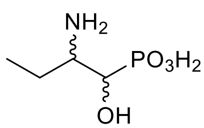 **15** | (+/-) | 15.19 | 15.19 | No |
| 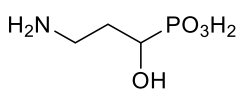 | (+/-) | 16.44 | 16.44; 2.00 | 50% |
| | (*S*) | 16.35 | 16.44 | No |
| **16** | (*R*) | 16.25 | 2.19 | Yes |
| 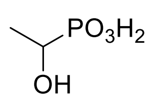 **17** | (*R*) | 20.22 | 20.77 | No |
| 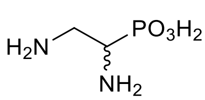 **18** | (+/-) | 12.76 | 12.81 | No |
| 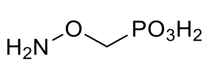 **8** | n/a | 11.8 | 11.85 | No |
| 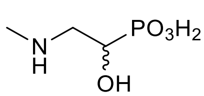 **19** | (+/-) | 13.37 | 13.38; 2.23 | 50% |

| | | | | |
|---|---|---|---|---|
| 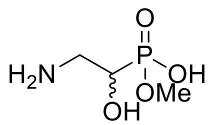 **20** | (+/-) | 17.78 | 17.79 | No |

### 3.2.5 pH profile of PhnZ reactivity

The malachite green assay was used to determine the pH optimum of PhnZ with (*R*)-**13** by determining the amount of $P_i$ generated within 5 minutes. Four different buffers were used to cover a range of pH 5.0-8.5 with half pH unit increments. Overlapping pH values were used to detect buffer effects on enzyme activity. The amount of $P_i$ that was generated was determined by producing a $P_i$ standard curve using each buffer (**Figure 3-19**) and using the equation of the line (**Table 3-5**) to relate the absorbance of the PhnZ reactions to the amount of $P_i$ that was generated. A pH profile for PhnZ was then produced by plotting the amount of $P_i$ that was generated against the respective pH (**Figure 3-20**).

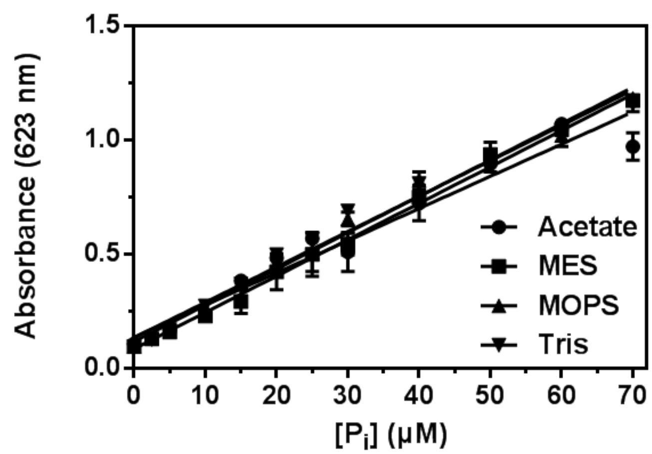


**Figure 3-19. $P_i$ standard curves for the buffers used to generate the pH profile of PhnZ.** All data points performed in duplicate.

**Table 3-5. Equations of the $P_i$ standard curves for the buffers used to generate the pH profile of PhnZ.**

| Buffer | Equation |
|---|---|
| Acetate | $Abs_{623} = [P_i]\cdot 0.014 + 0.137$ |
| MES | $Abs_{623} = [P_i]\cdot 0.016 + 0.086$ |
| MOPS | $Abs_{623} = [P_i]\cdot 0.016 + 0.118$ |
| Tris | $Abs_{623} = [P_i]\cdot 0.016 + 0.135$ |

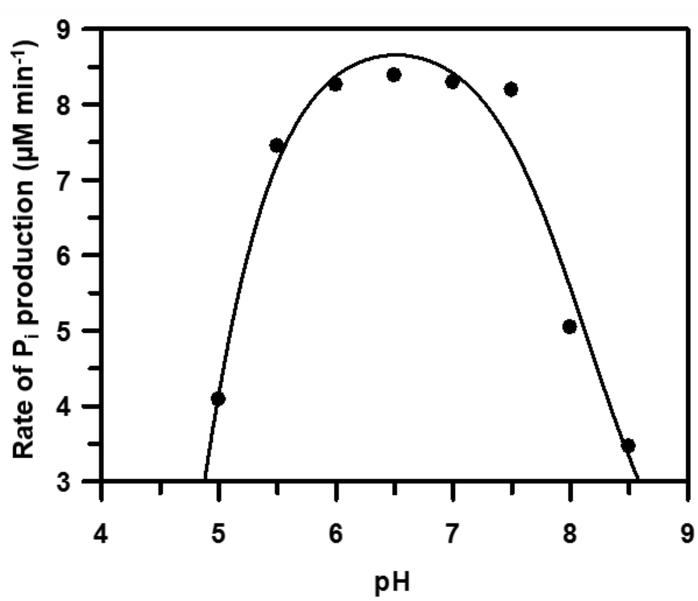


**Figure 3-20. pH profile of PhnZ.** All data points were generated from a single trial.

**Table 3-6. Apparent p$K_a$ values determined from the pH profile of PhnZ.**

| Apparent p$K_a$ | Value ± error |
|---|---|
| p$K_a$ 1 | 4.4 ± 0.4 |
| p$K_a$ 2 | 8.1 ± 0.3 |

### 3.2.6 Kinetic analysis of PhnZ with (*R*)-13 and (1*R*,2*R*)-14

Kinetic analysis of PhnZ was conducted by determining the initial rate of C-P bond cleavage by PhnZ using the EnzChek phosphate by monitoring the reaction at 360 nm over 30 minutes. The pH of the buffer provided with the kit is 8.0, however this buffer was replaced by MOPS at pH 7.0 to account for the pH optimum of PhnZ (**section 3.2.6**) To ensure that the reaction rate was not limited by the coupling enzyme, PNP, at this pH, the concentration of PhnZ was doubled to determine the effect this would have on the initial rate. The rate doubled when the concentration of PhnZ doubled, therefore PNP was not found to be rate-limiting. The molar extinction coefficient at 360 nm and pH 8.0 for the 2-amino-6-mercapto-7-methylpurine product is 11 200 $M^{-1}$ $cm^{-1}$, however the extinction coefficient at pH 7.0 was unknown and had to be determined. The difference in absorbance at 360 nm between a blank and reactions of PNP with four concentrations of $P_i$ were plotted against the concentrations of $P_i$ that were used (**Figure 3-21**) and the slope of the plot was used to determine an extinction coefficient of 7021 $M^{-1}$ $cm^{-1}$ at pH 7.0.

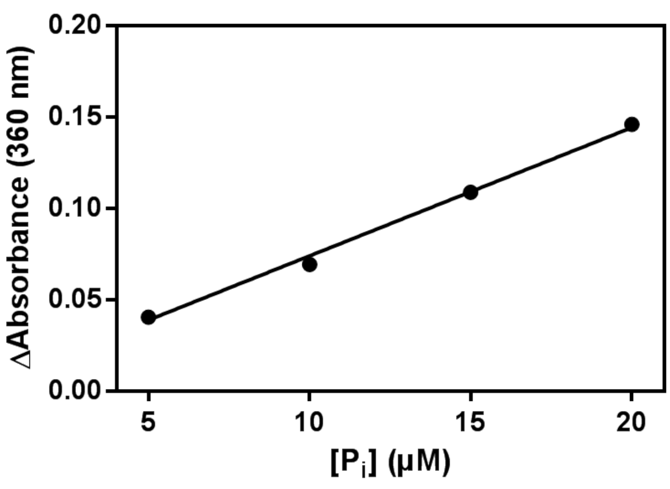


**Figure 3-21. Plot of ΔAbsorbance (360 nm) vs [$P_i$] (μM) generated using the EnzChek phosphate assay and $P_i$ standards.** Data points were generated using single trials.

Kinetic analysis was first carried out for PhnZ with (*R*)-**13** for later comparison with the other substrates that it can accept. Kinetic analysis was carried out on both PhnZHis and StrepPhnZHis in the interest of determining if either one could be used for kinetic analysis. The EnzChek phosphate assay was used to determine the initial rate of C-P bond cleavage at various concentrations of (*R*)-**13** and the data was fitted to the Michaelis-Menten equation (**Figure 3-22**). Kinetic parameters for each plot are presented in **Table 3-7**.

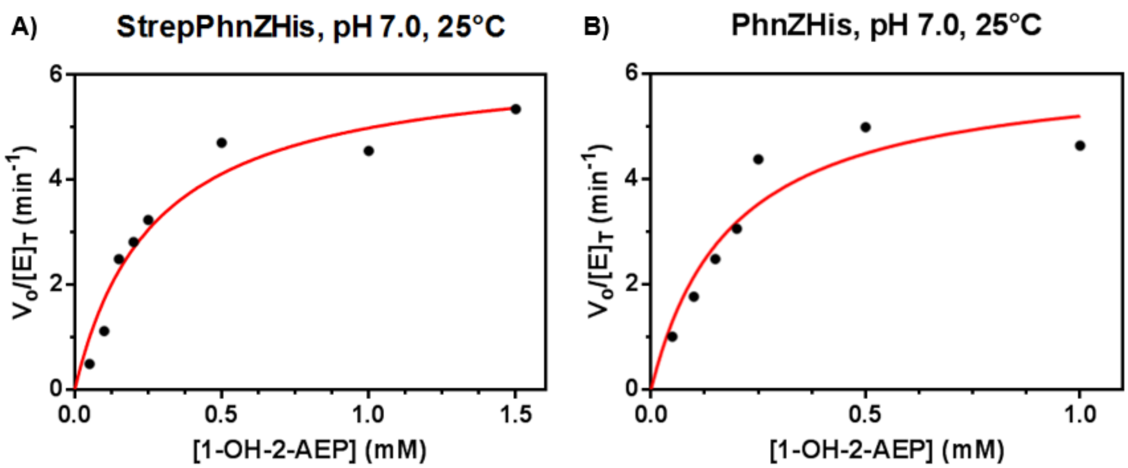


**Figure 3-22. Michaelis-Menten plots for the reaction of PhnZ with (*R*)-13 (1-OH-2-AEP).** Comparison of the plot generated using **A)** StrepPhnZHis and **B)** PhnZHis. All data points were generated using single trials.

**Table 3-7. Kinetic parameters for the reaction of PhnZ with (*R*)-13 and (1*R*,2*R*)-14.**

| Kinetic parameter | (*R*)-13 (StrepPhnZHis) | (*R*)-13 (PhnZHis) | (1*R*,2*R*)-14 (StrepPhnZHis) |
|---|---|---|---|
| $k_{cat}$ ($min^{-1}$) | 6.3 ± 0.6 | 6.2 ± 0.9 | 4.6 ± 0.2 |
| $K_M$ (mM) | 0.27 ± 0.07 | 0.19 ± 0.07 | 0.20 ± 0.02 |
| $k_{cat}/K_M$ ($min^{-1}$ $mM^{-1}$) | 23.5 ± 6.35 | 32.9 ± 12.8 | 22.8 ± 7.7 |

A Michaelis-Menten plot was also generated for the reaction of PhnZ with the substrate analogue (1*R*,2*R*)-**14** (**Figure 3-23**). A comparison of the kinetic parameters to those of the reaction of PhnZ with (*R*)-**13** is presented in **Table 3-7**.

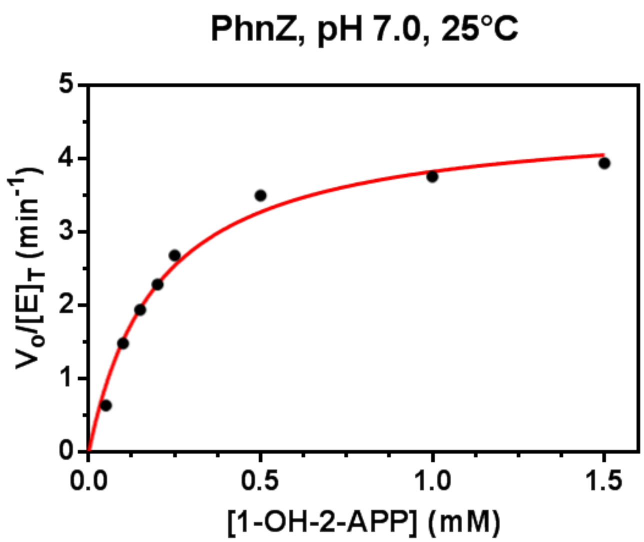


**Figure 3-23. Michaelis-Menten plot for the reaction of PhnZ with (1*R*,2*R*)-14 (1-OH-2-APP).** All data points were generated using single trials.

PhnZ has also been found to convert (*R*)-**16** to $P_i$, however the reaction was determined to be too slow for detection using the EnzChek phosphate assay. The malachite green assay was therefore used to determine kinetic parameters, however assay optimization is underway.

### 3.2.7 Kinetic isotope effect on hydrogen abstraction by PhnZ

The kinetic isotope effect (KIE) on hydrogen abstraction by PhnZ was determined by producing Michaelis-Menten plots for PhnZ with the substrates (*R*)-**13** and 1-D-(*R*)-**13**. The initial rate of C-P bond cleavage by PhnZ at various concentrations of (*R*)-**13** and 1-D-(*R*)-**13** was monitored using the EnzChek phosphate and at 360 nm over 10 minutes. Initial rates were plotted against the respective substrates and the data was fitted with the

Michaelis-Menten equation (**Figure 3-24**). The resulting kinetic parameters are in **Table 3-8** and the D-KIE calculated on those parameters are presented in **Table 3-9**.

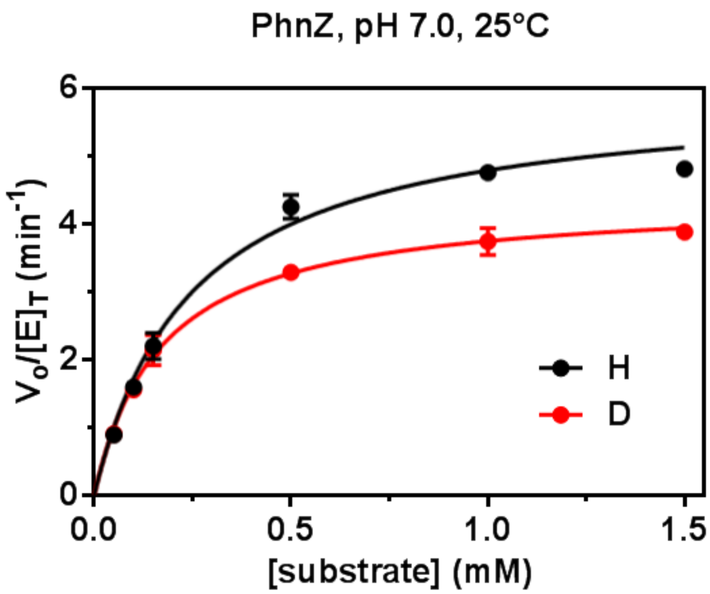


**Figure 3-24. Michaelis-Menten plots examining the KIE on hydrogen abstraction by PhnZ.** All data points were repeated triplicate with the exception of the data points at 0.1 and 1.5 mM substrate which were conducted as a single trial.

**Table 3-8. Kinetic parameters for the KIE on hydrogen abstraction by PhnZ.**

| Kinetic parameter | Mean ± error |
|---|---|
| $k_{cat(H)}$, min$^{-1}$ | 5.9 ± 0.2 |
| $K_{M(H)}$, mM | 0.25 ± 0.02 |
| $(k_{cat}/K_M)_{(H)}$, mM$^{-1}$min$^{-1}$ | 23.9 ± 2.5 |
| $k_{cat(D)}$, min$^{-1}$ | 4.4 ± 0.1 |
| $K_{M(D)}$, mM | 0.17 ± 0.01 |
| $(k_{cat}/K_M)_{(D)}$, mM$^{-1}$min$^{-1}$ | 25.9 ± 2.3 |

**Table 3-9. D-KIE on kinetic parameters for hydrogen abstraction by PhnZ.**

| D-KIE | Mean ± error |
|---|---|
| $k_{cat}$ | 1.36 ± 0.06 |
| $K_M$ | 1.5 ± 0.2 |
| $k_{cat}/K_M$ | 0.9 ± 0.1 |

### 3.2.8 Crystallization and X-ray data collection of PhnZ with substrate analogues

In order to investigate the nature of substrate binding within the PhnZ active site, PhnZ was co-crystallized with three substrate analogues: (*R*)-**17**, (1*R*, 2*R*)-**14**, and (*R*)-**16**. The crystallization conditions used for PhnZ with (±)-**13** (bis-tris pH 6.5, PEG 5000 MME) were used as a starting point to obtain crystals of PhnZ with the desired substrate analogues.

Initial attempts to co-crystallize PhnZ with (*R*)-**17** using an expansion of the conditions used for the co-crystallization of PhnZ with (*R*)-**13** failed to yield crystals and therefore a commercial screen was set up to screen for crystals with various conditions. This screen yielded small rod-like crystals and an expansion of that condition resulted in the formation of a cluster of rod-like crystals that were yellow in colour (**Figure 3-25, A**).

Initial attempts to crystallize PhnZ with (1*R*,2*R*)-**14** using an expansion of the conditions used for the co-crystallization of PhnZ with (*R*)-**13** were successful and yellow rod-like crystals were obtained. (**Figure 3-25, B**).

Initial attempts to crystallize PhnZ with (*R*)-**16** using an expansion of the conditions used for the co-crystallization of PhnZ with (*R*)-**13** were successful small clusters of yellow crystals were obtained (**Figure 3-25, C**). However, these crystals diffracted poorly and an additive screen was used to optimize crystallization conditions. Using this screen, yellow rod-like crystals were obtained with the addition of spermidine (**Figure 3-25, D**).

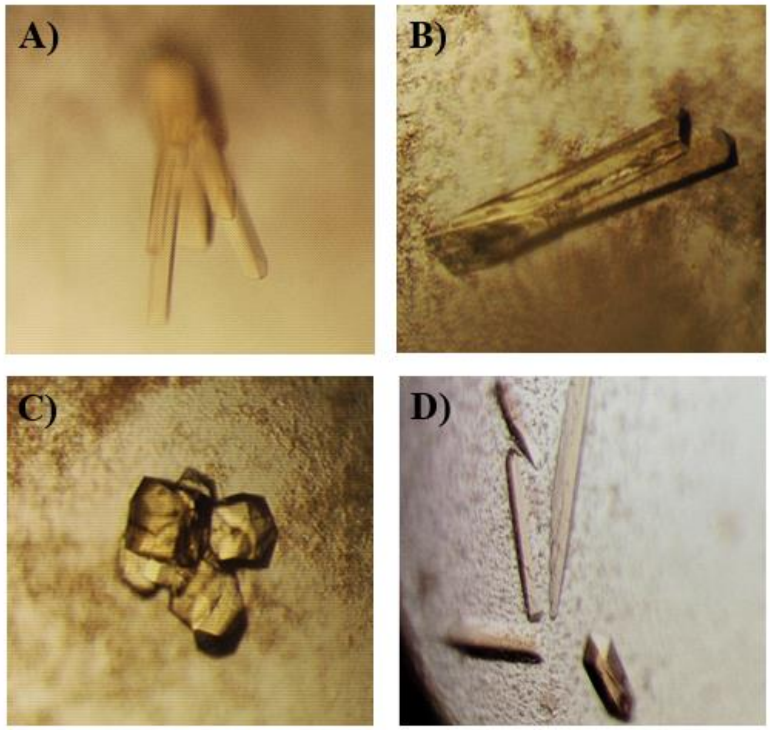


**Figure 3-25. Crystals of PhnZ co-crystalized with substrate analogues. A)** PhnZ co-crystallized with (*R*)-**17**, **B)** PhnZ co-crystallized with (1*R*, 2*R*)-**14**, **C)** PhnZ co-crystallized with (*R*)-**16** prior to optimization, and **D)** PhnZ co-crystallized with (*R*)-**16** after optimization. All crystals were yellow in colour.

#### 3.2.8.1 Structure solution

The crystal structures of PhnZ bound to (*R*)-**17**, (1*R*, 2*R*)-**14** and (*R*)-**16** were solved by molecular replacement using the substrate-bound PhnZ structure (PDB ID: 4MLN) as a search model. The structures of PhnZ co-crystallized with (*R*)-**17**, (1*R*, 2*R*)-**14** and (*R*)-**16** were solved to 1.7, 1.9, and 1.9 Å, respectively, and all crystals belonged to the $P2_12_12_1$ space group with 2 molecules of PhnZ in the asymmetric unit. Electron density for two metal ions in the active site of all molecules was seen and modelled as Fe.

**Table 3-10. Data collection and refinement statistics for the structures of PhnZ co-crystallized with substrate analogues.**

| | PhnZ : (*R*)-**17** | PhnZ : (1*R*, 2*R*)-**14** | PhnZ : (*R*)-**16** |
|---|---|---|---|
| **Data collection** | | | |
| Space group | $P2_12_12_1$ | $P2_12_12_1$ | $P2_12_12_1$ |
| Cell dimensions | | | |
| *a*, *b*, *c* (Å) | 68.00, 75.20, 83.20 | 68.48, 75.36, 83.67 | 68.48, 75.52, 82.20 |
| Wavelength | | | |
| Resolution (Å) | 19.90 – 1.70 | 19.69 – 1.90 | 19.96 - 1.90 |
| $R_{merge}$ | 7.0 (106.7) | 6.3 (77.4) | 8.2 (85.9) |
| $I/\sigma I$ | 16.04 (1.67) | 16.83 (2.52) | 17.98 (3.39) |
| Completeness (%) | 92.1 (64.0) | 99.9 (100.0) | 99.9 (99.9) |
| Redundancy | 6.6 | 7.2 | 10.7 |
| **Refinement** | | | |
| Resolution (Å) | 1.7 | 1.9 | 1.9 |
| No. reflections | 43829 | 34752 | 34205 |
| $R_{work} / R_{free}$ | 18.0/21.5 | 20.5/22.4 | 18.6/21.7 |
| No. atoms | | | |
| Protein | 2895 | 2844 | 2885 |
| Ligand/ion | 14/4 | 18/4 | 18/4 |
| Water | 296 | 212 | 251 |
| *B*-factors | | | |
| Protein | 29.4 | 37.1 | 36.7 |
| Ligand/ion | 22.1/26.1 | 30.1/68.9 | 36.4/27.5 |
| Water | 40.5 | 45.3 | 42.7 |
| R.m.s. deviations | | | |
| Bond lengths (Å) | 0.007 | 0.007 | 0.007 |
| Bond angles (°) | 1.090 | 1.055 | 1.013 |

Values in parenthesis represent the highest resolution shell.

### 3.2.8.2 Structure of PhnZ co-crystallized with (*R*)-17

The two molecules of PhnZ co-crystallized with (*R*)-**17** align well with an r.m.s.d. of 0.8 (**Figure 3-26, A**). Examination of the active site shows that the D21-N30 loop is found in a different conformation in each molecule (**Figure 3-26, B**), much like it is in the

PhnZ : (*R*)-**13** complex. In fact, molecule A in both complexes align well with and r.m.s.d. of 0.4 Å (**Figure 3-26, C**) and molecule B in both molecules align well with an r.m.s.d. of 0.4 Å (**Figure 3-26, E**). Examining the active site of a superimposition of molecule A from both molecules reveals that the active sites are nearly identical (**Figure 3-26, D**) with almost perfect overlap of both substrates and the D21-N30 loop, the key active site residues Y24 and E27. When examining the active site of a superimposition of molecule B from both molecules, the active sites are almost identical (**Figure 3-26, F**), however the D21-N30 loop appears to adopt a slightly different conformation and Y24 is more removed from the active site and is no longer a ligand for Fe1 with a distance of 4.7 Å from Fe1 compared to 2.1 Å in the PhnZ : (*R*)-**13** complex. E27 could not be modelled in molecule B in either complex.

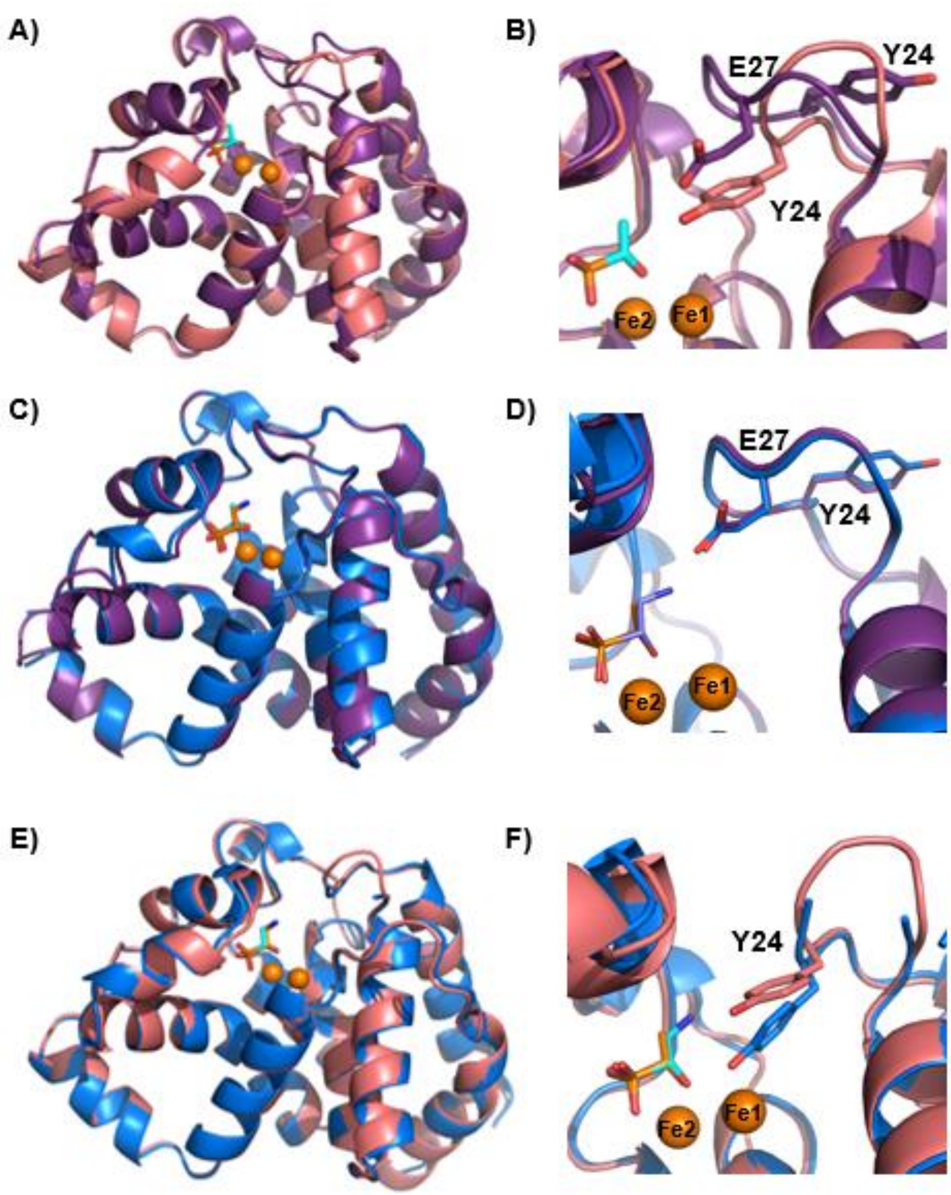


**Figure 3-26. Structure superimpositions of PhnZ co-crystallized with (*R*)-17.** Superimposition of molecules A (purple) and B (pink) from the PhnZ : (*R*)-**17** complex; **A)** overall superimposition of both molecules, **B)** view of the active site. Superimposition of molecule A from both the PhnZ : (*R*)-**17** complex (purple) and the PhnZ : (*R*)-**13** complex (blue); **C)** overall superimposition of both molecules, **D)** view of the active site. Superimposition of molecule B from both the PhnZ : (*R*)-**17** complex (pink) and the PhnZ : (*R*)-**13** complex (blue); **E)** overall superimposition of both molecules, **F)** view of the active site. (*R*)-**17** is modelled as light blue sticks, (*R*)-**13** is modelled as orange sticks, and Fe ions are modelled as orange spheres.

### 3.2.8.3 Structure of PhnZ co-crystallized with (1*R*, 2*R*)-**14**

As of the time of writing this thesis, preliminary crystallographic data of the PhnZ : (1*R*, 2*R*)-**14** complex includes a solved structure for only one molecule of the two observed in the asymmetric unit. This molecule aligns very well with molecule A from the PhnZ : (*R*)-**13** with an r.m.s.d. of 0.3 Å (**Figure 3-27, A**). Examining the active site, both are almost identical with the D21-N30 loop adopting an almost identical conformation and the Y24 and E27 residues aligning almost perfectly. (1*R*, 2*R*)-**14** binds to Fe2 in a manner almost identical to the binding (*R*)-**13**, with the methyl group on C2 pointing upwards in the active site (**Figure 3-27, B**).

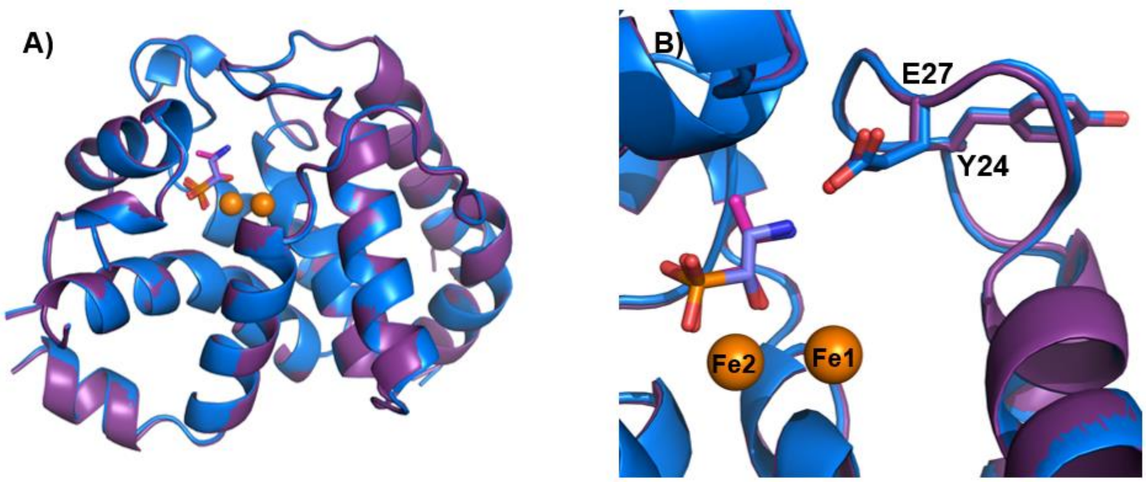


**Figure 3-27. Structure superimpositions of PhnZ co-crystallized with (1*R*, 2*R*)-14 (purple) and PhnZ co-crystallized with** (*R*)-**13 (blue). A)** View of the overall architecture of molecule A of both complexes. **B)** View of active site. (1*R*, 2*R*)-**14** is modelled as pink sticks, (*R*)-**13** is modelled as light blue sticks, and Fe ions are modelled as orange spheres.

### 3.2.8.4 Structure of PhnZ co-crystallized with (*R*)-16

The two molecules of PhnZ co-crystallized with (*R*)-**16** align very well with each other with an r.m.s.d. of 0.6 and there appears to be only one conformation of the D21-N30 loop. The conformation of the loop in this complex is very different from what has been seen with the other PhnZ complexes. Superimposing molecule B from the PhnZ : (*R*)-**16** complex with molecule A from the PhnZ : (*R*)-**13** complex, the two molecules align well with an r.m.s.d. of 0.6 Å (**Figure 3-28, A**). Examination of the active site shows that the backbone of the D21-N30 loop is found in very similar conformations in both molecules. However the side chains project differently from the loop, and in the case of the PhnZ : (*R*)-**16** complex, both Y24 and E27 project towards the active site (**Figure 3-28, C**). E27 is largely in the same position within the active site. However, due to the greater chain length of (*R*)-**16**, the carbonyl carbon of carboxyl group of E27 is displaced further out of the active site (3.2 Å) in comparison to the PhnZ : (*R*)-**13** complex (1.3 Å). Superimposing molecule B from the PhnZ : (*R*)-**16** complex with molecule B from the PhnZ : (*R*)-**13** complex, the two molecules align well with an r.m.s.d. of 0.8 Å (**Figure 3-28, B**). Examining the active site, Y24 overlaps almost perfectly between both molecules, although the loop conformations are very different. Likewise, although E27 cannot be modelled in the PhnZ : (*R*)-**13** complex, it is unlikely based on the loop conformation that it would be projecting towards the 2-amino group of the substrate (**Figure 3-28, D**).

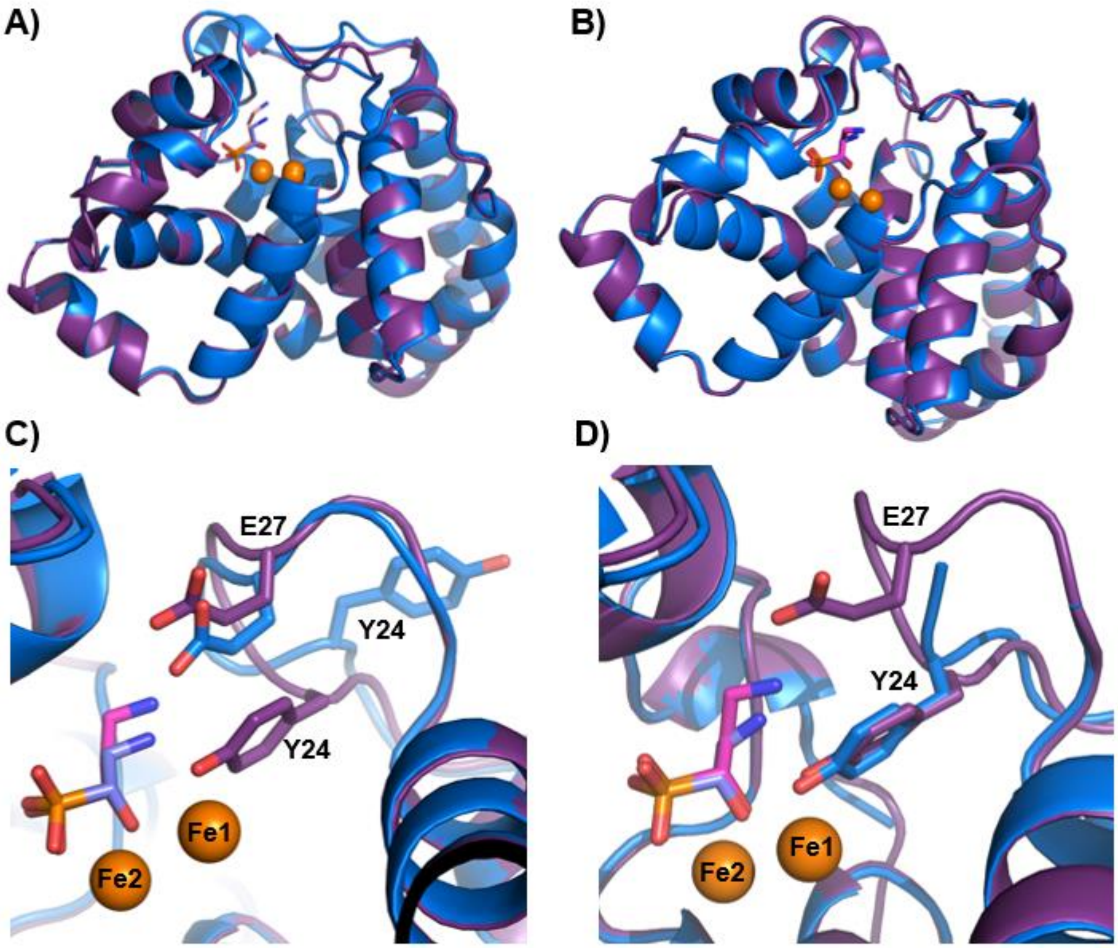


**Figure 3-28. Structure superimpositions of PhnZ co-crystallized with (*R*)-16 (purple) and PhnZ co-crystallized with (*R*)-13 (blue).** Superimposition of molecules B and A from the PhnZ : (*R*)-**16** complex (purple) and PhnZ : (*R*)-**13** complex (blue), respectively; **A)** overall superimposition of both molecules, **C)** view of the active site. Superimposition of molecule B from both the PhnZ : (*R*)-**16** complex (purple) and the PhnZ : (*R*)-**13** complex (blue); **B)** overall superimposition of both molecules, **D)** view of the active site. (*R*)-**16** is modelled as pink sticks, (*R*)-**13** is modelled as light blue sticks, and Fe ions are modelled as orange spheres.

# Chapter 4

# Discussion

## 4.1 The α-ketoglutarate/Fe(II)-dependent dioxygenase

A mechanism for PhnY has been proposed[66] based on the mechanism for TauD.[65] However, the active site residues necessary for catalysis have not been determined since a crystal structure of PhnY has not yet been obtained. Moreover, the residues used for substrate binding in TauD are not conserved with PhnY, despite the fact that these enzymes act on similar substrates (taurine and 2-aminoethylphosphonate, respectively). In the past, a major hurdle for obtaining a sample suitable for crystallography of PhnY was the inability to produce a sample that was stable enough to achieve high enough protein concentrations suitable for crystallography. In this work, improvements have been made to the expression and purification procedures for PhnY which now allows the enzyme to be isolated in high yields with improved stability. Many conditions have been tested to obtain crystals of PhnY, but a number of new obstacles now exist. PhnY is very unstable at room temperature, and although crystallization conditions at decreased temperatures have been tested in an attempt to slow the rate of precipitation, none of these have been successful. Various complexes were attempted, including apo-PhnY, PhnY with **2** or **10,** and PhnY with Fe(II), **2** or **10**. It was initially believed that PhnY may not have been crystallizing because it was reacting with the native substrate **2,** therefore the substrate analogue **10**, which is fluorinated at C1 preventing hydroxylation by PhnY, was also used to set up crystallization trays, however this was also unsuccessful. Moreover, all attempts to incubate a concentrated sample of PhnY with α-ketoglutarate were also unsuccessful, due to rapid precipitation regardless of the presence or absence of Fe(II), **2**, or **10** in any order of addition. This is, however, consistent with the observation that small amounts of PhnY precipitate at the end of reactions. In summary, the stability of PhnY remains a hurdle in obtaining crystals. Although it remains stable for a short time, it no longer remains stable under various crystallization conditions causing it to precipitate much too rapidly for well-ordered packing to occur and produce a crystal. Attempting to crystallize PhnY with other tags may alter crystal packing, and plasmids encoding PhnY with a C-terminal Strep tag and an N-terminal His tag have already been constructed and could be tested under various crystallization conditions. Although a high degree of purity (>95%) for PhnY has been achieved and is used in crystallography, a second purification step may help, as has been seen with PhnZ which has only produced crystals following purification by SEC after an initial purification by affinity chromatography.

Kinetic analysis enabled the determination of the kinetic parameters for PhnY which were 3.8 $min^{-1}$ and 0.4 mM for $k_{cat}$ and $K_M$, respectively. These values are within the same order of magnitude as those for PhnZ (6.2 $min^{-1}$ and 0.2 mM for $k_{cat}$ and $K_M$, respectively), which is to be expected if both enzymes work together within a pathway to degrade **2**. The low turnover values of PhnY and PhnZ may reflect the slow growth rate of the marine bacterium that produces these enzymes, which likely exists in a deep ocean environment where temperatures are low and $P_i$ levels approach nanomolar levels.[58]

The substrate specificity of PhnY was also investigated with 11 different phosphonates (**Figure 2-1**, **A**). However, unlike PhnZ, PhnY was only able to convert its natural substrate **2**. It is difficult to speculate which features of **2** are necessary for catalysis without crystallographic data to indicate which interactions between the substrate and active site residues are important. Nevertheless, using sequence alignments with PhnY homologues it will be possible to identify conserved residues that might be relevant to catalysis. These residues can be probed for their contribution to catalysis or substrate specificity through site directed mutagenesis. This could be complemented by modeling the structure of PhnY with a close homolog for which a structure is known. Finally, it would be useful to characterize homologues of PhnY that can be observed encoded in the genomes of a number of sequenced microorganisms.[61] These homologues may have different substrate specificities and be more amendable to structural characterization.

## 4.2 The C-P bond cleaving di-iron-dependent oxygenase PhnZ

### 4.2.1 Mechanism of PhnZ

The previously proposed mechanism for C-P bond cleavage by PhnZ[59] was based on the mechanism for MIOX[67]. Crystallographic and kinetic analysis now allows us to propose a more complete mechanism (**Figure 4-1**). The reaction begins with induced fit binding of the substrate, which is triggered by recognition of the 2-amino group of the substrate by E27 and expels Y24 from the oxygen binding site. This is believed to be accompanied by ionization of the α-hydroxyl of the substrate that binds to Fe2 and H62. The latter side chain appears to be important for catalysis, possibly as a general base, as indicated by a pronounced decrease in $k_{cat}$ from 11 $min^{-1}$ to 2 $min^{-1}$ when H62 is substituted for alanine. MIOX also has an active site residue for this purpose, however it is instead a lysine.[79] The Lewis acidity of Fe2 in a ferric oxidation state would encourage ionization of the substrate α-hydroxyl. The hypothesis that substrate recognition by E27 and binding to Fe2 causes Y24 to be expelled from its coordination site at Fe1 is supported by analyzing absorbance spectra of concentrated solutions of PhnZ. In the absence of substrate, the absorbance spectra of concentrated WT PhnZ solutions have a prominent shoulder at 350 nm and an absorbance maximum at 510 nm, which is characteristic of a charge-transfer complex between tyrosine and iron in the ferric state.[80] This characteristic absorbance maximum and the fact that tyrosine has a greater affinity for iron in the ferric oxidation state rather than ferrous, suggests that Fe1 is initially in the ferric oxidation state while Y24 is bound. Absorbance spectra of concentrated WT PhnZ solutions pre-incubated with substrate have a decreased absorbance at 510 nm suggesting Y24 is no longer bound, which is consistent with substrate binding causing a disruption in the charge-transfer complex between Fe1 and Y24. This is proposed to occur through an electron transfer from Fe2 (initially in the ferrous state) to Fe1 and expelling Y24 from its coordination site at Fe1 due to its decreased affinity for the ferrous oxidation state. A mixed oxidation state is also supported by Mössbauer and EPR spectroscopic analysis, however they cannot confirm the oxidation state of either iron at the beginning of the catalytic cycle.[61] Substitutions of Y24 and D161, which also bind to Fe1, to alanine would also disrupt the charge-transfer complex and in fact the absorbance spectra of these mutants also show a decreased absorbance at 510 nm. Crystallographic analysis also supports induced fit binding of the substrate since a water molecule occupies the apical position of Fe1 when E27 is interacting with the substrate while Y24 is no longer in the active site. This water molecule is 3.1 Å away from C1 in the structure, but could be replaced by molecular oxygen placing it within an appropriate distance from the C1 hydrogen to allow hydrogen abstraction. The subsequent catalytic steps can be anticipated to resemble the proposed mechanism of C-C bond cleavage by MIOX.[67] Molecular oxygen binds at the apical position of Fe1 (previously occupied by Y24) and is reduced to superoxide, which then abstracts the hydrogen from C1. Kinetic isotope studies on hydrogen abstraction reveal that the primary

D-KIE on $k_{cat}$ is 1.36 ± 0.06. A much higher D-KIE of ~6-7 would be expected if this step was rate limiting. However, in this case, the low D-KIE suggests that hydrogen abstraction is similar in transition state energy to other steps, resulting in a decreased D-KIE and suggesting that this is not the rate limiting step.[81,82] This value is very similar to what was observed for the analogous step performed by MIOX, where the primary D-KIE was measured to be 1.35 ± 0.35.[83] The rate limiting step is instead proposed to be the decay of the superoxide bridge intermediate.[67] The C-H bond cleavage is facilitated by resonance stabilization of the corresponding radical transition state by the α-hydroxyl group, particularly in its ionized state. A carbon-centred radical is not expected to form in this case and the electron is instead expected to delocalize into Fe2, resulting in an acyl phosphonate intermediate. The acyl phosphonate is then attacked by the adjacent hydroperoxide, with the bridging hydroxide acting as a base. The bridged peroxide is then believed to undergo homolytic cleavage yielding a ferryl oxygen and a gem-diolate phosphonate. Abstraction of the hydroxyl hydrogen by the ferryl oxygen initiates C-P bond cleavage by β-elimination of a phosphonyl radical, which may appear unusual, however this type of intermediate is well known and has been exploited in synthetic chemistry (**Figure 4-2**).[84,85] Ultimately, this forms glycine and metaphosphate, which can later be captured by water to generate $P_i$.

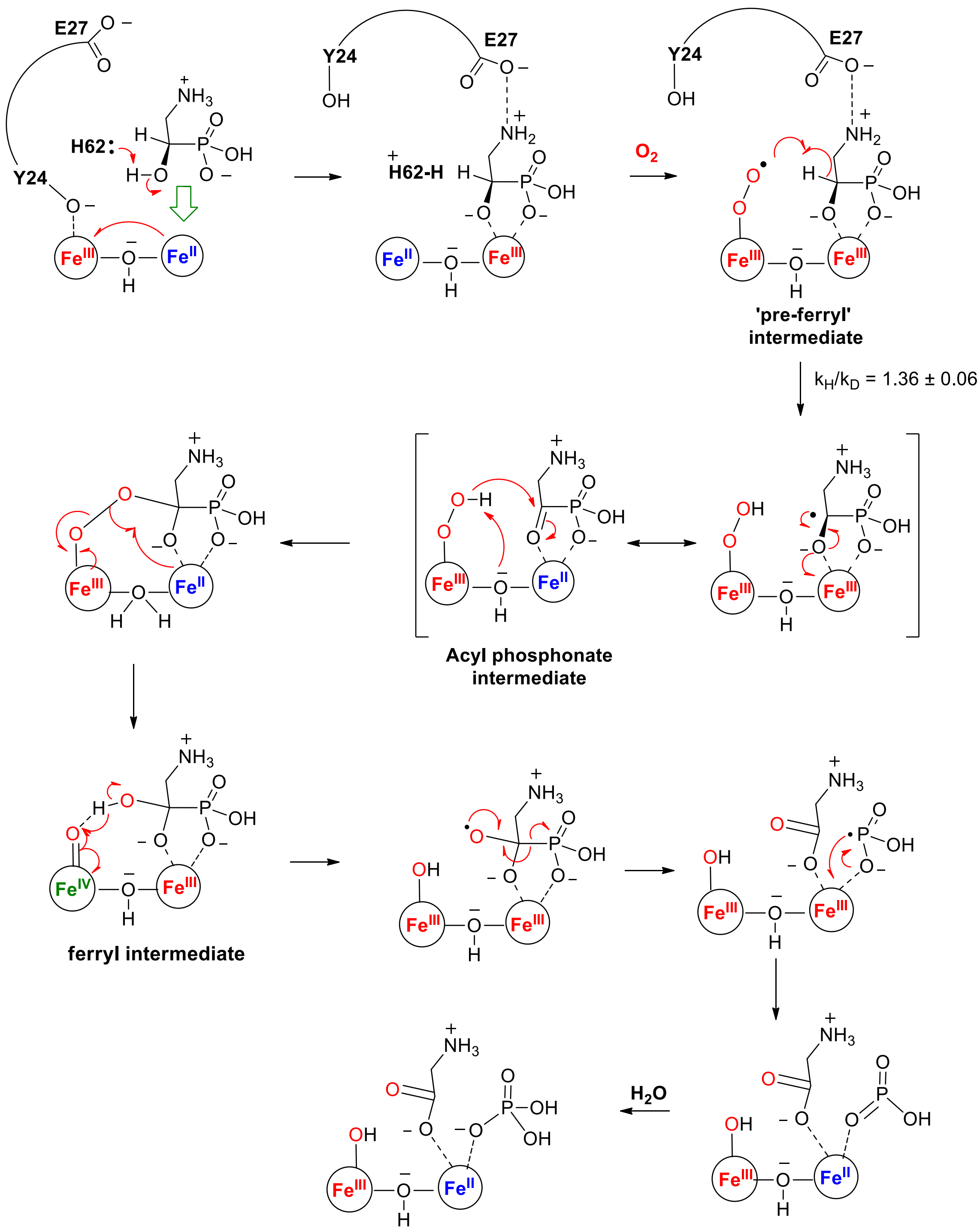


**Figure 4-1. Proposed mechanism for PhnZ.**

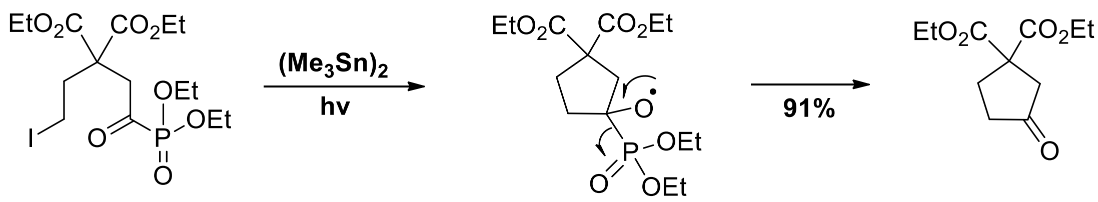

**Figure 4-2. Chemical precedence for the β–elimination of a phosphonyl radical.** Figure adapted from references 84 and 85.

### 4.2.2 Substrate specificity of PhnZ

The PhnY / PhnZ pathway has been found in various microorganisms including fungi and bacteria, and a *phnZ* gene has even been found in a mimivirus[86] suggesting that the pathway may be acquired through horizontal gene transfer. The presence of a *phnZ* gene in the mimivirus and the lack of a *phnY* gene suggests that PhnZ may be able to cleave the C-P bond of other phosphonates, or that α-hydroxyphosphonates occur in certain environments rendering PhnY redundant. This is also corroborated by the fact that a greater percentage of microorganisms contain *phnZ* than those that contain *phnZ* and *phnY* together and that 1-OH-2-AEP has been identified as a head group of lipids.[58,87,88]

PhnZ was previously co-crystallized with its native substrate (*R*)-**13** to investigate the nature of substrate binding.[61,64] The substrate (*R*)-**13** binds to Fe2 in a bidentate mode through the α-hydroxyl and one of the phosphoryl hydroxyl groups. A loop near the active site of PhnZ undergoes a conformational change upon substrate binding and closes the active site. This conformational change appears to be mediated by the interaction of E27 (a residue on the loop) that forms an electrostatic interaction with the amino group of the substrate, which would be protonated under physiological conditions. The conformational change in the loop may anchor the loop in place, and this interaction is coupled to the expulsion of Y24 from the active site creating space for molecular oxygen to bind. In summary, the α-hydroxyl of the substrate and the 2-amino group appear to be required for binding, therefore other α-hydroxy phosphonates that included or lacked the amino group were tested for activity PhnZ to probe the role of the amino group. Additionally, substrates containing heteroatoms at C1 which could assist transition state stabilization during C-H bond cleavage were also tested.

In support of the hypothesis that the amino group of the substrate is necessary to close the active site and allow the reaction to proceed is the fact that PhnZ cannot turn over a substrate lacking the amino group and a mutation of E27 to alanine decreases the $k_{cat}$ from 11 to 3 $min^{-1}$ and increases the $K_M$ from 0.17 to 1.1 mM. Crystallographic analysis of PhnZ co-crystallized with (*R*)-**17** suggests that it binds to Fe2 very similarly to the mode of the natural substrate (*R*)-**13**. Much like the "open" and "closed" conformations seen in the complex of PhnZ with (*R*)-**13** (where Y24 is in the active site in the "open" conformation and out of the active site in the "closed" conformation), (*R*)-**17** is seen bound in the active site with an "open" conformation in molecule A and a "closed" conformation in molecule B. Although the substrates bind in very similar modes, the conformation of the loop differs in the "open" conformation, where Y24 is 4.7 Å away from Fe1 and is no longer bound. It is not clear why this should prevent catalysis as molecular oxygen would appear to be free to bind to Fe1 and be reduced to superoxide. However, if the binding energy of the 2-amino group contributes significantly to transition state stabilization of the rate determining step, C-P bond cleavage would be prevented irrespective of the ability of molecular oxygen to bind to the active site.

With the knowledge of the importance of the α-hydroxyl and amino group in the substrate, other α-hydroxy phosphonates with amino groups were tested for activity with

PhnZ. Of these substrates, PhnZ was able to fully convert (1*R*, 2*R*)-**14** and (*R*)-**16,** and 50% of (+/-)-**19** to $P_i$. The first substrate, (1*R*, 2*R*)-**14**, has the α-hydroxyl in the same configuration as for (*R*)-**13** and the chain is one carbon longer, however the amino group is still at C2. Kinetic analysis of PhnZ with this substrate indicates that it has comparable kinetic parameter to those of PhnZ with the natural substrate (*R*)-**13**, with 6.2 $min^{-1}$ and 4.6 $min^{-1}$ for $k_{cat,}$ and 0.19 mM and 0.20 mM for $K_M$, for (*R*)-**13** and (1*R*, 2*R*)-**14**, respectively. Preliminary crystallographic analysis of PhnZ co-crystallized with (1*R*, 2*R*)-**14** shows that this substrate binds to Fe2 almost identically to the way (*R*)-**13** does. Molecule A from both complexes shows the loop in the closed conformation where E27 is interacting with the amino group. Superimposition of molecule A from both complexes shows almost perfect overlap between the two structures (r.m.s.d. 0.3 Å) with both substrates bound almost identically and the additional methyl group on C2 of (1*R*, 2*R*)-**14** pointing upwards toward an α-helix. The presence of the helix within the active site may restrict available space and may be the reason why (+/-)-**15**, which has an ethyl group at C2, is not a competent substrate for PhnZ.

The second substrate that was a competent substrate for PhnZ, (*R*)-**16**, has the α-hydroxyl in the same configuration as the natural substrate (*R*)-**13**, however the chain is one carbon longer with the amino group at C3. Although kinetic parameters could not be determined, preliminary kinetic experiments indicate that the reaction of PhnZ with (*R*)-**16** is approximately 10-fold slower than the reaction of PhnZ with (*R*)-**13**. Crystallographic analysis of PhnZ co-crystallized with (*R*)-**16** shows that the substrate binds to Fe2 almost identically to the way (*R*)-**13** does. However, the main difference between this complex and that of PhnZ with (*R*)-**13** is that the loop is in a much different conformation. It appears as though the active site is closed, as indicated by the interaction of E27 with the 3-amino group, however Y24 still occupies the apical site of Fe1. Analysis of the location of E27 when it interacts with the 3-amino group indicates that it is more removed from the active site than E27 in the PhnZ : (*R*)-**13** by a difference of 1.3 Å between the carbonyl carbons. This appears to cause the loop to adopt a slightly different conformation, however this small difference between the two "closed" loop conformations may be sufficient to prevent the expulsion of Y24 from the active site. If Y24 is not efficiently expelled from the active site and spends more time occupying the apical position of Fe1, this would be consistent with the observation that the reaction of PhnZ with (*R*)-**16** is much slower than with (*R*)-**13** or (1*R*, 2*R*)-**14**.

The third substrate that was competent with PhnZ is (+/-)-**19**. PhnZ is capable of converting 50% of a racemic mixture of this substrate, and the fact that PhnZ has only been able to accept (*R)*-α-hydroxy phosphonates suggests that PhnZ likely accepts only (*R*)-**19**, however this remains to be tested. This suggests that PhnZ may be able to accept other *N*-functionalized α-hydroxyphosphonates, which makes it more promising that it could be engineered to accept a substrate such as glyphosate.

### 4.2.3 Engineering the substrate specificity of PhnZ

In order to attempt engineering of the substrate specificity of PhnZ, the coupled interaction between Y24 and E27 was further investigated to determine the importance of the role they play in substrate binding. Previously reported kinetic parameters of the Y24F variant are very similar to those of the WT with no apparent loss of activity and only a slight increase in $K_M$ from 0.17 to 0.26 mM.[64] However, the E27A variant resulted in a dramatic loss of activity with a decrease in $k_{cat}$ from 11 to 3 min$^{-1}$ and almost a 10-fold increase in $K_M$ to 1.1 mM.[64] These kinetic parameters are consistent with E27 playing a role in substrate binding. A truncated substrate lacking the 2-amino group, (*R*)-**17**, was therefore tested as a substrate for Y24F to determine if the dependence of the amino group could be removed if Y24 was not occupying the molecular oxygen binding site. However, (*R*)-**17** was not a competent substrate for the WT enzyme nor the Y24F or E27A variants suggesting that the interaction of E27 with the amino group of the substrate was either necessary for catalysis or that the charged E27 residue forms unfavourable interactions within the active site in the absence of the charged amino group, however the latter can now be discounted by crystallographic analysis with suggests otherwise.

To further investigate the coupled interaction between Y24 and E27, a double mutant containing both the Y24F and E27A mutations was produced to verify the effect both mutations had on catalysis. PhnZ Y24F/E27A was first tested with the native substrate (*R*)-**13** and surprisingly, all activity had been abolished. This has a few implications, firstly, substituting both of these residues may have a detrimental effect on the flexibility and motion of the loop, or secondly, that E27 may play a more important role in substrate binding than previously believed. Enzymes use much of the energy associated with substrate binding to stabilize the rate determining transition state for catalysis, and in some cases this can be increased through a flexible loop that closes over the active site to exclude solvent. In the case of triosephosphate isomerase (TIM), the phosphate moiety of its substrate glyceraldehyde-3-phosphate (GP) is used as a clamp to close the active site by means of a flexible loop that closes off the active site to water and optimizes transition state interactions.[89] The activity of TIM when its substrate is truncated to one lacking the phosphate dramatically decreases.[90] However, activity can be rescued by the addition of phosphite. Although this moiety is not attached to the substrate, it maintains its role of interacting with the flexible loop to keep TIM in the active closed conformation. A direct comparison of this effect can be made to the role of the flexible loop of PhnZ. It can be hypothesized that the amino group of the substrate (*R*)-**13** may play a role analogous to that of the phosphate group of GP. Therefore, it would be interesting to see if the addition of a high concentration of ammonium ion to the reaction of PhnZ with (*R*)-**17** would rescue its activity. Likewise, it would also be interesting to see if the substitution of an active site residue for lysine could provide the same effect to favour the closed conformation of PhnZ.

In examination of the activity of PhnZ with (*R*)-**14,** it is clear that the location of interaction between the amino group of the substrate and E27 is important, since Y24 does not appear to be expelled efficiently when the loop adopts this particular conformation. Therefore, this should be investigated further to determine if the coordination of Y24 to Fe1 is in fact causing the decreased activity or if it is a result of incomplete closure of the active site by the loop. If the Y24F variant is more active with (*R*)-**14** than the WT enzyme, then this may be an indication that Y24 is not efficiently expelled from the active site. However, if the Y24F variant is not more active, then this would be an indication that E27 binds the substrate in a manner that does not sufficiently close the active site. This hypothesis could then be tested with a E27D substitution, wherein the shorter Asp side chain would complement the additional space occupied by the longer substrate (*R*)-**14**.

### 4.3 Engineering the PhnY / PhnZ pathway

The investigation of the substrate specificity of PhnZ has revealed that the α-hydroxyl group is strictly required for catalysis (**Table 3-4**). PhnZ is also unreactive with substrates containing a heteroatom (O, N) attached to the alpha carbon unless it is in the form of a hydroxyl group. Therefore, for PhnZ to be able to degrade a phosphonate such as glyphosate, an enzyme is required that will catalyze the hydroxylation of the $\alpha$-carbon. Lack of crystallographic data for PhnY presents an obstacle for rational engineering of its substrate specificity, therefore directed evolution may be a more successful route to engineer the pathway for degradation of glyphosate. Directed evolution mimics natural selection by introducing mutations at the DNA-level using random mutagenesis with methods such as error-prone PCR and DNA shuffling. The mutated genes can then be transformed into an *E. coli* strain lacking a functional CP-lyase pathway for expression, and screened for the desired function.[91] In the case of PhnY and PhnZ, it would be simple to select for desirable PhnY and PhnZ variants since *E. coli* transformed with the mutated genes could be grown on minimal media containing glyphosate as the sole source of $P_i$. Only cells containing PhnY and PhnZ variants that are proficient in converting glyphosate to $P_i$ and glycine would allow growth on the glyphosate medium.

# Chapter 5

## Conclusions and future work

In this thesis, improvements have been made to the expression and purification procedures for PhnY making it a better candidate for crystallography, however the stability of PhnY under crystallization conditions remains an obstacle for obtaining a crystal structure. A crystal structure of PhnY would be of utmost importance to determine active site residues necessary for catalysis and to alter substrate specificity by rational design. However, we are now in possession of deuterated substrates that can be used to derive mechanistic information by KIE analysis on hydrogen abstraction to determine if this step is rate limiting.

The kinetic parameters of PhnY have been determined and appear to be in agreement with the hypothesis that PhnY and PhnZ work together in a pathway to degrade 2-AEP. PhnY has been found to be very specific for this substrate, however it remains to see if a crystal structure can be obtained to allow rational engineering of the active site or if directed evolution will be required to alter its specificity.

A more complete mechanism for PhnZ has now been proposed based on kinetic and crystallographic analysis. The similarities between the mechanisms of PhnZ and MIOX are also more evident, as can be seen by the unusually low primary deuterium KIE on hydrogen abstraction observed for both enzymes.

The role of the flexible loop near the active site and the substrate specificity of PhnZ are now much better understood and provide a basis for rational design of the substrate specificity. A double mutant of PhnZ including both the E27A and Y24F mutations was produced in order to establish the extent of the role they play in substrate binding and catalysis. This mutant was found to have lost all activity, suggesting that they do in fact play an active role in substrate binding.

Crystallographic analysis of PhnZ co-crystallized with substrate analogues provided further insight into the roles of E27 and Y24 in substrate specificity and provided explanations to corroborate kinetic data. PhnZ was found to accept some bulk in its active site, as seen with (1*R*, 2*R*)-**14** and (*R*)-**14,** however the position of the amino group on the substrate appears to be important. When the amino group is on C3 as opposed to C2, conformational changes occur in the flexible loop that are significant enough to prevent efficient expulsion of Y24 from the active site resulting in at least 10-fold reduced activity. In contrast, when the amino group is on C2, kinetic parameters similar to those seen with the natural substrate (*R*)-**13** are seen. Crystallographic analysis of PhnZ with a truncated substrate lacking the amino group, (*R*)-**17**, reveal that the loop adopts similar conformations as it does when (*R*)-**13** is bound with the exception that Y24 is no longer a ligand for Fe1. Y24 remains within close proximity to Fe1, however the lack of coordination between the two may suggest that the loop is highly flexible in the absence of an amino group in the active that can serve as an anchor to maintain closure of the active site.

Future experiments should focus on obtaining a crystal structure of PhnY or a close homolog to propose a more detailed mechanism and to provide a basis for rational engineering of its substrate specificity, as well as to carry out KIE analysis to determine if hydrogen abstraction is the rate-limiting step. Future experiments for PhnZ should investigate the role of the substrate amino group and explore methods to compensate for its interaction with E27 to alter substrate specificity. Active site substitutions could also be made such as E27D to determine if this would allow PhnZ to accept a longer substrate with an amino group at C3, or if the Y24F variant is sufficient to regain full activity of PhnZ with longer α-hydroxy phosphonates containing terminal amino groups.

Directed evolution may be a promising route to engineer the PhnY / PhnZ pathway and would be worth exploring to be able to create variants that can degrade alternative alkylphosphonates, such as glyphosate, the active component of RoundUp herbicide.

# Chapter 6

## References


1. Westheimer, F. H. Why nature chose phosphates. *Science* **1987**, *235*, 1173-1178.

2. Kononova, S. V.; Nesmeyanova, M. A. Phosphonates and their degradation by microorganisms. *Biochemistry (Moscow)* **2002**, *67*, 220-233.

3. Freedman, L. D.; Doak, G. O. The preparation and properties of phosphonic acids. *Chem. Rev.* **1957**, *57*, 479-523.

4. McGrath, J. W.; Chin, J. P.; Quinn, J. P. Organophosphonates revealed: new insights into the microbial metabolism of ancient molecules. *Nat. Rev. Microbiol.* **2013**, *11*, 412-419.

5. de Graaf, R. M.; Visscher, J.; Schwartz, A. W. A plausibly prebiotic synthesis of phosphonic acids. *Nature* **1995**, *378*, 474-477.

6. Schwartz, A. W. Phosphorus in prebiotic chemistry. *Phil. Trans. R. Soc.* **2006**, *361*, 1743-1749.

7. Horiguchi, M.; Kandatsu, M. Isolation of 2-aminoethane phosphinic acid from rumen protozoa. *Nature* **1959**, *184*, 901-902.

8. Moschidis, M. C. Phosphonolipids. *Prog. Lipid Res.* **1985**, *23*, 223-246.

9. Metcalf, W.; van der Donk, W. Biosynthesis of phosphonic and phosphinic acid natural products. *Annu. Rev. Biochem.* **2009**, *78*, 65-94.

10. Warren, W. A. Biosynthesis of phosphonic acids in Tetrahymena. *Biochim. Biophys. Acta.* **1968**, *156*, 340-346.

11. Bowman, E.; McQueney, M.; Barry, R. J.; Dunaway-Mariano, D. Catalysis and thermodynamics of the phosphoenolpyruvate/phosphonopyruvate rearrangement. Entry into the phosphonate class of naturally occurring organophosphorus compounds. *J. Am. Chem. Soc.* **1988**, *110*, 5575-5576.

12. Horiguchi, M. Biosynthesis of 2-aminoehtylphosphonic acid in cell-free preparations from tetrahymena. *BBA-Gen. Subjects* **1972**, *261*, 102-113.

13. Horiguchi, M.; Rosenberg, H. Phosphonopyruvic acid: a probable precursor of phosphonic acids in cell-free preparations of tetrahymena. *Biochim. Biophys. Acta* **1975**, *404*, 333-340.

14. Seidel, H. M.; Freeman, S.; Seto, H.; Knowles, J. R. Phosphonate biosynthesis: isolation of the enzyme responsible for the formation of a carbon-phosphorus bond. *Nature* **1988**, *335*, 457-458.

15. Barry, R. J.; Bowman, E.; McQueney, M.; Dunaway-Mariano, D. Elucidation of the 2-aminoethylphosphonate biosynthetic pathway in *Tetrahymena pyriformis*. *Biochem. Bioph. Res. Co.* **1988**, *153*, 177-182.

16. Jia, Y.; Lu, Z.; Huang, K.; Herzberg, O.; Dunaway-Mariano, D. Insight into the mechanism of phosphoenolpyruvate mutase catalysis derived from site-directed mutagenesis studies of active site residues. *Biochemistry* **1999**, *38*, 14165-14173.

17. Liu, S.; Lu, Z.; Jia, Y.; Dunaway-Mariano, D.; Herzberg, O. Dissociative phosphoryl transfer in PEP mutase catalysis: structure of the enzyme/sulfopyruvate complex and kinetic properties of mutants. *Biochemistry* **2002**, *41*, 10270-10276.

18. Yamato, M; Koguchi, T.; Okachi, R.; Yamada, K.; Nakayama, K.; Kase, H.; Karasawa, A.; Shuto, K. K-26, a novel inhibitor of angiotensin I converting enzyme produced by an actinomycete K-26. *J. Antibiot. (Tokyo)* **1986**, *39*, 44-52.

19. Ntai, I.; Manier, M. L.; Hachey, D. L.; Bachmann, B. O. Biosynthetic origins of C-P bond containing tripeptide K-26. *Org. Lett.* **2005**, *7*, 2763-2765.

20. Ntai, I.; Phelan, V. V.; Bachmann, B. O. Phosphonopeptide K-26 biosynthetic intermediates in *Astrosporangium hypotensionis*. *Chem. Commun.* **2006**, *43*, 4518-4520.

21. Phelan, V. V. Biosynthetic investigations of the peptide natural products K-26 and anthramycin. PhD thesis, Vanderbilt University, **2010**.

22. Werner, W. J.; Allen, K. D.; Hu, K.; Helms, G. L.; Chen, B. S.; Wang, S. C. *In vitro* phosphinate methylation by PhpK from *Kitasatospora phosalacinea*. *Biochemistry* **2011**, *50*, 8986-8988.

23. Sviridov, A. V.; Shushkova, T. V.; Ermakova, I. T.; Ivanova, E. V.; Leontievsky, A. A. Glyphosate: safety risks, biodegradation and bioremediation. *Current Environmental Issues and Challenges*. Springer Netherlands, **2014**, 183-195.

24. Rueppel, M. L.; Brightwell, B.B.; Schaefer, J.; Marvel, J. T. Metabolism and degradation of glyphosate in soil and water. *J. Agric. Food Chem.* **1977**, *25*, 517-528.

25. Lund-Høie, K.; Friestad, H.O. Photodegradation of the herbicide glyphosate in water. *Bull. Environ. Contam. Toxicol.* **1986**, *36*, 723–729.

26. Williams, G. M.; Kroes, R.; Munro, I. C. Safety evaluation and risk assessment of the herbicide Roundup and its active ingredient, glyphosate, for humans. *Reg. Toxicol. Pharmacol.* **2000**, *31*, 117–165.

27. Hove-Jensen, B.; Zechel, D. L.; Jochimsen, B. Utilization of glyphosate as phosphate source: biochemistry and genetics of bacterial carbon-phosphorus lyase. *Microbiol. Mol. Biol. Rev.* **2014**, *78*, 176-197.

28. Helander, M.; Saloniemi, I.; Saikkonen, K. Glyphosate in northern ecosystems. *Trends Plant Sci.* **2012**, *17*, 569-574.

29. Wardle, D. A; Parkinson, D. Influence of the herbicides 2,4-D and glyphosate on soil microbial biomass and activity: a field experiment. *Soil Biol. Biochem*. **1992**, *24*, 185–186.

30. Benachour, N.; Seralini, G.E. Glyphosate formulations induce apoptosis and necrosis in human umbilical, embryonic, and placental cells. *Chem. Res. Toxicol.* **2009**, *22*, 97-105.

31. Gasnier, C.; Dumont, C.; Benachour, N.; Clair, E.; Chagnon, M. C.; Seralini, G. E. Glyphosate-based herbicides are toxic and endocrine disruptors in human cell lines. *Toxicology* **2009**, *262*, 184-191.

32. Paganelli, A.; Gnazzo, V.; Acosta, H.; Lopez, S. L.; Carrasco, A. E. Glyphosate-based herbicides produce teratogenic effects on vertebrates by impairing retinoic acid signaling. *Chem. Res. Toxicol.* **2010**, *23*, 1586-1595.

33. Hsieh, Y.-J.; Wanner, B. L. Global regulation by the seven-component PI signaling system. *Curr. Opin. Microbiol*. **2010**, *13*, 198-203.

34. Quinn, J. P.; Kulakove, A. N.; Cooley, N. A.; McGrath, J. W. New ways to break an old bond: the bacterial carbon-phosphorus hydrolases and their role in biogeochemical phosphorus cycling. *Environ. Microbiol.* **2007**, *9*, 2392-2400.

35. White, A. K.; Metcalf, W. W. Microbial metabolism of reduced phosphorus compounds. *Annu. Rev. Microbiol.* **2007**, *61*, 379-400.

36. Nigel, G. T.; McGrath, J. W.; McMullan, G.; Quinn, J. P. Review: Organophosphonates: occurrence, synthesis and biodegradation by microorganisms. *World J. Microb. Biot.* **1998**, *14*, 635-647.

37. Baker, A.; Ciocci, M.; Metcalf, W.; Kim, J.; Babbitt, P.; Wanner, B.; Martin, B. M.; Dunaway-Mariano, D. Insights into the mechanism of catalysis by the P-C bond cleaving enzyme phosphonoacetaldehyde hydrolase derived from gene sequence analysis and mutagenesis. *Biochemistry* **1998**, *37*, 9305-9315.

38. Morais, M.; Zhang, W.; Baker, A.; Zhang, G.; Dunaway-Mariano, D.; Allen, K. The Crystal structure of *Bacillus cereus* phosphonoacetaldehyde hydrolase: insight into catalysis of phosphorus bond cleavage and catalytic diversification within the HAD enzyme superfamily. *Biochemistry* **2000**, *39*, 10385-10396.

39. Morais, M.; Zhang, G. Z.; Olsen, D. B.; Dunaway-Mariano, D.; Allen, K. X-ray crystallographic and site-directed mutagenesis analysis of the mechanism of Schiff-base formation in phosphonoacetaldehyde hydrolase catalysis. *J. Biol. Chem.* **2004**, *279*, 9353-9361.

40. Lahiri, S.; Zhang, G.; Dunaway-Mariano, D.; Allen, K. Diversification of function in haloacid dehalogenase enzyme superfamily: the role of the cap domain in hydrolytic phosphorus-carbon bond cleavage. *Bioorg. Chem.* **2006**, *34*, 394-409.

41. Chen, C.; Han, Y.; Niu, W.; Kulakova, A. N.; Howard, A.; Quinn, J. P.; Dunaway-Mariano, D.; Herzberg, O. Structure and kinetics of phosphonopyruvate hydrolase from *Voriovorax sp.* Pal2: New insight into the divergence of catalysis within the PEP mutase/isocitrate lyase superfamily. *Biochemistry* **2006**, *45*, 11491-11504.

42. Agarwal, V.; Borisova, S.; Metcalf, W.; van der donk, W.; Nair, S. Structural and mechanistic insights into C-P bond hydrolysis by phosphonoacetate hydrolase. *Chem. Biol.* **2011**, *18*, 1230-1240.

43. Kamat, S. S.; Raushel, F. M. The enzymatic conversion of phosphonates to phosphate by bacteria. *Curr. Opin. Chem. Biol.* **2013**, *17*, 589-596.

44. Huang, J.; Su, Z.; & Xu, Y. The evolution of microbial phosphonate degradative pathways. *J. Mol. Evol.*, **2005**, *61*, 682-690.

45. Wackett, L.; Shames, S.; Venditti, C.; Walsh, C. Bacterial carbon-phosphorus lyase: Products, ratesm and regulation of phosphonic and phosphinic acid metabolism. *J. Bacteriol.* **1987**, *169*, 710-717.

46. Chen, C. M.; Ye, Q. Z.; Zhu, Z. M.; Wanner, B. L.; Walsh, C.T. Molecular biology of carbon-phosphorus bond cleavage. Cloning and sequencing of the *phn* (*psiD*) genes involved in alkylphosphonate uptake and C-P lyase activity in *Escherichia coli*. *J. Biol. Chem.* **1990**, *265*, 4461-4471.

47. Zhang, Q.; van der Donk, W. A. Answers to the carbon-phosphorus lyase conundrum. *Chembiochem* **2012**, *13*, 627-629.

48. Kamat, S. S.; Williams, H. J.; Raushel, F. M. Intermediates in the transformation of phosphonates to phosphate by bacteria. *Nature* **2011**, *480*, 570-573.

49. Hove-Jensen, B.; Rosenkrantz, T. J.; Haldimann, A.; Wanner, B. L. *Escerichia coli phnN*, encoding ribose 1,5-bisphosphokinase activity (phosphoribosyl disphosphate

forming): dual role in phosphonate degradation and NAD biosynthesis pathways. *J. Bacteriol.* **2003**, *185*, 2793-2801.

50. Hove-Jensen, B.; McSorley, F. R.; Zechel, D. L. Catabolism and detoxification of 1-aminoalkylphosphonic acids: N-acetylation by the phnO gene product. *PLoS ONE* **2012**, *7*, e46416.

51. Hove-Jensen, B.; McSorley, F. R.; Zechel, D. L. Physiological role of PhnP-specified phosphoribosyl cyclic phosphodiesterase in catabolism of organophosphinic acids by the carbon-phosphorus lyase pathway. *J. Am. Chem. Soc.* **2011**, *133*, 3617-3624.

52. Frost, J.; Loo, S. C.; Li, D. Radical-based dephosphorylation and organophosphonate biodegradation. *J. Am. Chem. Soc.* **1987**, *109*, 2166-2171.

53. Frey, P.; Hegerman, A. The radical SAM superfamily. *Crit. Rev. Biochem. Mol.* **2008**, *43*, 63-88.

54. Kamat, S. S.; Williams H. J.; Dangott, L. J.; Chakrabarti, M.; Raushel, F. M. The catalytic mechanism for aerobic formation of methane by bacteria. *Nature* **2013**, *497*, 132-136.

55. Jochimsen, B.; Lolle, S.; McSorley, F. R.; Nabi, M.; Stougaard, J.; Zechel, D. L.; Hove-Jensen, B. Five phosphonate operon gene products as components of a multi-subunit complex of the carbon-phosphorus lyase pathway. *Proc. Natl. Acad. Sci. U.S.A.* **2011**, *108*, 11393-11398.

56. Seweryn, P.; Van, L. B.; Kjeldgaard, M.; Russo, C. J.; Passmore, L. A.; Hove-Jensen, B.; Jochimsen, B.; Brodersen, D. E. Structural insights into the bacterial carbon-phosphorus lyase machinery. *Nature* **2015**, *submitted.*

57. Adams, M. A.; Luo, Y.; Hove-Jensen, B.; He, S.-M.; van Staalduinen, L. M.; Zechel, D. L.; Jia, Z. Crystal structure of PhnH: an essential component of carbon-phosphorus lyase in *Escherichia coli*. *J. Bacteriol*. **2008**, *190*, 1072-1083.

58. Martinez, A.; Tyson, G. D. Widespread known and novel phosphonate utilization pathways in marine bacteria revealed by functional screening and metagenomic analyses. *Environ. Microbiol.* **2010** *12*, 222-238.

59. McSorley, F. R.; Wyatt, P. B.; Martinez, A.; DeLong, E. F.; Hove-Jensen, B.; Zechel, D. L. PhnY and PhnZ comprise a new oxidative pathway for enzymatic cleavage of a carbon-phosphorus bond. *J. Am. Chem. Soc.* **2012**, *134*, 8364-8367.

60. Circello, B. T.; Eliot, A. C.; Lee, J.; van der Donk, W. A.; Metcalf, W. W. Molecular cloning and heterologous expression of the dehydrophos biosynthetic gene cluster. *Chem. Biol*. **2010**, *17*, 402-411.

61. Wörsdörfer, B.; Lingaraju, M.; Yennawar, N. H.; Boala, A. K.; Krebs, C.; Bollinger, Jr, J. M.; Pandelia, M.-E. Organophosphonate-degrading PhnZ reveals an emerging family of HD domain mixed-valent diiron oxygenases. *Proc. Natl. Acad. Sci. U.S.A.* **2013**, *110*, 18874-18879.

62. van Staalduinen, L. M. Structural insights into novel microbial metalloenzymes. Ph. D. thesis, Queen's University, **2013**.

63. Xing, G.; Barr, E. W.; Diao, Y.; Hoffart, L. M.; Prabhu, K. S.; Arner, R. J.; Reddy, C. C.; Krebs, C.; Bollinger Jr., J. M. Oxygen activation by a mixed-valent , diiron(II/III) cluster in the glycol cleavage reaction catalyzed by *myo*-inositol oxygenase. *Biochemistry* **2006**, *45*, 5402-5412.

64. van Staalduinen, L.; McSorley, F. R.; Schiessl, K.; Séguin, J.; Wyatt, P. B.; Hammerschmidt, F.; Zechel, D. L.; Jia, Z. Crystal structure of PhnZ in complex with substrate reveals a di-iron oxygenase mechanism for catabolism of organophosphonates. *Proc. Natl. Acad. Sci.* **2014**, *111*, 5171–5176.

65. Eichhorn, E.; van der Ploeg, J. R.; Kertesz, M. A.; Leisinger, T. Characterization of the α-ketoglutarate-dependent taurine dioxygenase from *Escherichia coli*. *J. Biol. Chem.* **1997**, *272*, 23031-23036.

66. McSorley, F. R. Enzymatic cleavage of carbon-phosphorus bonds. Ph. D. thesis, Queen's University, **2013**.

67. Hirao, H.; Morokuma, K. Insights into the (superoxo)Fe(III)Fe(III) intermediate and reaction mechanism of *myo*-inositol oxygenase: DFT and ONIOM(DFT:MM) Study. *J. Am. Chem. Soc.* **2009**, *131*, 17206-17214.

68. Hartley, L.; Kaakoush, N.; Ford, J.; Korolik, V.; & Mendz, G. Characterisation of Campylobacter jejuni genes potentially involved in phosphonate degradation. *Gut Pathogens* **2009**, *1*, 1-9.

69. Ford, J.; Kaakoush, N.; Mendz, G. Phosphonate metabolism in Helicobacter pylori. *Antonie van Leeuwenhoek* **2010**, *97*, 51-60.

70. Beutler, H. O. Succinate. *Methods of Enzymatic Analysis*, 3rd ed., Vol. VII, (Bergmeyer, H. U., ed.), VCH Publishers (UK) Ltd., Cambridge, UK, **1989**, 25-33.

71. Pegan, S. D.; Tian, Y.; Sershon, V.; Mesecar, A. D. A universal, fully automated high throughput screening assay for pyrophosphate and phosphate release from enzymatic reactions. *Comb. Chem. High T. Scr.* **2010**, *13*, 27-38.

72. Webb, M. R. A continuous spectrophotometric assay for inorganic phosphate and for measuring phosphate release kinetics in biological systems. *Proc. Natl. Acad. Sci. USA* **1992**, *89*, 4884-4887.

73. Kabsch, W. XDS. *Acta. Crystallogr. D. Biol. Crystallogr.* **2010**, *66*, 125–132.

74. Matthews, B. W. Solvent content of protein crystals. *J. Mol. Biol.* **1968**, *33*, 491–497.

75. McCoy, A. J.; Grosse-Kunstleve, R. W.; Adams, P. D.; Winn, M. D.; Storoni, L. C.; Read, R. J. *Phaser* crystallographic software. *J. Appl. Cryst.* **2007**, *40*, 658-674.

76. Adams, P. D.; Afonine, P. V.; Bunkóczi, G.; Chen, V. B.; Davis, I. W.; Echols, N.; Head, J. J.; Hung, L.-W.; Kapral, G. J.; Grosse-Kunstleve, R. W.; McCoy, A. J.; Moriarty, N. W.; Oeffner, R.; Read, R. J.; Richardson, D. C.; Richardson, J. S.; Terwilliger, T. C.; Zwart, P. H. PHENIX: a comprehensive Python-based system for macromolecular structure solution. *Acta. Crystallogr. D. Biol. Crystallogr.* **2010,** *66*, 213–221.

77. Emsley, P.; Lohkamp, B.; Scott, W. G.; Cowtan, K . Features and development of Coot. *Acta. Crystallogr. D. Biol. Crystallogr.* **2010,** *66*, 486–501.

78. Benvenuti1, M.; Mangani, S. Crystallization of soluble proteins in vapor diffusion for x-ray crystallography. *Nat. Protoc*. **2007**, *2*, 1633-1651.

79. Brown, P. M.; Caradoc-Davies, T. T.; Dickson, J. M. J.; Cooper, G. J. S.; Loomes, K. M. Crystal structure of a substrate complex of *myo*-inositol oxygenase, a di-iron oxygenase with a key role in inositol metabolism. *Proc. Natl. Acad. Sci. U.S.A.* **2006**, *103*, 15032-15037.

80. Xiang, D. F.; Kolb, P.; Fedorov, A. A.; Meier, M. M.; Fedorov, L. V.; Nguyen, T. T.; Sterner, R.; Almo, S. C., Shoichet, B. K.; Raushel, F. M. Functional annotation and three-dimensional structure of Dr0930 from *Deinococcus radiodurans*, a close relative of phosphotriesterase in the amidohydrolase superfamily. *Biochemistry* **2009**, *48*, 2237–2247.

81. Berti, P. J.; Tanaka, K. S. E. Transition state analysis using multiple kinetic isotope effects : mechanisms of enzymatic and non-enzymatic glycoside hydrolysis and transfer. *Adv. Phys. Org. Chem.* **2002**, *37*, 239-314.

82. Bugg, T. D. H. Introduction to Enzyme and Coenzyme Chemistry, 2nd ed., *Blackwell Publishing*, **2004**.

83. Xing, G.; Dlao, Y.; Hoffart, L. M.; Barr, E. W.; Prabhu, K. S.; Arner, R. J.; Reddy, C. C.; Krebs, C.; Bollinger Jr., J. M. Evidence for C-H cleavage by an iron-superoxide complex in the glycol cleavage reaction catalyzed by *myo*-inositol oxygenase. *Proc. Natl. Acad. Sci. USA* **2006**, *103*, 6130-6135.

84. Kim, S.; Cho, C. H.; Lim, C. J. β-Elimination of a phosphonate group from an alkoxy radical: an intramolecular acylation approach using an acylphosphonate as a carbonyl group acceptor. *J. Am. Chem. Soc.* **2003**, *125*, 9574-9575.

85. Leca, D.; Fensterbank, L.; Lacôte, E.; Malacria, M. Recent advances in the use of phosphorus-centered radicals in organic chemistry. *Chem. Soc. Rev.* **2005**, *34*, 858-865.

86. Raoult, D.; Audic, S; Robert, C.; Abergel, C.; Renesto, P.; Ogata, H.; La Scola, B.; Suzan, M.; Claverie, J.-M. The 1.2-megabase genome sequence of mimivirus. *Science* **2004**, *306*, 1344-1350.

87. Korn, E. D.; Dearborn, D. G.; Fales, H. M.; Sokoloski, E. A. Phosphonoglycan. A major polysaccharide constituent of the amoeba plasma membrane contains 2-aminoethylphosphonic acid and 1-hydroxy-2-aminoethylphosphonic acid. *J. Biol. Chem.* **1973**, 248, 2257–2259.

88. Watanabe, Y.; Nakajima, M.; Hoshino, T.; Jayasimhulu, K.; Brooks, E. E.; Kaneshiro, E. S. A novel sphingophosphonolipid head group 1-hydroxy-2-aminoethyl phosphonate in *Bdellovibrio stolpii*. *Lipids* **2001,** *36*, 513–519.

89. Malabanan, M. M.; Amyes, T. L.; Richard, J. P. A role for flexible loops in enzyme catalysis. *Current Opinion in Structural Biology* **2010**, *20*, 702-710.

90. Malabanan, M. M.; Koudelka, A. P.; Amyes, T. L.; Richard, J. P. Mechanism for activation of triosephosphate isomerase by phosphite dianion : the role of a hydrophobic clamp. *J. Am. Chem. Soc.* **2012**, *134*, 10286-10298.

91. Bornscheuer, U.T.; Pohl, M. Improved biocatalysts by directed evolution and rational protein design. *Curr. Opin. Chem. Biol.* **2001**, 5, 137-143.

# Appendix A

## $^{31}$P-NMR spectra for PhnY reactions

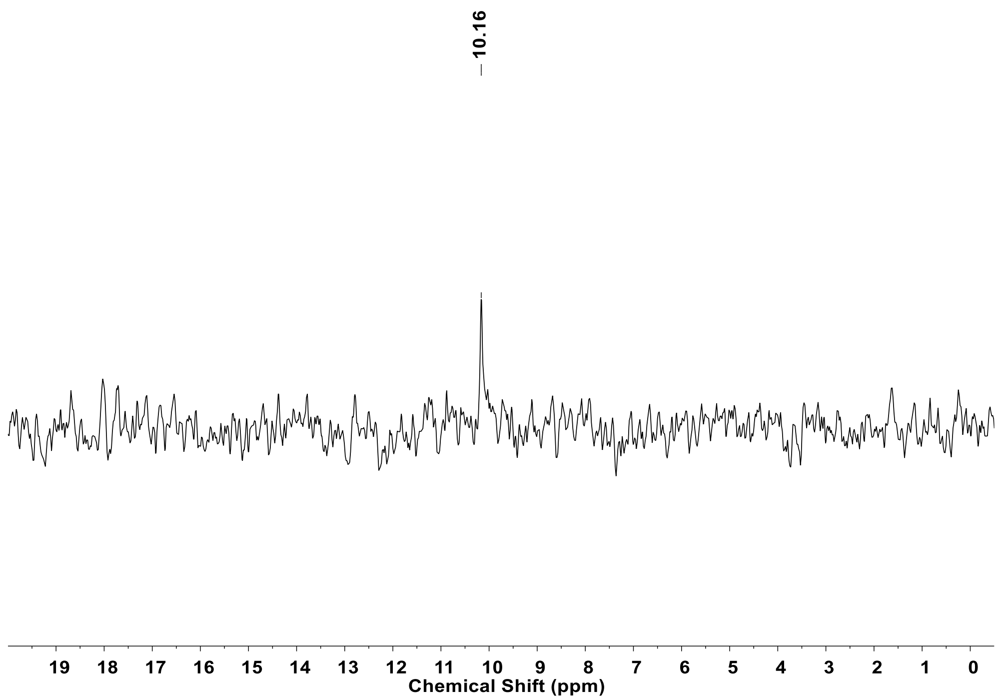


**Figure A 1.** $^{31}$P-NMR spectrum of enzyme-free control with **1**.

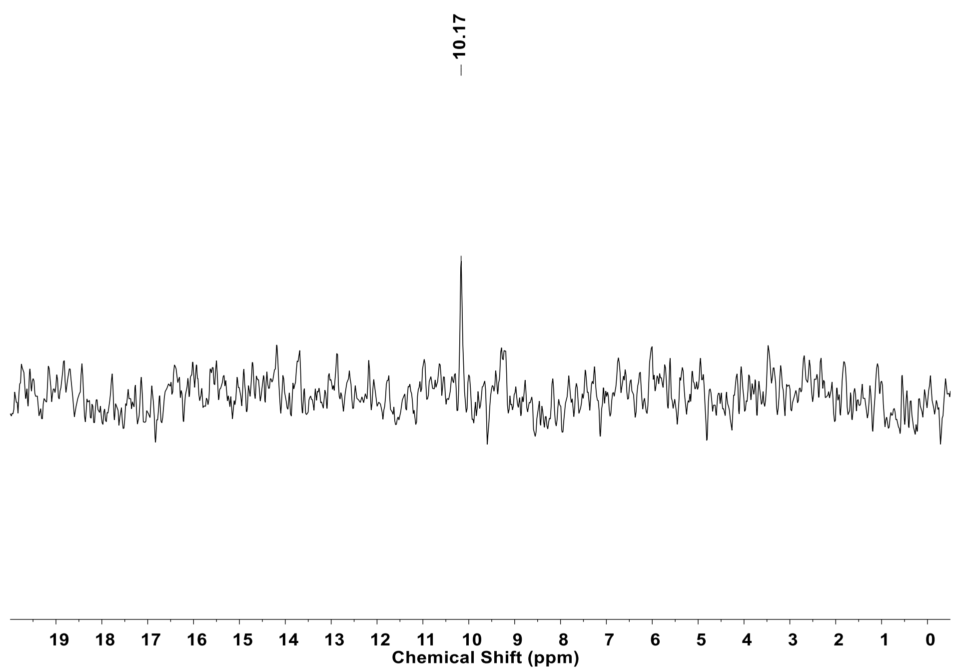


**Figure A 2.** $^{31}$P-NMR spectrum of PhnY reaction with **1**.

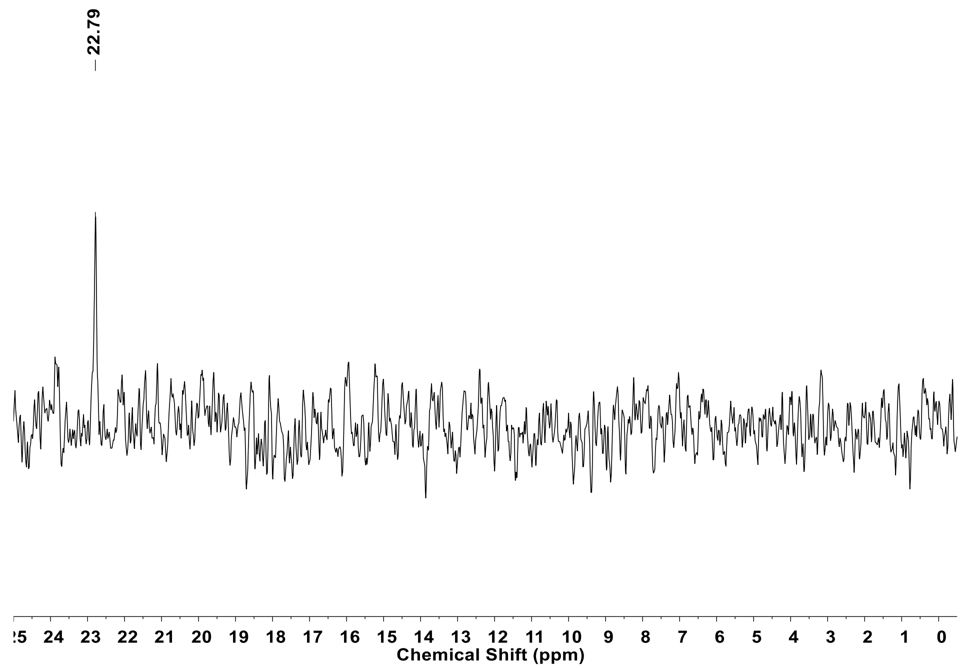


**Figure A 3.** $^{31}$P-NMR spectrum of enzyme-free control with **3**.

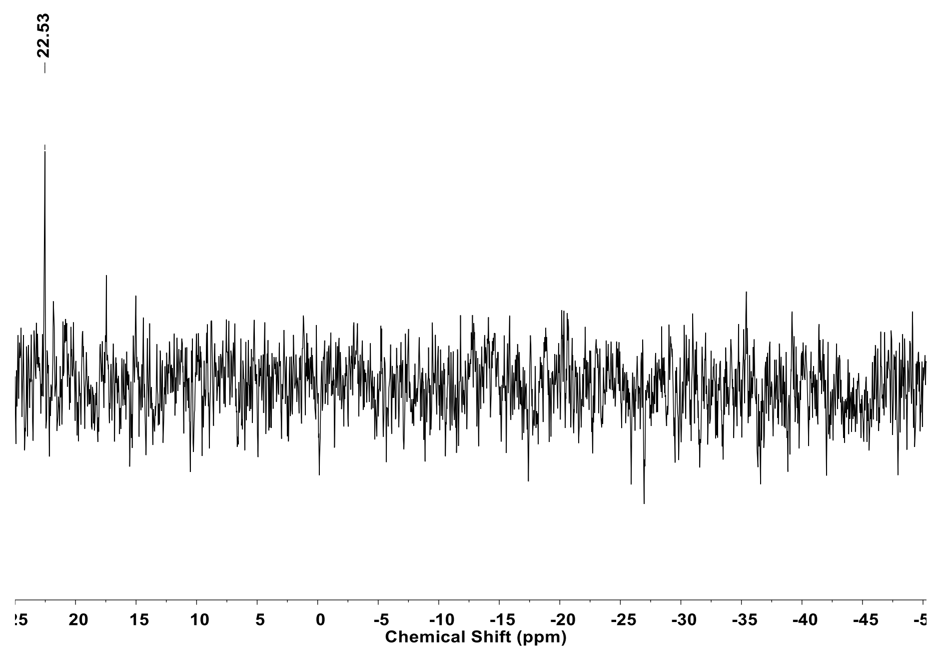


**Figure A 4.** $^{31}$P-NMR spectrum of PhnY reaction with **3**.

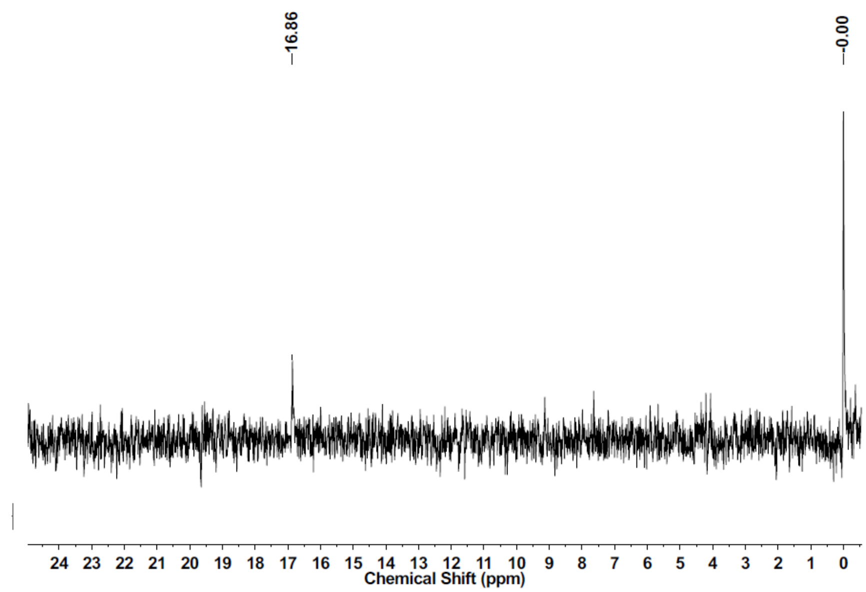


**Figure A 5.** $^{31}$P-NMR spectrum of enzyme-free control with (*S*)-**4**.

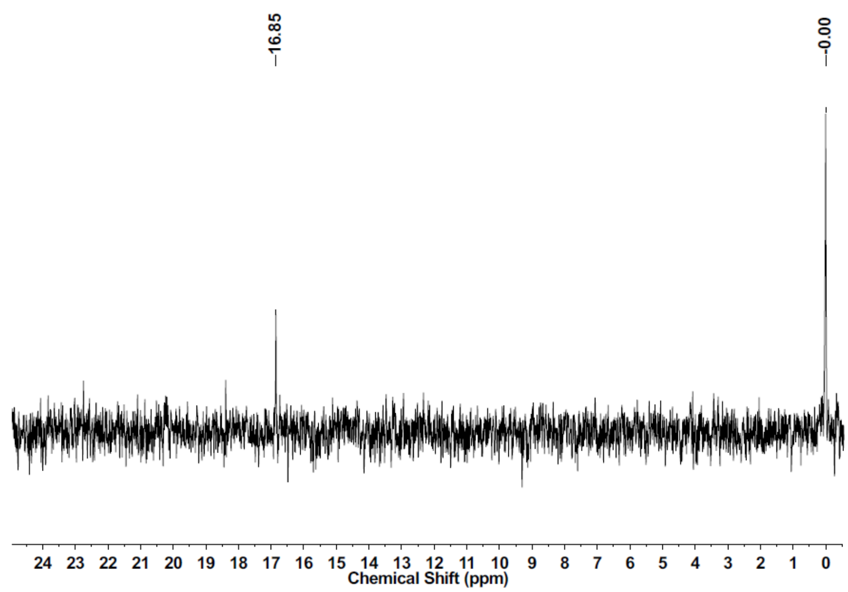


**Figure A 6.** $^{31}$P-NMR spectrum of PhnY reaction with (*S*)-**4**.

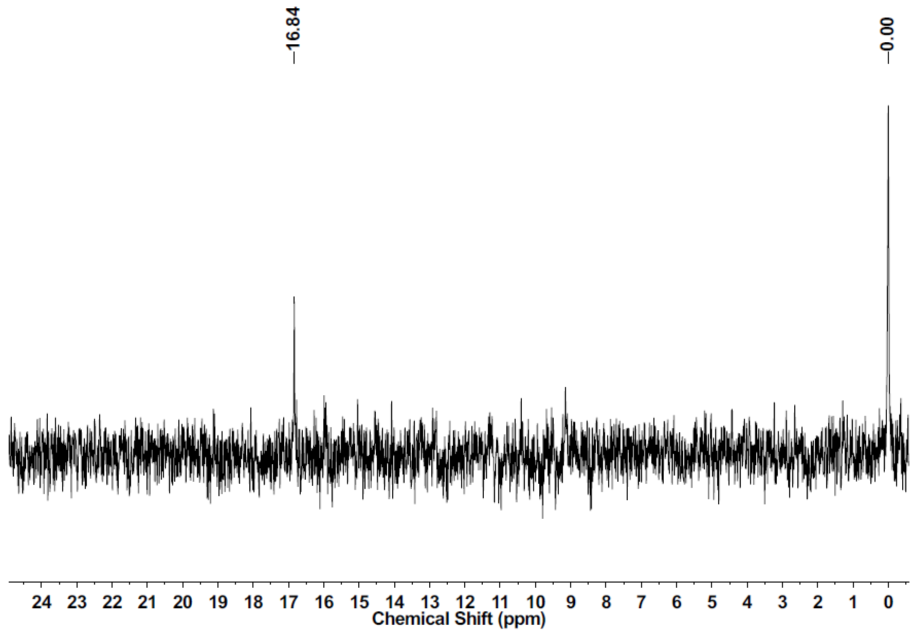


**Figure A 7.** $^{31}$P-NMR spectrum of enzyme-free control with (*R*)-**4**.

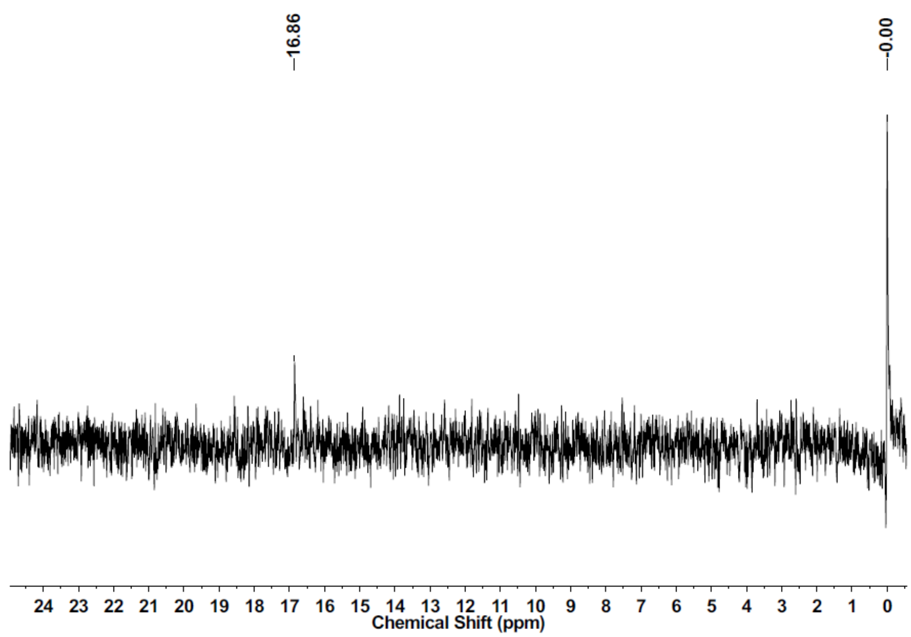


**Figure A 8.** $^{31}$P-NMR spectrum of PhnY reaction with (*R*)-**4**.

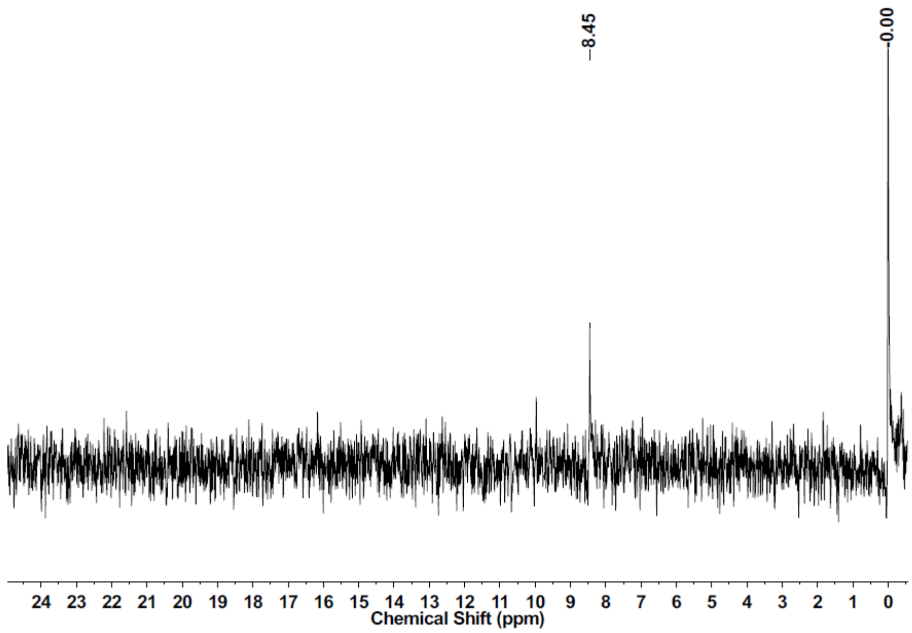


**Figure A 9.** $^{31}$P-NMR spectrum of enzyme-free control with **7**.

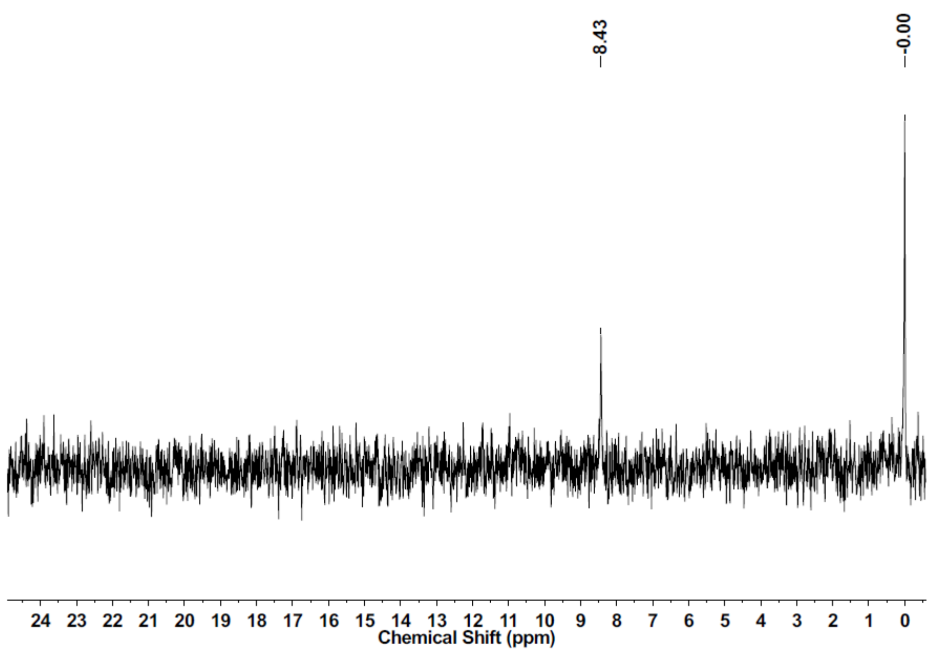


**Figure A 10.** $^{31}$P-NMR spectrum of PhnY reaction with **7**.

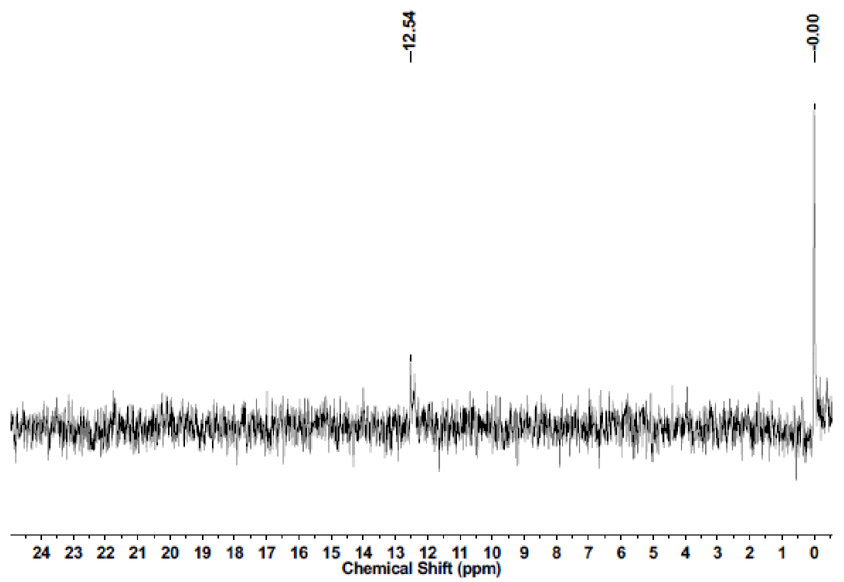


**Figure A 11.** $^{31}$P-NMR spectrum of enzyme-free control with **8**.

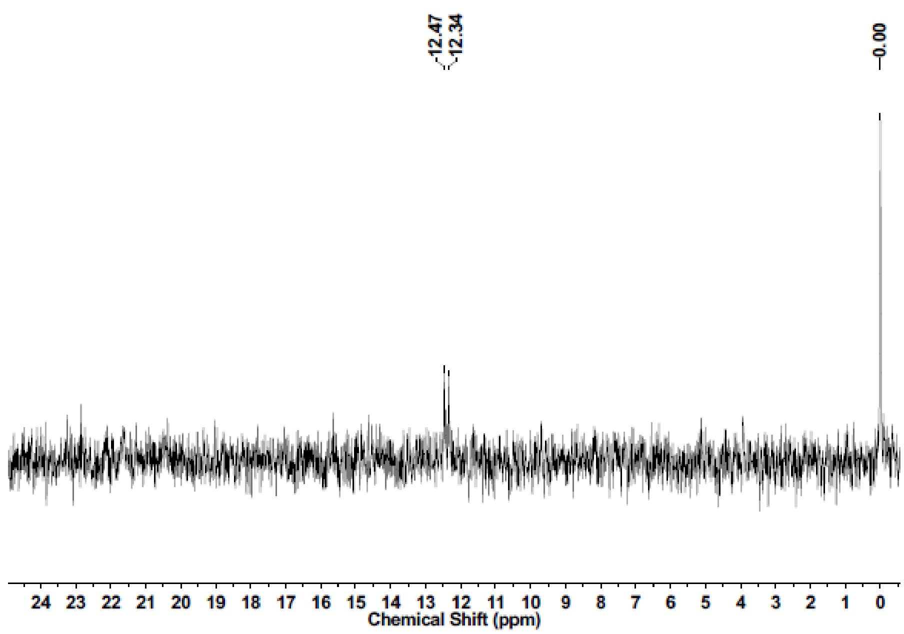


**Figure A 12.** $^{31}$P-NMR spectrum of PhnY reaction with **8**.

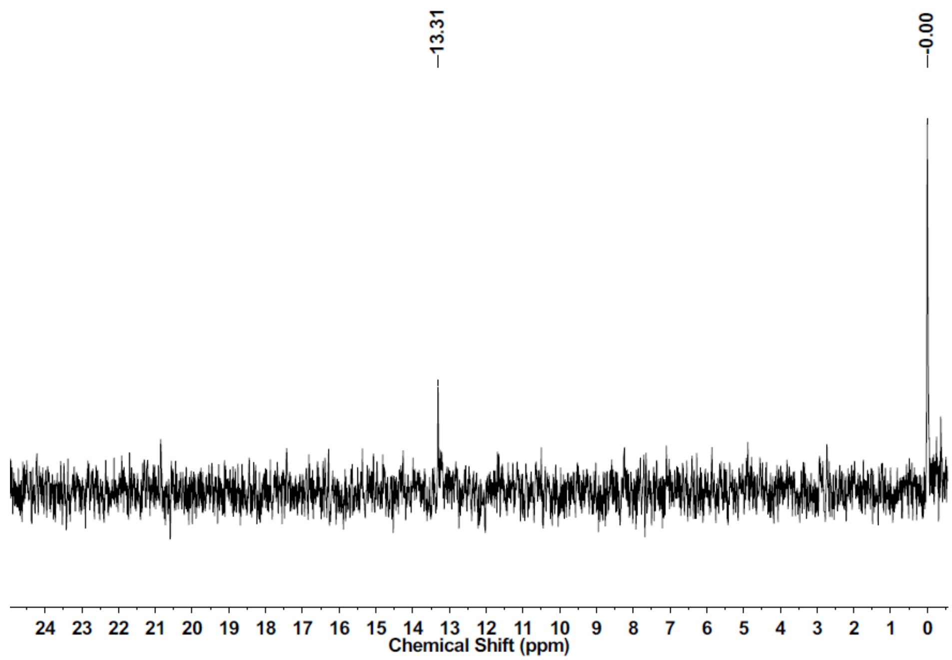


**Figure A 13.** $^{31}$P-NMR spectrum of enzyme-free control with **9**.

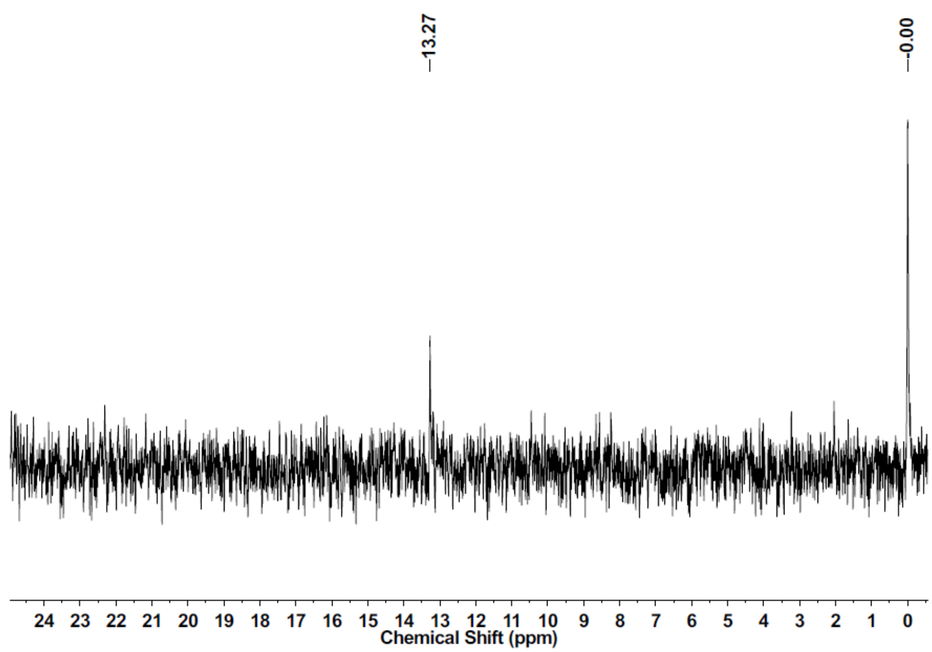


**Figure A 14.** $^{31}$P-NMR spectrum of PhnY reaction with **9**.

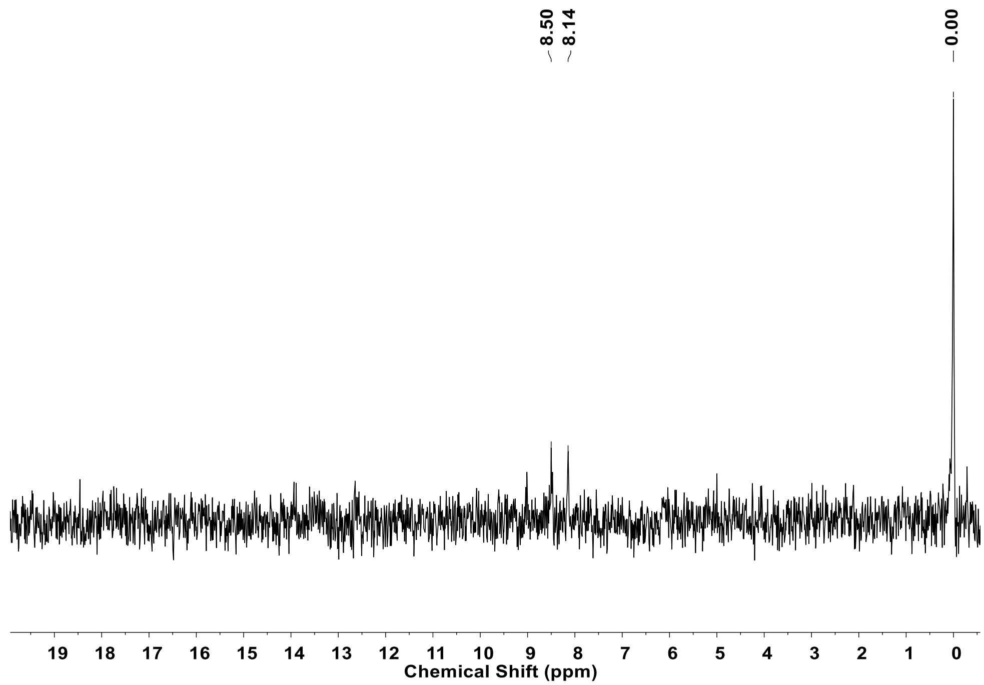


**Figure A 15.** $^{31}$P-NMR spectrum of enzyme-free control with **10**.

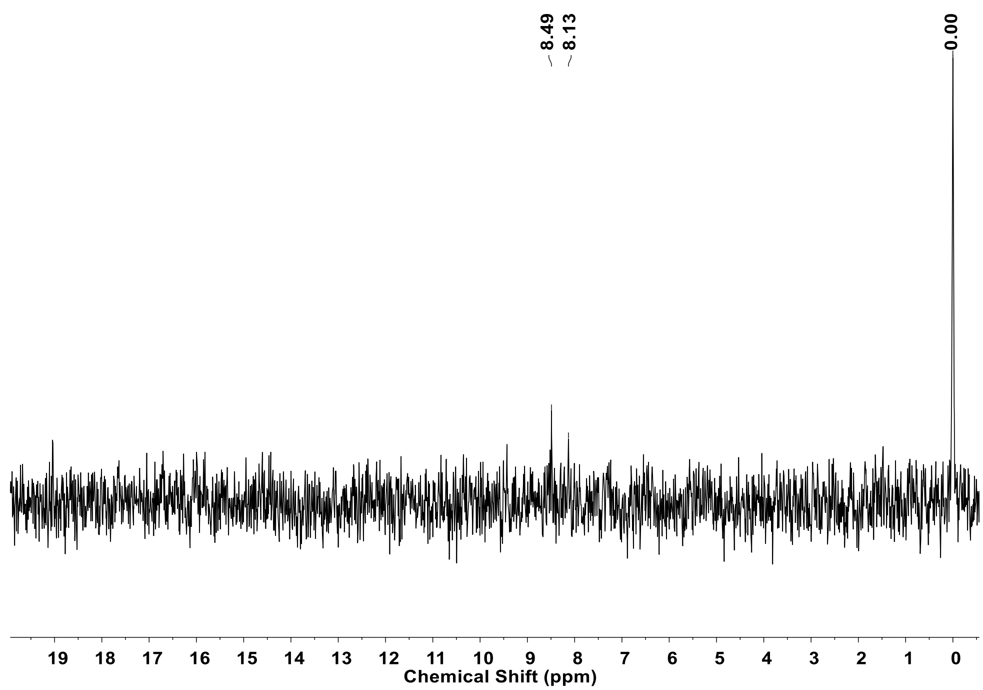


**Figure A 16.** $^{31}$P-NMR spectrum of PhnY reaction with **10**.

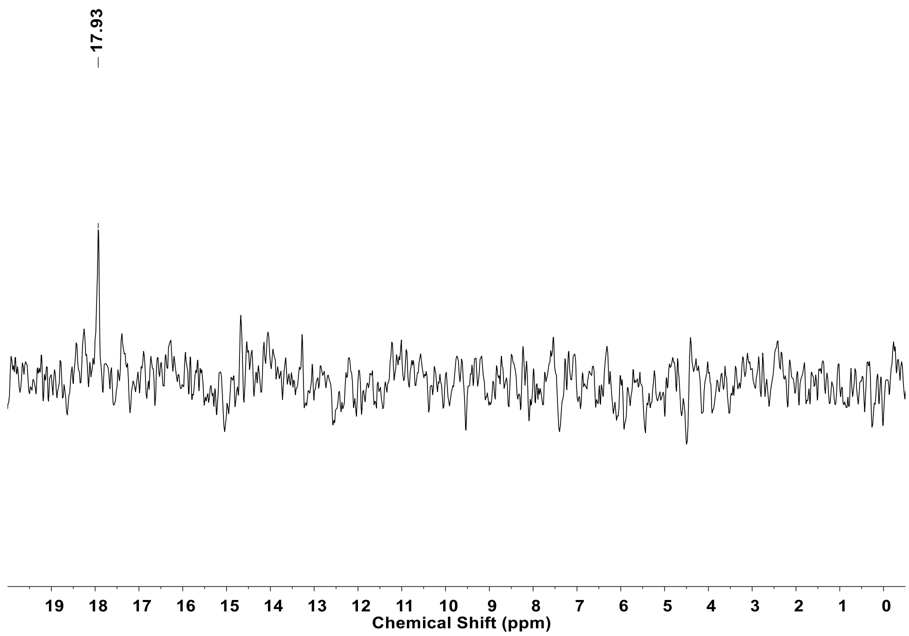


**Figure A 17.** $^{31}$P-NMR spectrum of enzyme-free control with **11**.

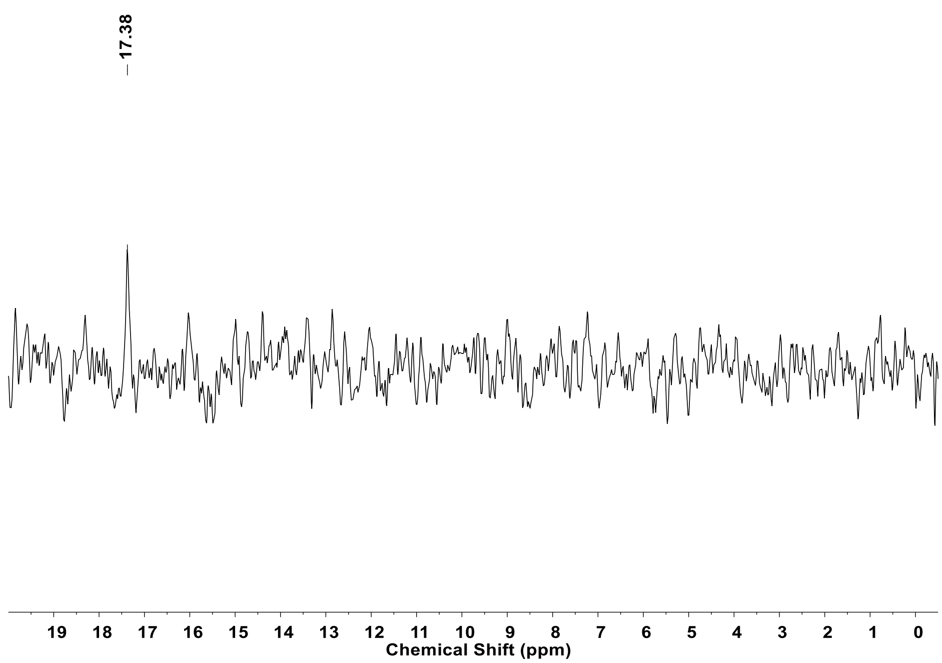


**Figure A 18.** $^{31}$P-NMR spectrum of PhnY reaction with **11**.

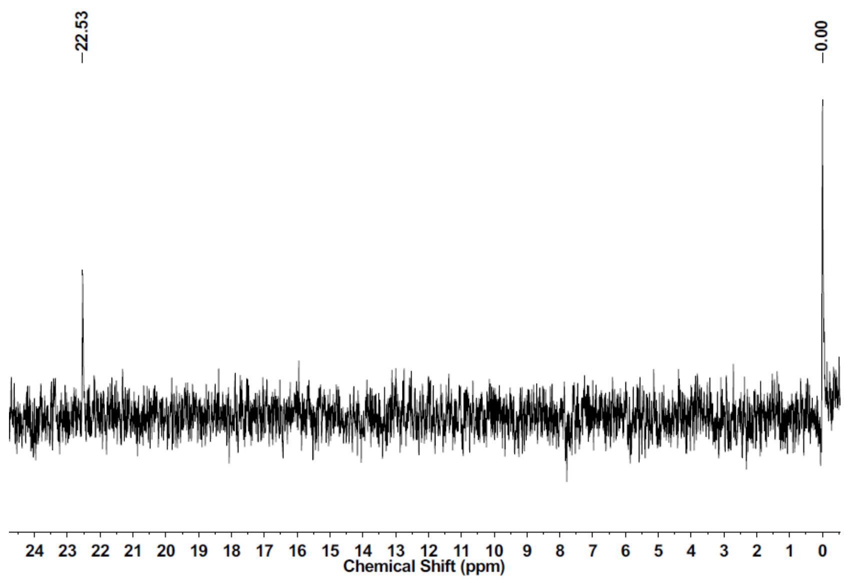


**Figure A 19.** $^{31}$P-NMR spectrum of enzyme-free control with **12**.

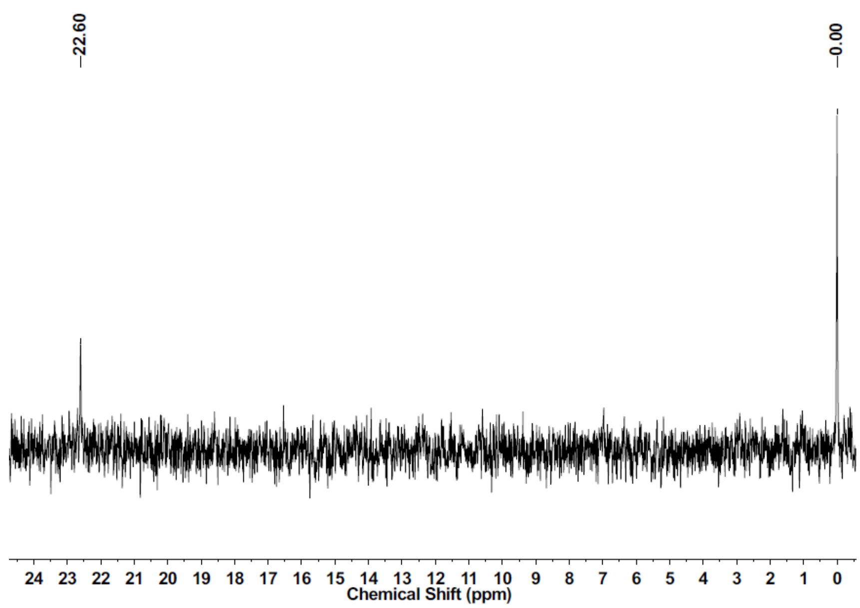


**Figure A 20.** $^{31}$P-NMR spectrum of PhnY reaction with **12**.

# Appendix B

## $^{31}$P-NMR spectra for PhnZ reactions

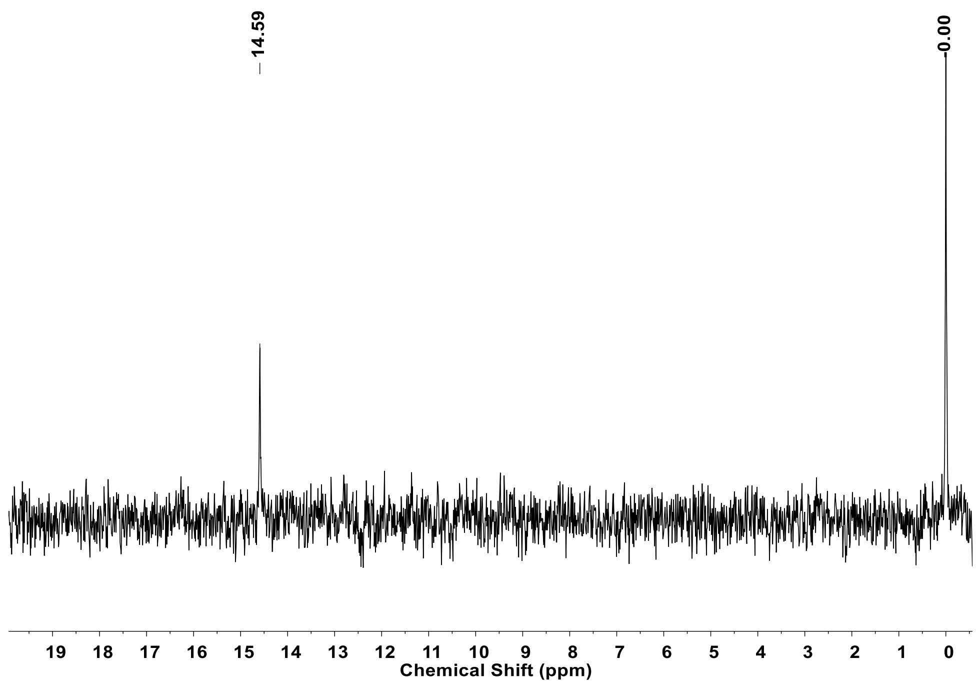


**Figure A 21.** $^{31}$P-NMR spectrum of enzyme-free control with (1*R*;2*R*)-**14**.

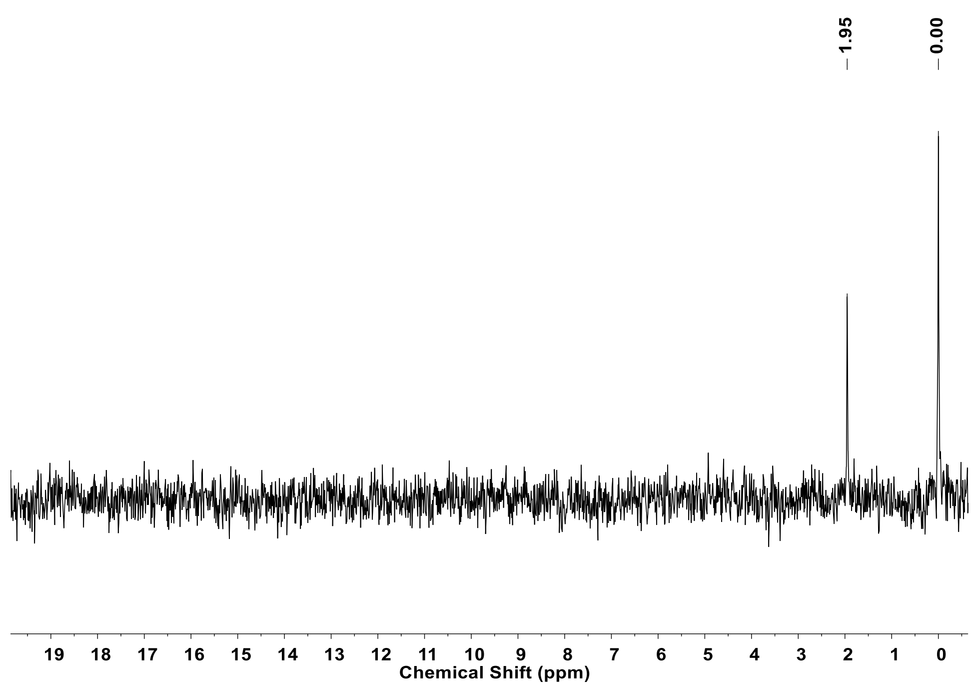


**Figure A 22.** $^{31}$P-NMR spectrum of PhnZ reaction with (1*R;*2*R*)-**14**.

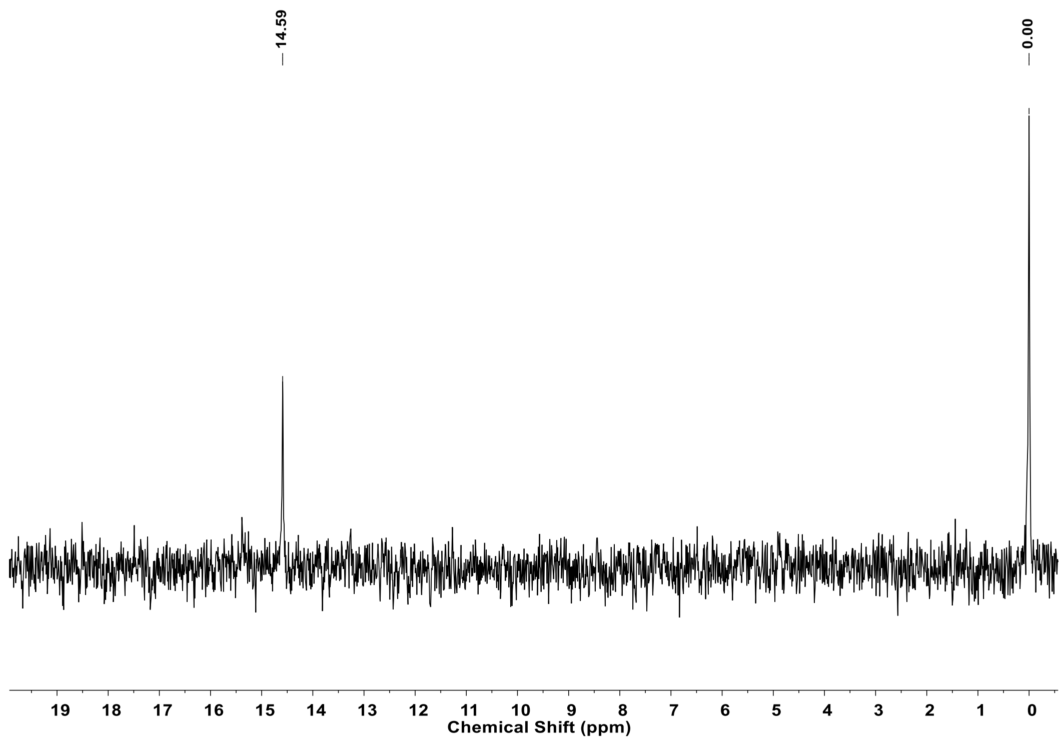


**Figure A 23.** $^{31}$P-NMR spectrum of enzyme-free control with (1*R*;2*R*):(1S,2S)-**14**.

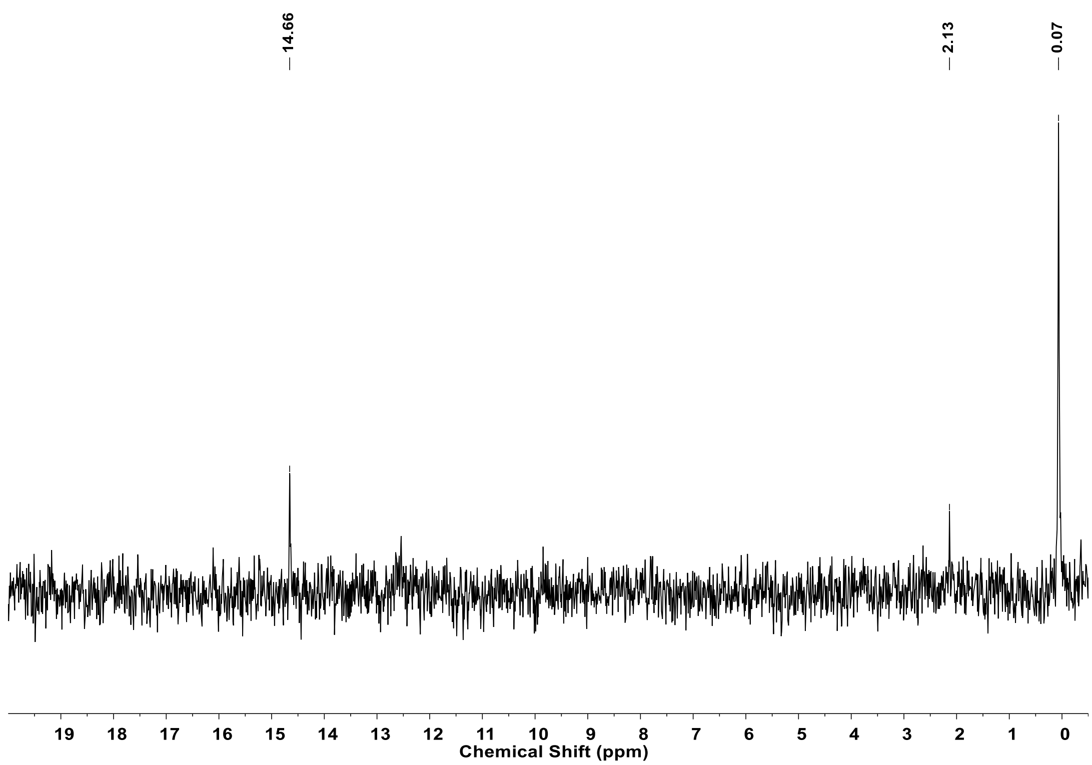


**Figure A 24.** $^{31}$P-NMR spectrum of enzyme-free control with (1*R*;2*R*):(1S,2S)-**14**.

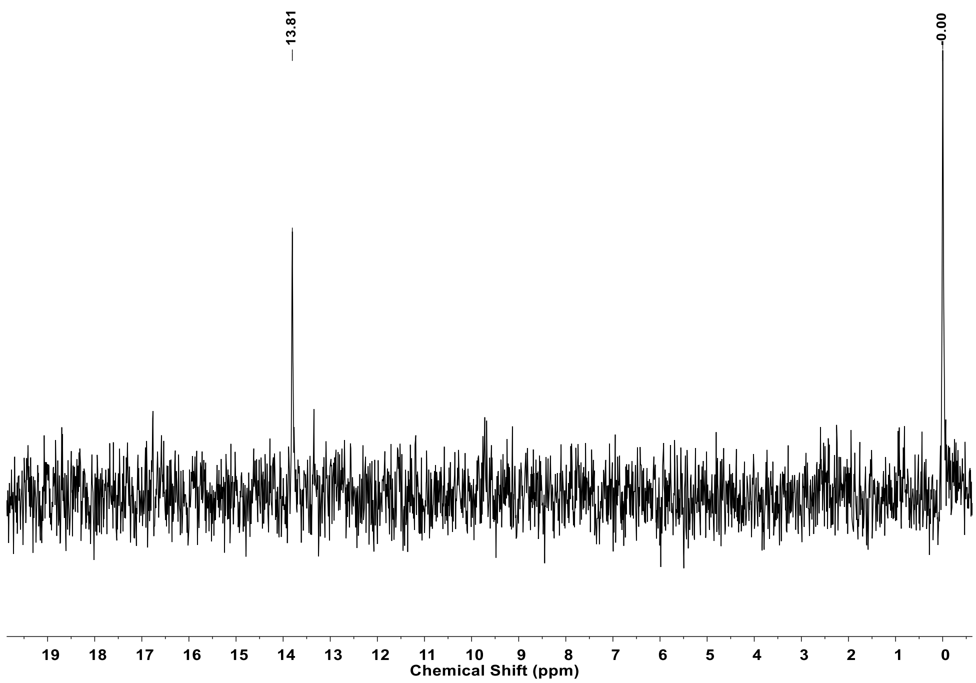


**Figure A 25.** $^{31}$P-NMR spectrum of enzyme-free control with (1R,2S):(1S,2R)-**14**.

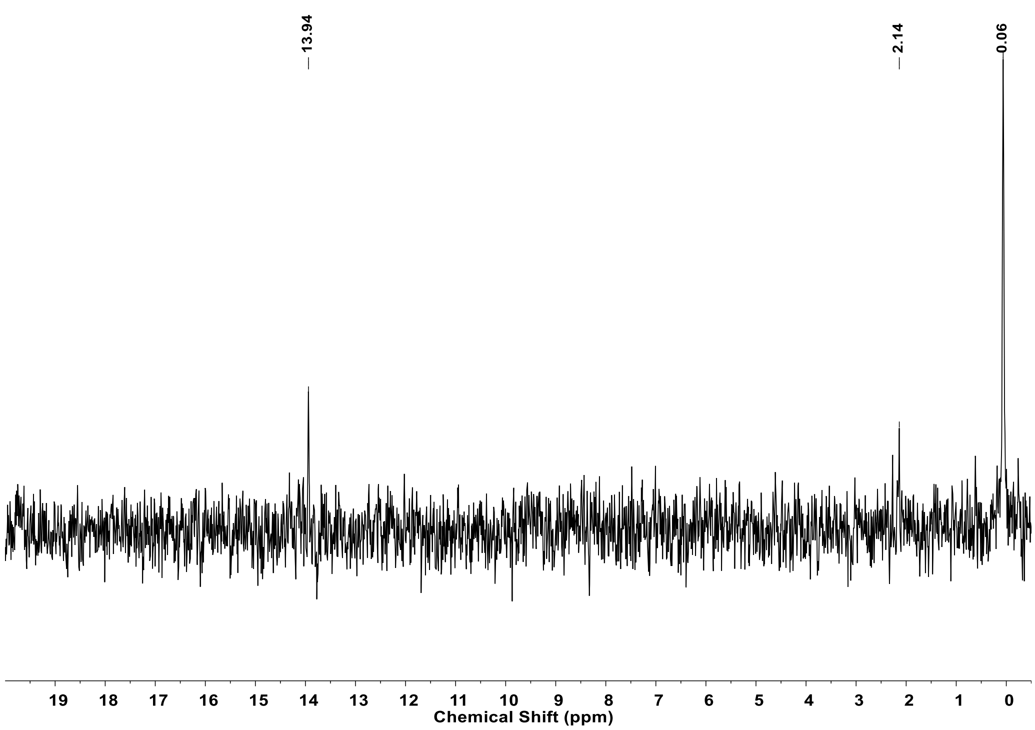


**Figure A 26.** $^{31}$P-NMR spectrum of PhnZ reaction with (1R,2S):(1S,2R)-**14**.

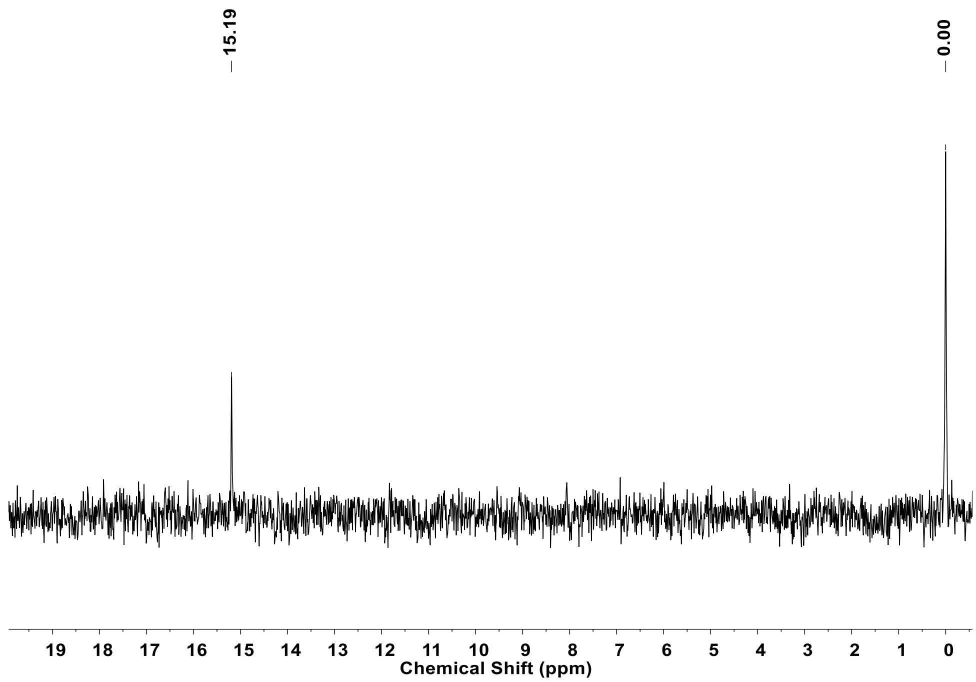


**Figure A 27.** $^{31}$P-NMR spectrum of enzyme-free control with (+/-)-**15**.

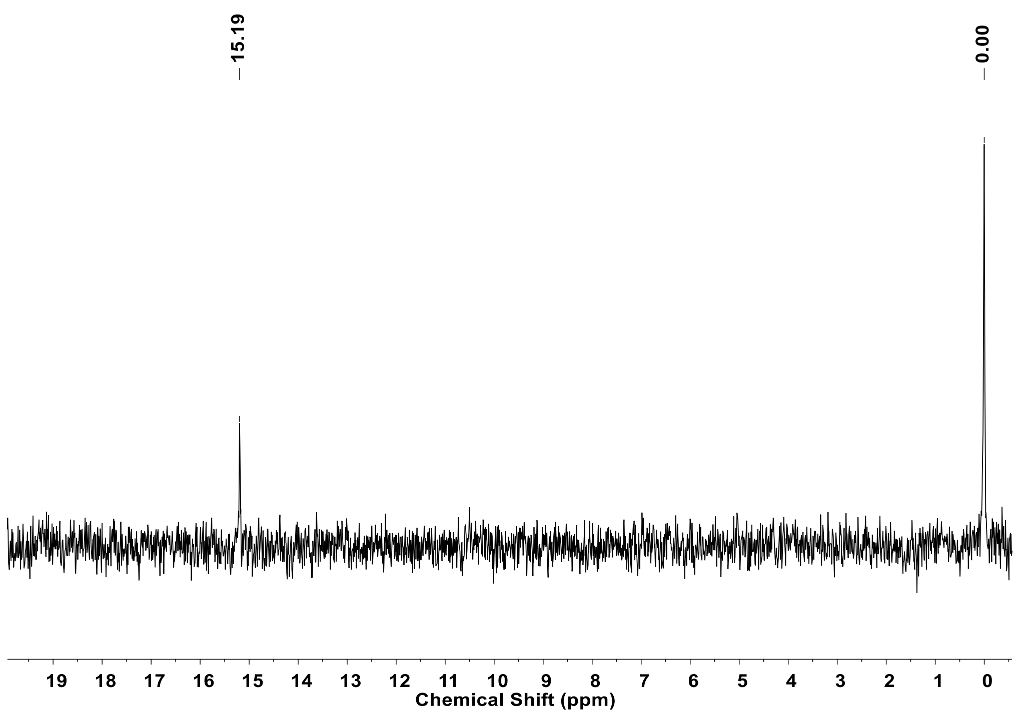


**Figure A 28.** $^{31}$P-NMR spectrum of PhnZ reaction with (+/-)-**15**.

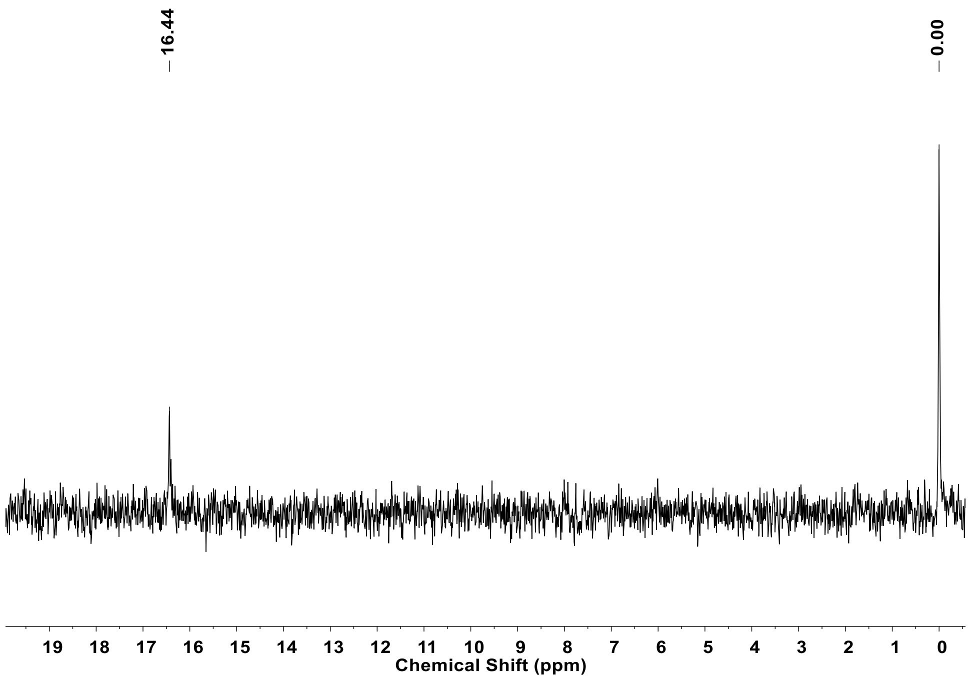


**Figure A 29.** $^{31}$P-NMR spectrum of enzyme-free control with (+/-)-**16**.

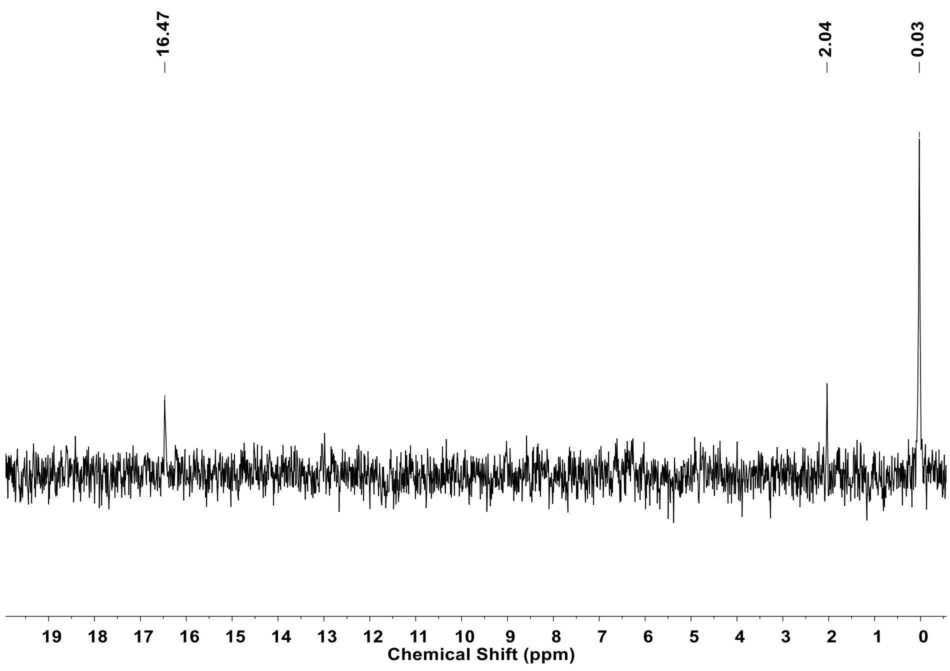


**Figure A 30.** $^{31}$P-NMR spectrum of PhnZ reaction with (+/-)-**16**.

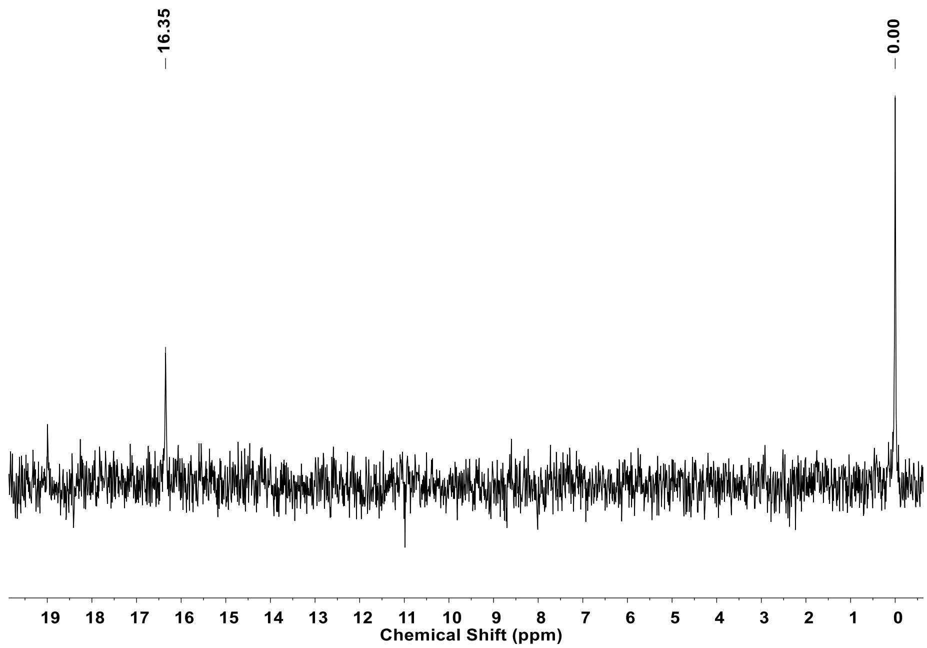


**Figure A 31.** $^{31}$P-NMR spectrum of enzyme-free control with (*S*)-**16**.

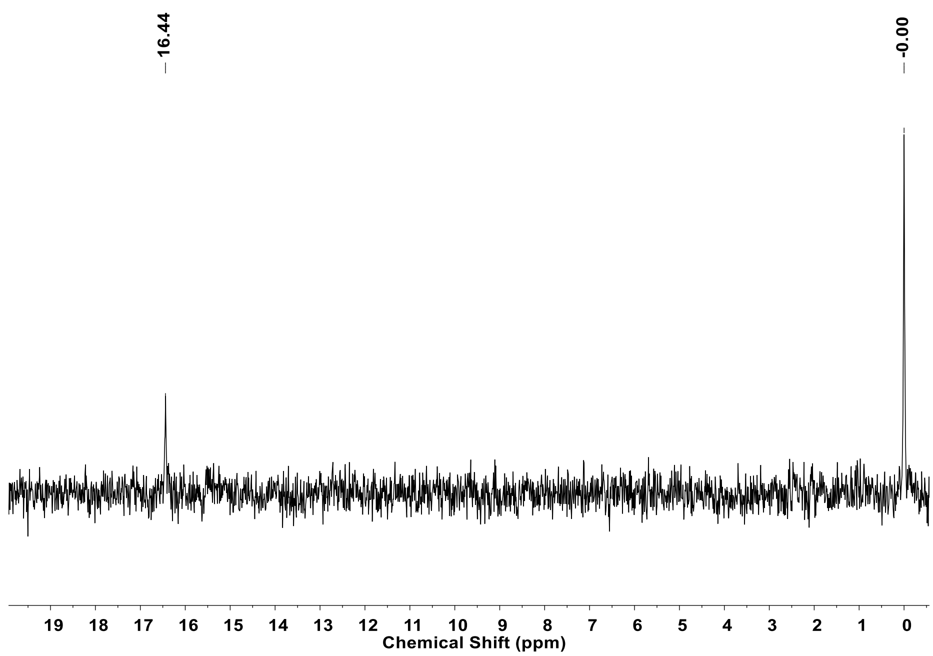


**Figure A 32.** $^{31}$P-NMR spectrum of PhnZ reaction with (*S*)-**16**.

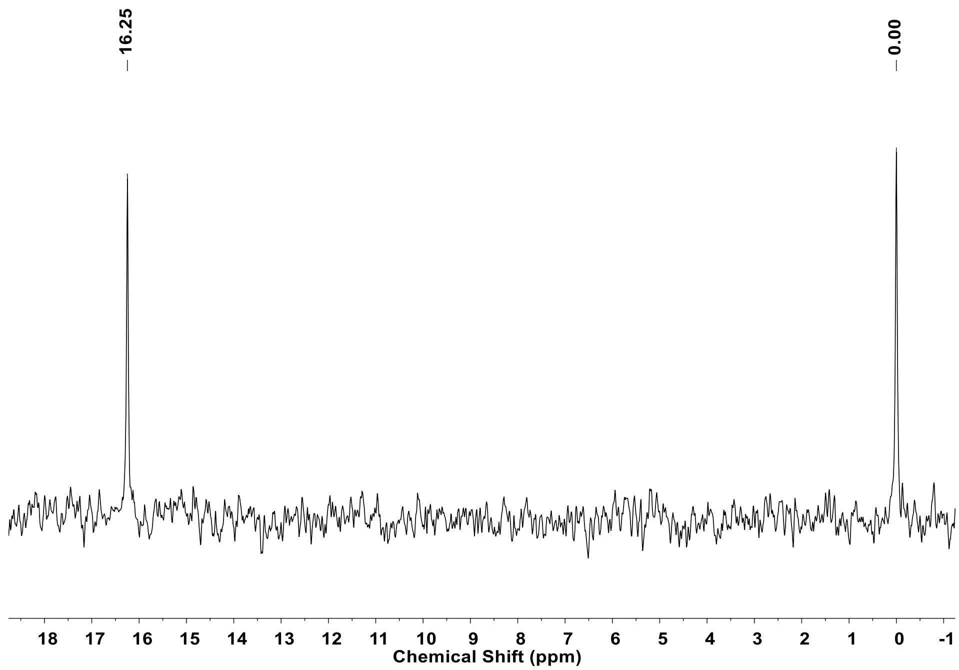


**Figure A 33.** [31]P-NMR spectrum of enzyme-free control with (*R*)-**16**.

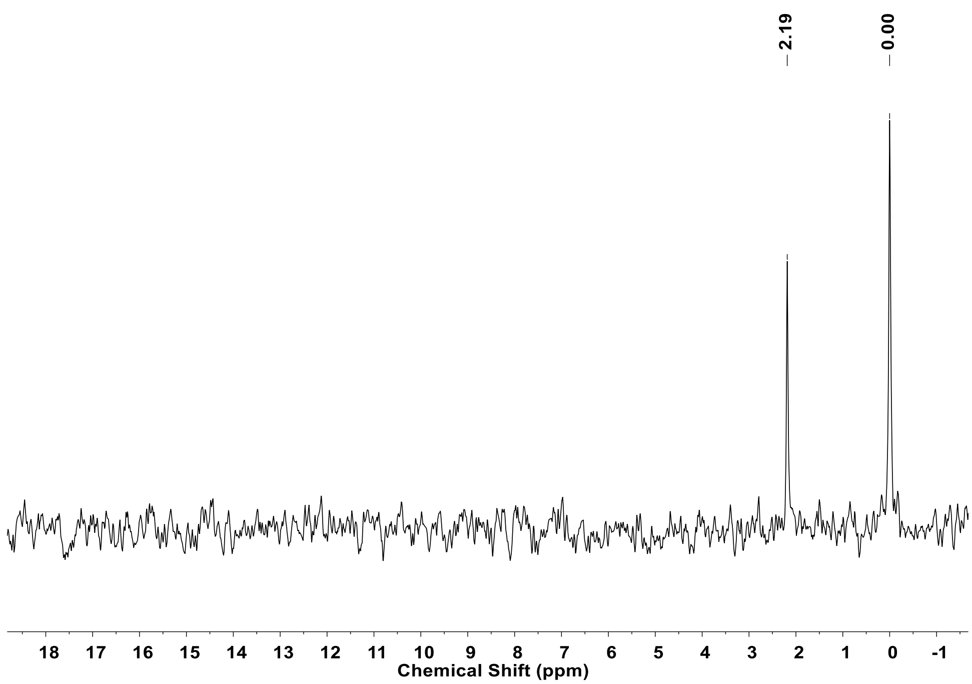


**Figure A 34.** [31]P-NMR spectrum of PhnZ reaction with (*R*)-**16**.

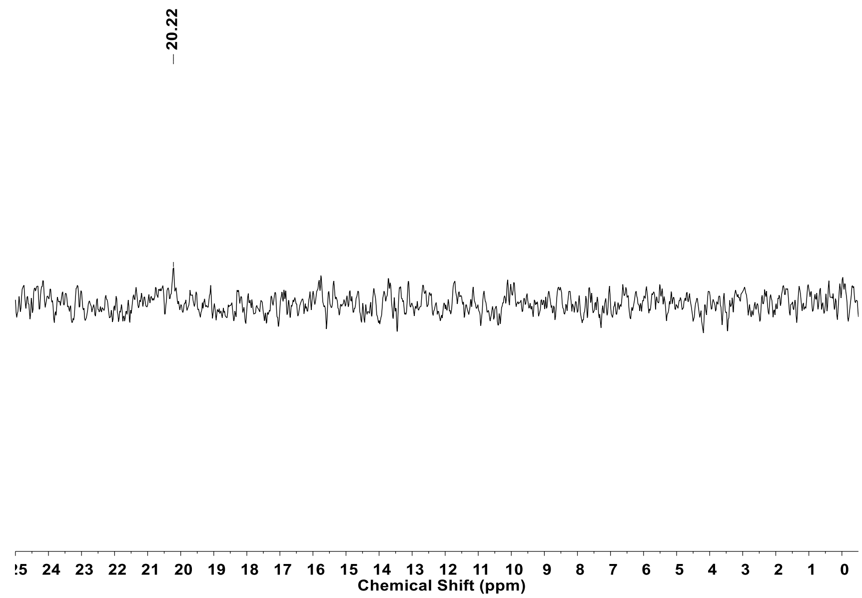


**Figure A 35.** $^{31}$P-NMR spectrum of enzyme-free control with (*R*)-**17**.

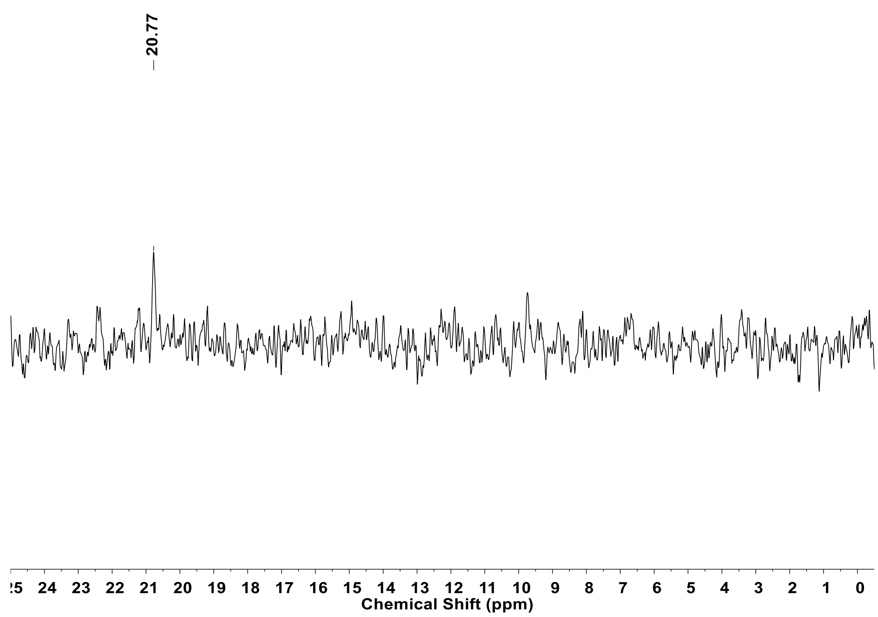


**Figure A 36.** $^{31}$P-NMR spectrum of PhnZ reaction with (*R*)-**17**

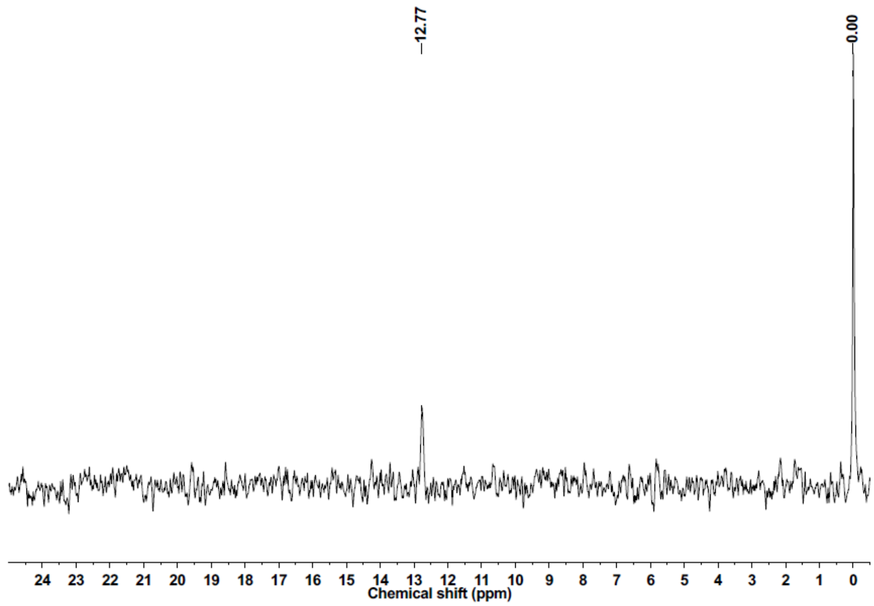


**Figure A 37.** $^{31}$P-NMR spectrum of enzyme-free control with (+/-)-**18**.

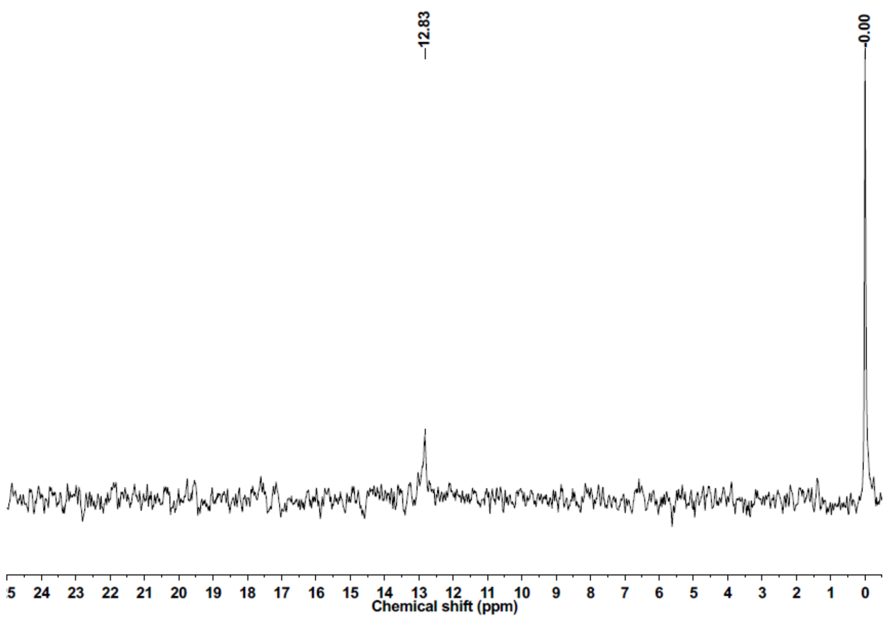


**Figure A 38.** $^{31}$P-NMR spectrum of PhnZ reaction with (+/-)-**18**.

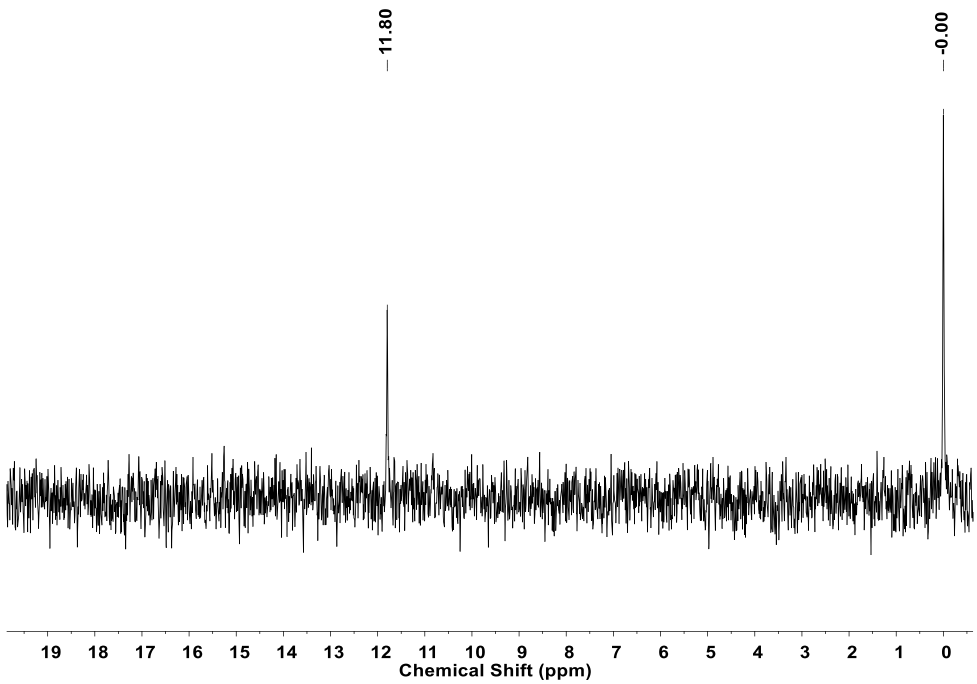


**Figure A 39.** $^{31}$P-NMR spectrum of enzyme-free control with **8**.

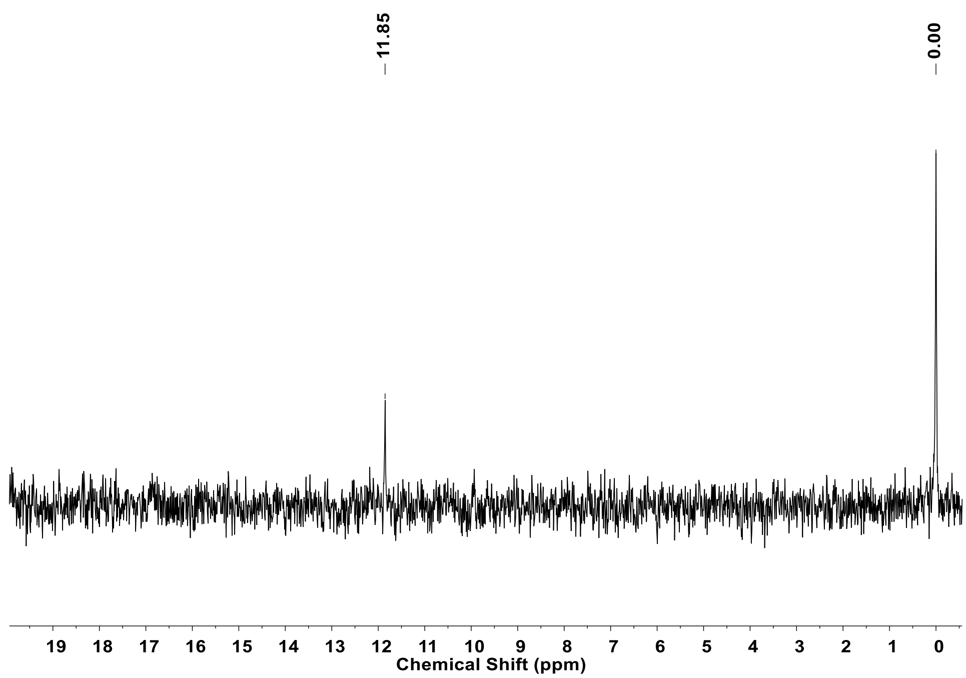


**Figure A 40.** $^{31}$P-NMR spectrum of PhnZ reaction with **8**.

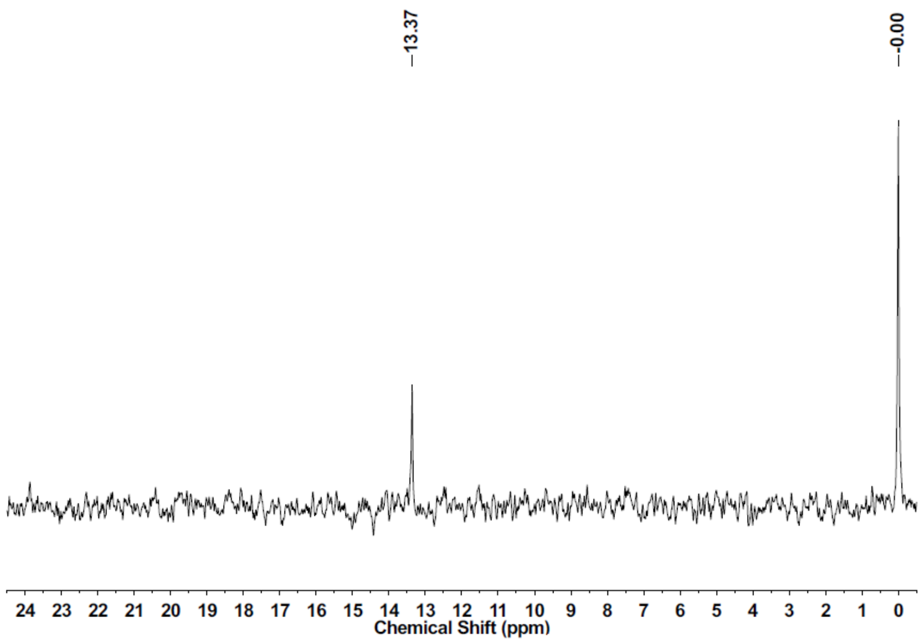


**Figure A 41.** $^{31}$P-NMR spectrum of enzyme-free control with (+/-)-**19**.

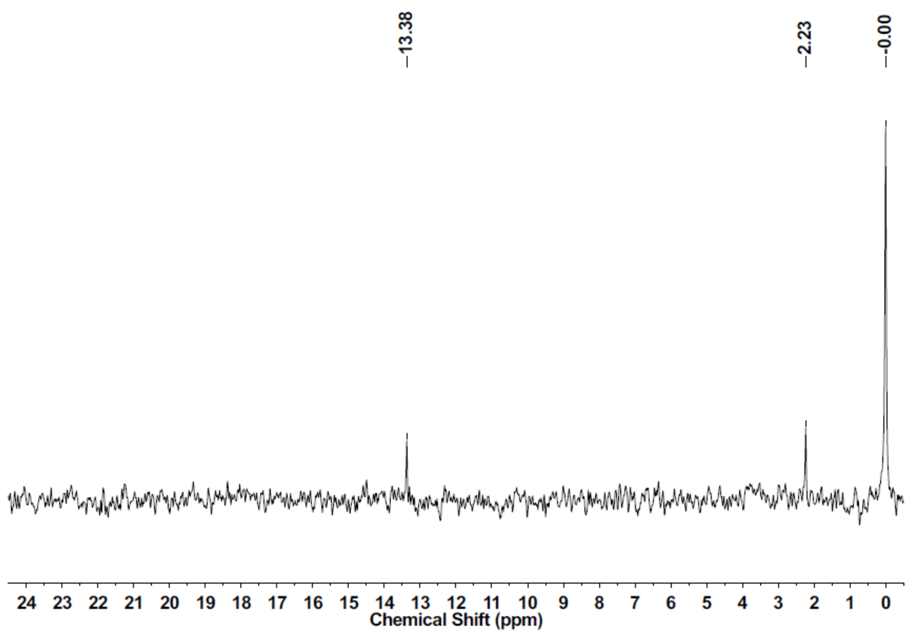


**Figure A 42.** $^{31}$P-NMR spectrum of PhnZ reaction with (+/-)-**19**.

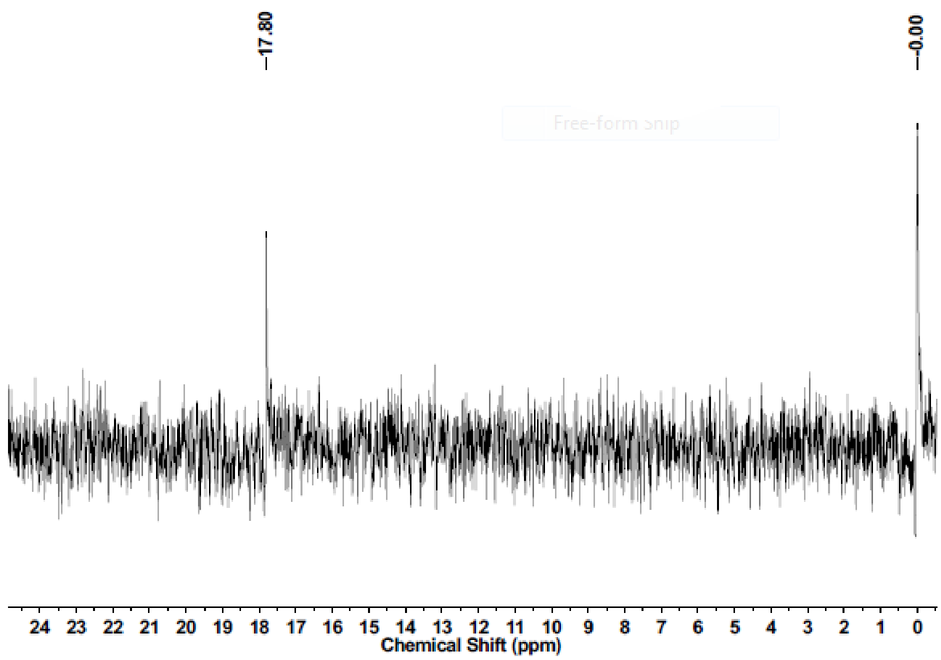


**Figure A 43.** $^{31}$P-NMR spectrum of enzyme-free control with (+/-)-**20**.

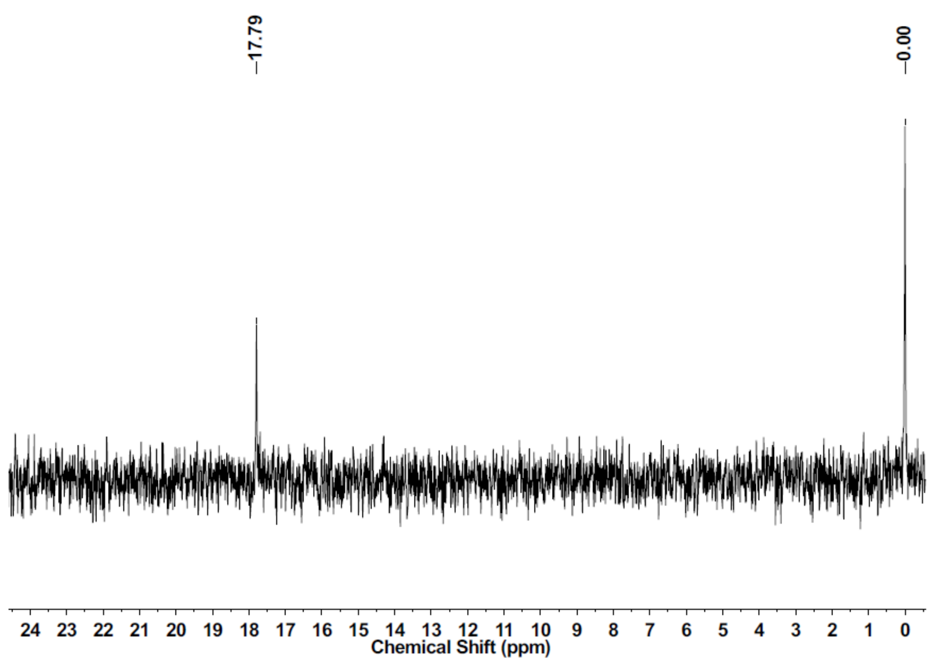


**Figure A 44.** $^{31}$P-NMR spectrum of PhnZ reaction with (+/-)-**20**.

# Appendix C

## $^{31}$P-NMR spectra for PhnZ Y24F/E27A

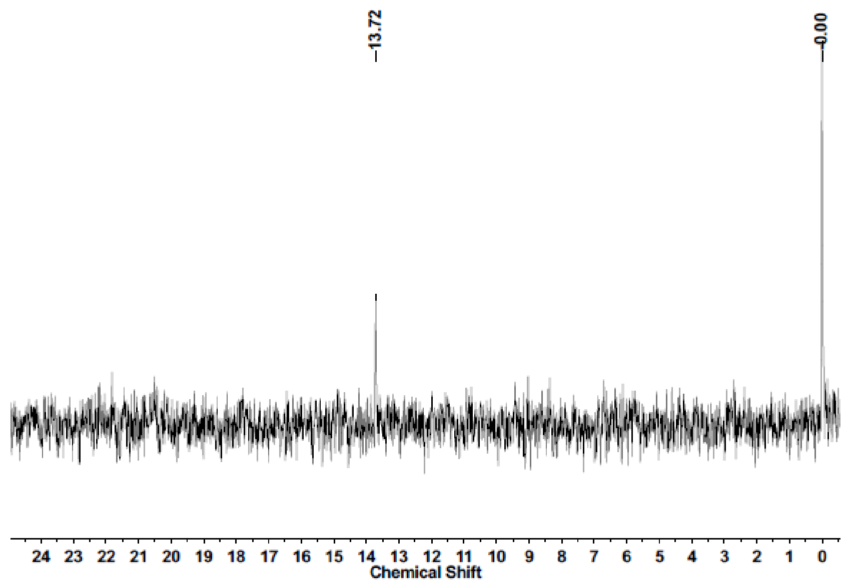


**Figure A 45.** $^{31}$P-NMR spectrum of PhnZ reaction with (*R*)-**13**.

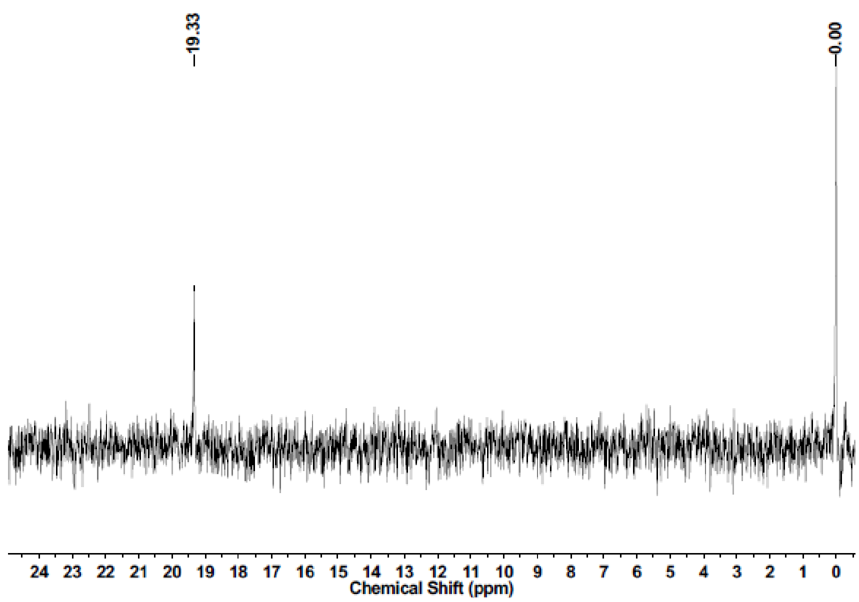


**Figure A 46.** $^{31}$P-NMR spectrum of enzyme-free control with (*R*)-**17**.

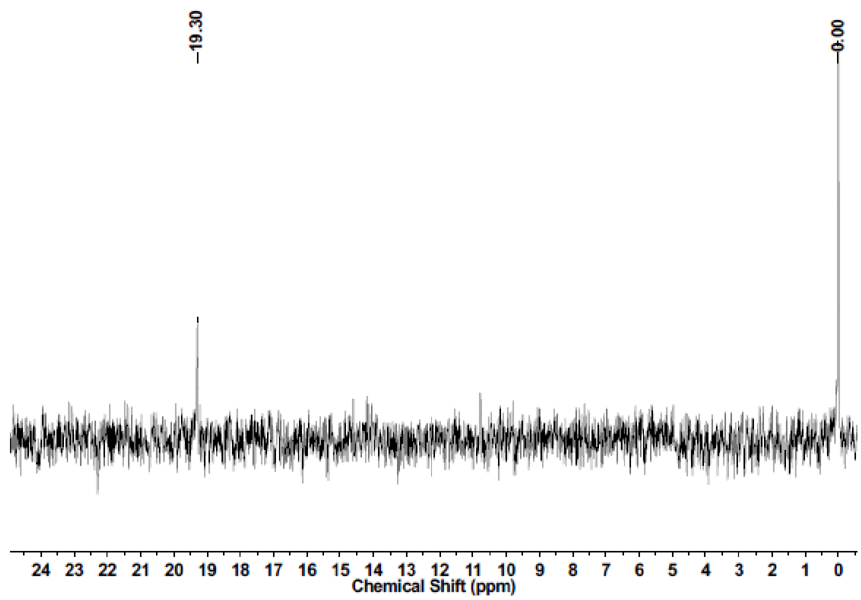


**Figure A 47.** $^{31}$P-NMR spectrum of PhnZ reaction with (*R*)-**17**.